Title
Colloidal Two-Dimensional Nanosheets as Functional Inks for Printable Electronic Thin-Films

Permalink
https://escholarship.org/uc/item/4485z8hm

Author
Song, Frank

Publication Date
2021

UNIVERSITY OF CALIFORNIA

Los Angeles

Colloidal Two-Dimensional Nanosheets as Functional Inks for Printable Electronic Thin-Films

A dissertation submitted in partial satisfaction of the

requirements for the degree Doctor of Philosophy

in Chemistry

by

Frank Song

2021

ABSTRACT OF THE DISSERTATION

Colloidal Two-Dimensional Nanosheets as Functional Inks for Printable Electronic Thin-Films

by

Frank Song

Doctor of Philosophy in Chemistry

University of California, Los Angeles, 2021

Professor Xiangfeng Duan, Chair

Thin-films deposited through scalable printing techniques is key to next generation large-area electronics, such as displays, sensors, and soft electronics. The typical thin film deposition approaches such as chemical vapor deposition and high vacuum physical vapor deposition are energy intensive, or require high temperatures that limit the diversity of substrates, and are generally too costly for the next generations of cheap wearable electronics. Solution-processable thin-films can be prepared at ambient pressures and temperatures allowing electronics to be made on soft plastic substrates for flexible devices. To this end, solution processable inorganic nanomaterials have superior stability and electronic performance when compared to currently researched organic semiconducting materials. In particular, two-dimensional nanosheets represent an attractive candidate for solution-processed thin-film electronics. Their ultrathin wide-area structure offers the perfect geometry to form electronic thin-films with complete coverage, and the natural flexibility of such 2D nanosheets suits well for the needs of soft electronics. To enable robust application of colloidal nanosheets for solution-processed electronics, an essential task is to develop functional 2D inks with controllable thickness, size and electronic properties. Additionally, new printing and processing techniques need to be investigated to produce uniform films. This thesis will look at both bottom-up synthesis and top-down intercalation exfoliation methods of producing colloidal nanosheets which can then be further processed into inks. For synthetic methods, we investigate the preparation of InSe and SnSe nanoplates using long chain amines as a surfactant. For top-down strategy, we focus on using electrochemistry to intercalate and then further exfoliating with gentle bath sonication. Initially MoS_2 is investigated by cathodically intercalating large organic quaternary ammonium ions using a simply electrochemical cell setup. This produces MoS_2 that remains in its 2H state with electron mobilities of 10 $cm^2 \cdot V^{-1} \cdot s^{-1}$. The produced nanosheets of MoS_2 shows promising semiconducting thin-film applications with superior electronic performance. Finally, by utilizing home-grown layered crystals, we show a large family colloidal nanosheets (InSe, In_2Se_3, Bi_2Se_3, Bi_2Te_3, $SnSe_2$, SnS_2, etc) may be prepared using a similar intercalation and exfoliation approach.

The dissertation of Frank Song is approved.

Justin Caram

William M. Gelbart

Yang Yang

Xiangfeng Duan, Committee Chair

University of California, Los Angeles

2021

Dedicated to my parents,

my sister Janet, and all my close friends

for their continuous support, wisdom, and sanguinity.

Smooth seas do not make skillful sailors.

Table of contents

List of Figures

Acknowledgments

It has been a privilege to be given this opportunity to pursue my graduate studies in the Department of Chemistry and Biochemistry at University of California, Los Angeles. The past five years were truly impactful for my growth as a researcher, problem solver and adult. The years spent during my PhD track offered some of the most difficult and persevering challenges I have ever experienced. These endured hardships have developed me into someone who can proudly call themselves an official scientist. I would like to take this section in my thesis to thank those who have assisted me throughout and made my journey one to be cherished.

First and foremost, I would like to thank my advisor, Professor Xiangfeng Duan. His unwavering support, leadership, and mentoring guided me to become the scientist I am today. He offered the perfect balance of hands-on approach while also allowing me to freely explore my field on my own. He would always encourage me to think outside of the box when solving a problem and to not limit myself in any capacity when it comes to research. These are lessons I find valuable in all facets of my life. I started off my first year being completely lost and frustrated to the point of nearly dropping out of the doctoral program. I was always able to come to Professor Duan with any troubles I had and we were able to discuss and figure out a solution. I have now proudly developed into someone who can design and lead projects on my own.

During my PhD experience there have been many graduate students who have assisted me. I want to thank Zhaoyang Lin who mentored me during my studies. He passed down his years of experience and I truly could not have gotten through this without his help. Introducing me to many new concepts, instruments, and how to solve a problem with scientific rigor. He is truly a pioneer in the field of two-dimensional semiconductors and I am lucky to be able to work with him. We had many late-night discussions on how to push research to the limit. He challenged me to think outside the box and changed my perspective on how research is done. Additionally, I would like to thank some of the other graduate students and post-docs. Specifically, I would like to thank Dan Zhu and Daniel Baumann for making time to discuss research. Many of my ideas came from our white board sessions as well as many of the solutions to my research challenges. It was always helpful to get a separate set of eyes to look at my work. Finally, I would like to thank all of the people from my research group as well as helpful students from other groups for making my PhD journey an enjoyable one.

VITA

2011	High School Diploma San Dieguito Academy Encinitas, CA
2016	Bachelors in Chemistry University of California, Santa Cruz Santa Cruz, CA
2018	Masters of Science in Chemistry University of California, Los Angeles Los Angeles, CA
Expected in **2021**	Doctor of Philosophy in Chemistry University of California, Los Angeles Los Angeles, CA

Chapter 1. Introduction

1.1 Background and motivation of Large-area electronics

Large-area electronics, synonymous with printed electronics is a new method of producing electronic thin-film devices through printing procedures. Here functional materials (conducting, semiconducting, and insulating) are dispersed in a suitable solvent and deposited through a solution-based method. The goal is to address a range of applications beyond the traditional monocrystalline silicon currently used in today's computer chips.[1] It does not suffer the same limitations as traditional silicon-based electronics fabrication. The material is deposited through low-temperature solution process, allowing a large variety of substrates to be used such as plastics and textile. Initially, large-area electronics focused on area-intensive applications such as displays and photovoltaics. Over the last decade, the scope of applications has expanded to flexible devices, medical, electrodes, and sensing (Fig. 1) .[2-8]

Figure 1.1. Showing the diverse number of applications for printed electronics. These range from thin-film transistors, sensors, LED lighting, flexible displays, large-area solar cells, energy storage devices, and transparent electrodes. *Adapted from reference 9.*

Using printing methods for electronics assembly allows for the application of large device dimensions that traditional single crystal silicon cannot do efficiently. By utilizing ambient conditions (temperature and pressure), solution-based approaches can process electronically active thin-films much more economically with greater scalability. Being able to operate at room temperature substrates such as plastic and rubber can be used to make flexible and stretchable electronics.[10] This technology is suitable for wearable medical sensors where flexibility is required to conform to biological systems and cost effectiveness is allows disposability for hygiene concerns. It has been demonstrated using ink-jet printed silver nanoparticles on polydimethylsiloxane (PDMS) can create a simple resistive sensor for measuring heartbeat pulse (Fig. 2).[11] Printing methods can range from simple spin-coating to more advanced ink-jet where entire lithography steps can be avoided to pattern the material (Fig. 3).[12] Using roll-to-roll printing, large quantities of electronic thin-films can be fabricated through a scalable process which would reduce the cost significantly. This process could largely be automated to produce large quantity batches of electronic devices.

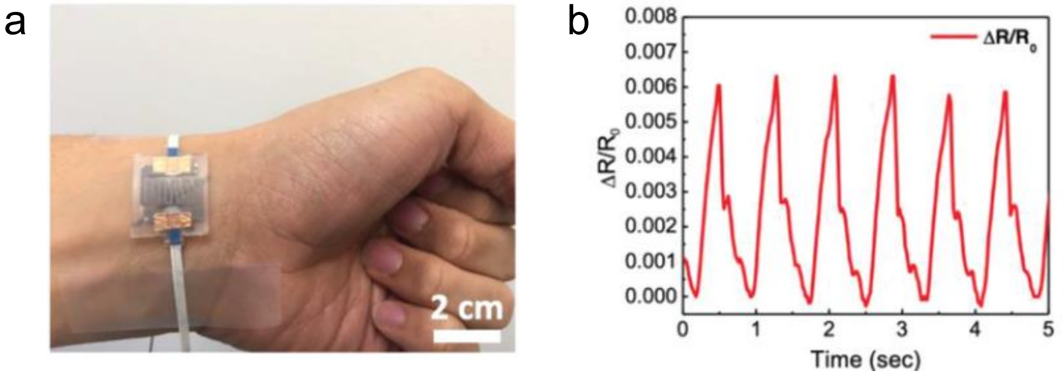

Figure 1.2. Ink-jet printed patterned silver nanoparticle device on PDMS. (a) Printed silver nanoparticle pressure sensor placed above artery in wrist to measure pulse. (b) Relative resistance of device as a function of time. The pulse places pressure on the device which changes the resistance. *Adapted from reference 11*.

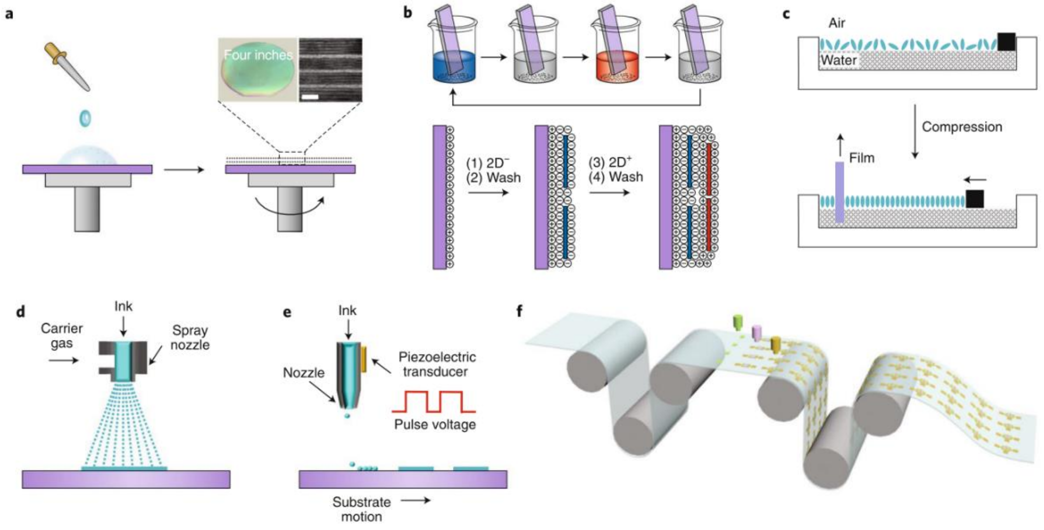

Figure 1.3. Thin-film assembly using various printing techniques. (a) Spin-coating, left inset image is a four-inch wafer with a thin-film of solution processed molybdenum disulfide (MoS_2). Right side inset is a transmission electron microscope image of Bi_2Se_3 film. (b) Layer-by-layer deposition of film. This printing technique operates on electrostatics where different layers of charged material are deposited onto the film followed by a washing step to eliminate excess ions. (c) Langmuir Blodgett trough consists of a monolayer of material on the surface of a solvent. A barrier is used to compress the material onto a dipped substrate forming a film. (d) Spray-coating of film. (e) Ink jet printing allows patterning without the need of lithography. (f) Roll-to-roll continuous processing of devices on flexible substrate. *Adapted from reference 12*.

1.2 Limitations of previously studied electronic materials

There is in general an inverse scaling relationship between device substrate size (area) and its electronic performance (charge carrier mobility). Traditional monocrystalline silicon and gallium arsenide offer high electronic performance but cannot be scaled to large-area attributed to limitations of crystal growth. Traditional semiconductors are grown using the Czochralski method where a single crystal seed is used to pull a large crystal from a melt.[14] This requires a special furnace (Fig. 4) under argon environment to prevent excessive oxidation and heating coils to reach <1400°C. Starting from 1950, the crystal diameter of single crystal silicon ingot has been pushed from 50 mm to 450 mm over the years, but this increase in size is still not adequate to cover electronics required for true large-area. An early attempt at silicon based large-area electronics was the use of polycrystalline silicon. This involves the use of many small crystals known as crystallites of high-purity silicon to form a continuous film. Polycrystalline silicon synthesis involves silane (SiH_4) heated using a furnace with a carrier gas where it then undergoes a process of chemical vapor deposition on the substrate of choice. The chemistry behind the of making polycrystalline silicon is as described by the following reaction:[15]

$$SiH_4(g) \rightarrow Si(s) + 2\,H_2(g)$$

This chemical decomposition of silane could allow the large-area electronic functionalities with adequate performances. This pyrolysis-based deposition operates in temperatures of 500-800 °C which restricts the substrates to thermally tolerant ones such as glass.

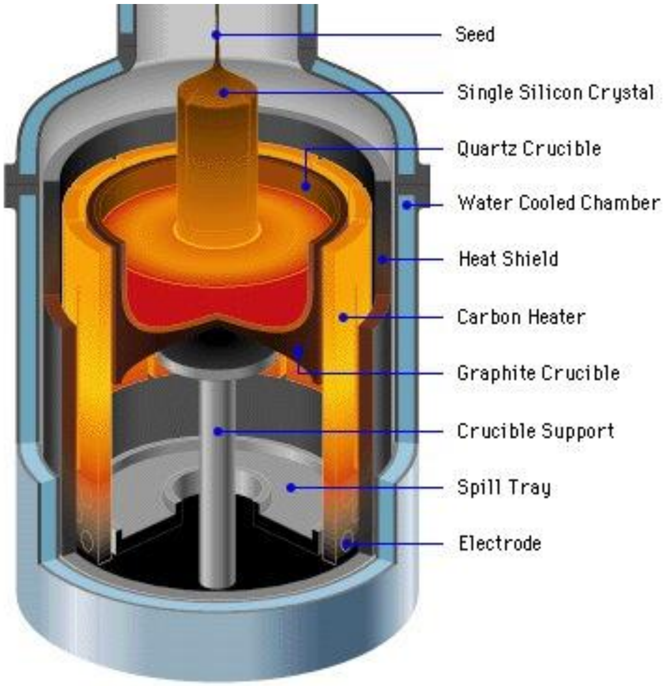

Figure 1.4. Diagram of a Czochralski furnace for electronic grade silicon ingot growth. A hybrid quartz/graphite crucible containing highly pure silicon is heated to 1400 °C until a homogenous melt is formed. A monocrystalline silicon seed is dipped into the melt and pulled while simultaneously being rotated. As it pulls from the melt, the colder water-cooled chamber environment allows for crystallization. Image adapted from *meroli.web.cern.ch*.

Asides from semiconductors, there is also a growing demand for large-area transparent conductors to be processed through solution deposition. This technology would allow touch-based displays to increase in size and to be made at much lower cost for consumer electronic goods. Thin transparent conductor films as the electrodes for solar cells allows additional photons to interact with the photovoltaic materials compared to traditional metal grid contacts. Currently the most studied transparent conductor is indium tin oxide (ITO). This alloy is a mixture of indium oxide doped with tin atoms to make it conductive, the general ratio is 74% indium, 18% oxygen, and 8% tin by weight. ITO is commercially used for touch screens; liquid crystal displays and solar cells. It is favorable for solar cells applications due to its high conductivity and transparency with low absorption in the visible range. The typical process of ITO film making is through a physical vapor deposition, either using electron beam evaporation or magnetron sputtering.[16] These processes all require vacuum chambers which becomes progressively expensive and energy intensive as the scale increases. Finding a way to cheaply print transparent conductive films would allow new applications such as electrochromic glass and self-defrosting windows that utilizes electrical current.

1.3 Requirements for solution-processed large-area electronics

Proper next generation large-area electronics requires flexibility and low cost per area for applications in displays, electronic paper, and health monitoring. This requires material integration on pliable plastic substrates with sufficient computational performance and communication functionalities. A key requirement is to have the active material colloidally suspended in a solvent with no aggregation as an ink. The solvent of choice must be the correct viscosity, surface wettability and ability to rapidly evaporate leaving behind an even film with no coffee ring effect. Ideally this solution can be concentrated down into an ink with long term stability so that it may utilize modern printing technology to deposit films through a low-temperature and minimal pressure process.[17] Finally the solution-processed devices need to be fabricated from temperatures below the glass transition of plastics (>300-400°C).

Some of the earliest work of developing functional electronic inks used organic polymers. Organic semiconductors for thin-films have two basic requirements to be successfully integrate into printed electronic applications. First is an extended π-conjugated core structure which allows the organic semiconductor to become conductive when a charge is injected. This system of conjugated π-bonds forms the polymeric backbone that mediates the charge transfer. Geometry is important for charge transfer as the π orbitals need to have overlap requiring molecules with flat geometry (Fig. 5). The second requirement is for either the core structure or to have functional groups attached that allows the organic semiconductor to become soluble in the proper solvent.[18]

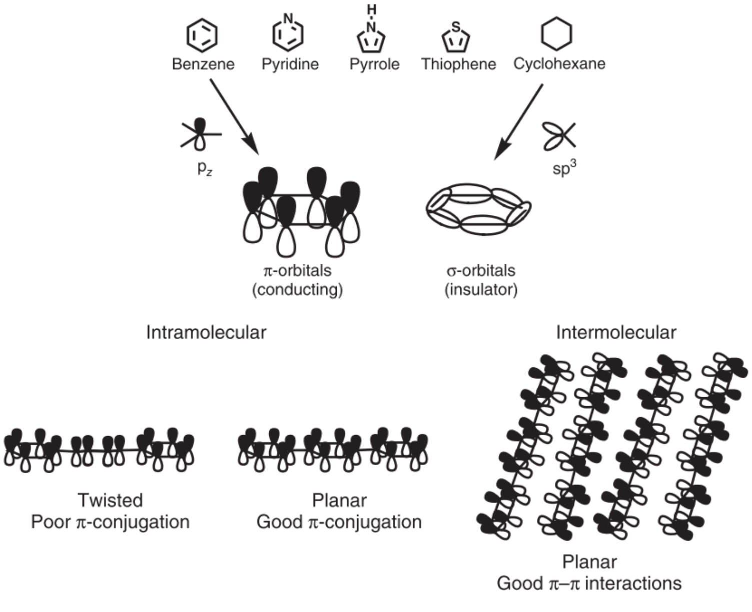

Figure 1.5. Schematic showing the appropriate building blocks for organic molecules with charge conducting capabilities. A requirement is π-conjugation, pure sigma orbitals such as cyclohexane result in insulating properties. Planar molecules have overlapping π orbitals which allows charge to travel through the individual molecule but also allows charge transfer to occur intermolecularly in the setting of a thin-film. *Adapted from reference 11*.

Organic polymers have many promising characteristics for large-area electronic applications. It can be made into an ink solution, deposited through printed means using low temperature processes, and polymers are naturally malleable enough for flexible electronics.[19] One of the earliest and most studied organic semiconductors is polythiophene, consisting of a polymeric backbone of heterocyclic sulfurs. Thin-film transistors of polythiophene could be made through a low temperature solution method with I_{on}/I_{off} ratios of 10^7. The field effect mobility was a low 0.14 $cm^2 \cdot V^{-1} \cdot s^{-1}$ and the I_{on}/I_{off} ratio rapid decreased in presence of oxygen requiring all measurements to be carried out in a nitrogen glovebox.[20] Efforts to improve performance include adding electron delocalizing functional groups and co-monomers, the field effect mobility would only improve up to 0.6 $cm^2 \cdot V^{-1} \cdot s^{-1}$.[21,22] Other organic molecules used such as polypyrrole consisting of fused aromatics with flat geometry giving high density π conjugation have also been developed into an ink to be painted into a thin film. With better air stability than polythiophenes, polypyrrole printed films still suffered from poor hole mobilities of 0.21 $cm^2 \cdot V^{-1} \cdot s^{-1}$.[23] Despite efforts that have been made to develop printed organic polymer based electronic devices for past few decades, lack of ambient stable material and poor electronic performances have prevented any successful commercialization. Although there have been improvements in the field, the general field effect performance of organic semiconductors remains <1 $cm^2 \cdot V^{-1} \cdot s^{-1}$. The poor performance combined with oxygen sensitivity, low temperature tolerance and environmental sensitivity acts as major road blocks preventing wide spread use of such technology.[24]

While organic semiconducting materials encompasses suitable features for printed electronics such as intrinsic flexibility and solution based low-cost processing, the chemical instability and slow switching speeds limits their use to lower-end applications. With the advent of Internet of Things (IoT) and wireless wearable health monitoring, there is a requirement for more robust electronics with faster computation speeds while also maintaining large-scale integration. Inorganic material functional inks offer the perfect middle ground between large-area low end organic molecule electronics and high-performance single crystal silicon chip electronics. Inorganic electronic materials have better switching speeds (charge mobility) combined with superior oxygen and thermal stability. Nanomaterials have been the forefront of material science research in the past decade. The ultra-small size (nanometer in at least on dimension) combined with ability to stabilize with surfactants have allowed nanomaterials to become colloidally suspended into different solvents. New understandings of nanostructured materials combined with surface science has opened the door for inorganic based functional inks for printed electronics.[25]

There are generally three classes of inorganic nanomaterials defined by their anisotropic dimensions. If it is nanometer sized (>100 nm) in all three dimension it is classified as zero-dimensional (0D) (quantum dots, nanoclusters), nanometer sized in two dimensions are classified as one-dimensional (1D) (nanowires, nanotubes) and finally if geometrically nanometer sized in one dimension it is labeled as two-dimensional (2D) (nanosheets, nanoplates). The earliest and most studied nanostructure is the 0D semiconductor quantum dot, the most common are cadmium selenide (CdSe) and lead selenide (PbSe). These are typically synthesized through a bottom-up chemical synthesis involving dissolving the appropriate precursors in solvent, heating it up and then mixing them together through hot-injection. Quantum dots can be colloidally suspended in solution with the appropriate surfactants allowing them to be solution deposited through various printing techniques such as spin-coating, dip-coating, spray-coating, and drop-casting.[26] 1D or one-dimensional nanostructures have one dimension elongated and larger than the other two. Some commonly studied ones are silver nanowires which have been solution processed into transparent conductive films.[27] The most published semiconducting 1D structure are single walled carbon nanotubes, comprising of hexagonal lattice of SP2 carbons rolled up into a seamless cylinder. Carbon nanotubes do not have dangling surface bonds which act as insulating agents for charge transport. Similar to quantum dots, carbon nanotube semiconductors have also been processed through a variety of different solution methods into films.

Both 0D quantum dots and 1D nanotubes are able to be processed into functional inks, they both suffer from large draw backs. Cadmium selenide and lead selenide use toxic metals as their main metal source, and use environmentally hazardous precursors such as Trioctylphosphine (TOP) during the synthesis. For 0D the small size results in films with large amounts of grain boundaries, each acting as an energy barrier for charge transfer (Fig. 6a). The dangling bonds along with the surface ligands required to stabilize 0D colloids form additional transport barriers at the grain boundaries causing charge scattering and recombination which degrades the transport properties. 1D nanostructures can minimize the grain boundaries in a film due to their larger dimensions, but their contacts are only point contacts from one nanostructure to the other. Additionally, the dimensions of 1D creates difficulty in forming a complete film creating inconsistent device performance and restricts its capability to be reproduced over large areas. These limitations confine the use of 1D solution processed films for transparent conductor applications only. Majority of 1D also suffer from dangling bonds similar to 0D which creates interfacial disorders at the contact points (Fig. 6b). While single-walled carbon nanotube is a unique case of a 1D nanostructure without dangling bonds, it is incredibly difficult to separate metallic form from semiconducting. Carbon nanotubes are grown through a chemical vapor deposition process, depending on the chirality they can be either metallic or semiconducting in a ratio of 30:70 where 30 percent are intrinsic metallic conductors.[28] For proper printed electronics the materials need to be pure phase in terms of both geometric and electronic properties.

Two-dimensional or 2D nanostructures such as nanosheets or nanoplates are the most suitable building blocks for solution printed electronic films. These nanosheets have electronic characteristics that range from metallic conductors, semiconductors, and insulators for dielectrics. When solution deposited these colloidal 2D nanostructures tend to lay flat on the substrate forming a uniform film with large overlapping contacts minimizing grain boundaries which results in less energy barriers for superior charge transferring characteristics. Similar to 0D and 1D there are numerous methods of printing 2D colloids such as spin-coating, ink-jet printing, dip-coating, spray-coating and Langmuir-Blodgett trough deposition. The large dimensional size in two different dimensions offers superior film coverage, especially when scaled up to wafer level processing. The ultrathin property of these nanosheets gives them intrinsic flexibility making them suitable for flexible electronics. 2D nanostructured materials can be synthesized from bottom-up methods using chemical precursors or from top-down by breaking the down the weak interlayer bonds. Finally, due to their lack of dangling bonds at the surfaces, there is less interfacial contacts acting as charge scattering sites (Fig. 6c) for better electronic performance.

This thesis will focus on utilizing two-dimensional nanosheet colloids as functional inks for printed electronic thin-films. It will discuss the properties of two-dimensional nanostructures, and different methods to synthesize them. Then some experimental results of bottom-up and a unique top-down electrochemical method to produce 2D nanosheets through bulk crystals. Crystal growth will be employed to produce a series of different layered bulk structure which can be broken down into functional nanosheet inks. Some applications of functional inks from printed nanosheets will be demonstrated in the form of thin-film transistors and superlattices.

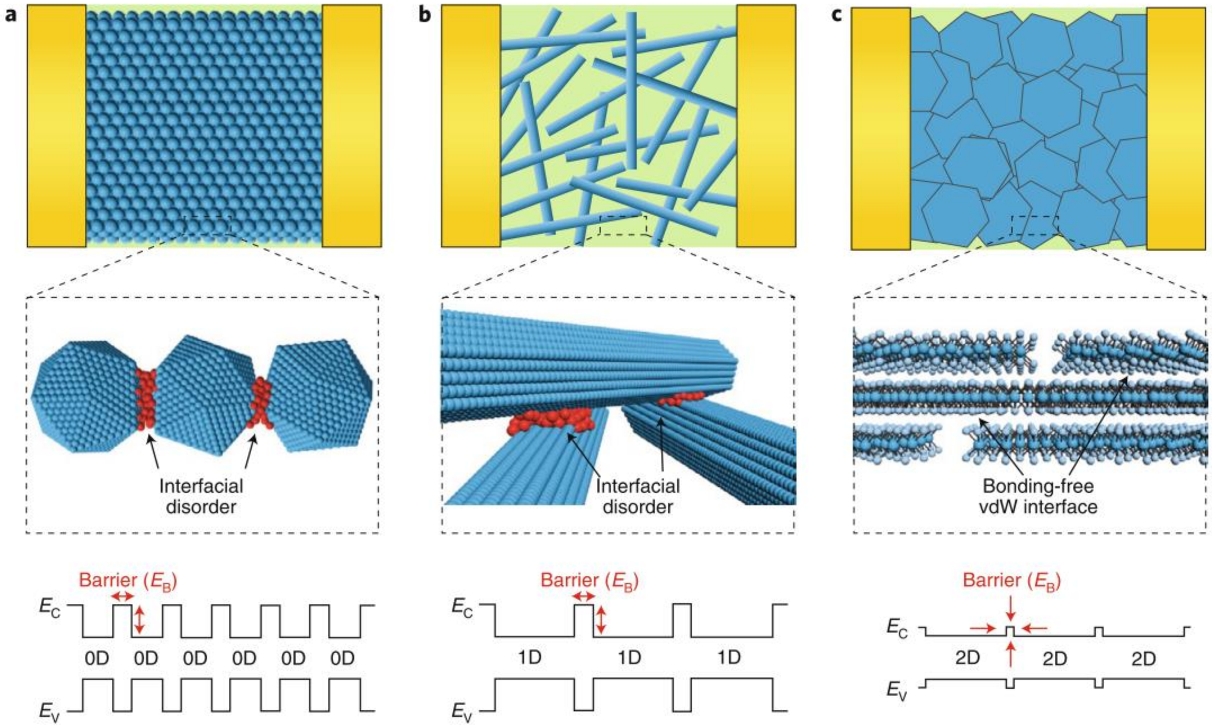

Figure 1.6. Difference in thin-films from 0D, 1D, and 2D. E_C represents conduction band edge energy, E_V represents valence band edge energy, and E_B energy barrier height between the individual nanostructures. (a) A thin-film from 0D quantum dots features complete film coverage but the inherently small size dimension combined with dangling bonds creates several large energy barriers. This ultimately reduces the charge transport. (b) 1D thin-films suffer from incomplete coverage with many blank areas, this limits the applications and makes reproducibility difficult. Similar to 0D the dangling bonds act as heightened energy barriers. (c) Thin-films using 2D as building blocks have several benefits. It has complete film coverage, lower amount of individual grain boundaries. Due to lack of dangling bonds, the charge transfer energy barrier is reduced when compared to 0D and 1D. *Adapted from reference 12.*

1.4 References

1. Arias, A. C.; MacKenzie, J. D.; McCulloch, I.; Rivnay, J.; Salleo, A. *Chem. Rev.* **2010**, 110, 3.
2. Khan, S.; Lorenzelli, L.; Dahiya, R. S. Technologies for Printing Sensors and Electronics Over Large Flexible Substrates: A Review. *IEEE Sens. J.* **2015**, 15, 3164−3185.
3. Someya, T.; Kato, Y.; Sekitani, T.; Iba, S.; Noguchi, Y.; Murase, Y.; Kawaguchi, H.; Sakurai, T. Conformable, Flexible, LargeArea Networks of Pressure and Thermal Sensors with Organic Transistor Active Matrixes. *Proc. Natl. Acad. Sci. U. S. A.* **2005**, 102, 12321–12325.
4. Fukaya, N.; Kim, D. Y.; Kishimoto, S.; Noda, S.; Ohno, Y. OneStep Sub-10 μm Patterning of Carbon-Nanotube Thin Films for Transparent Conductor Applications. *ACS Nano* **2014**, 8, 3285−3293.
5. Barmpakos, D.; Segkos, A.; Tsamis, C.; Kaltsas, G. A Disposable Flexible Humidity Sensor Directly Printed on Paper for Medical Applications. *J. Phys.: Conf. Ser.* **2017**, 931 (1), 012003.
6. Moya, A.; Sowade, E.; del Campo, F. J.; Mitra, K. Y.; Ramon, E.; Villa, R.; Baumann, R. R.; Gabriel, G. All-Inkjet-Printed Dissolved Oxygen Sensors on Flexible Plastic Substrates. *Org. Electron.* **2016**, 39, 168−176.
7. Carey, T.; Cacovich, S.; Divitini, G.; Ren, J.; Mansouri, A.; Kim, J. M.; Wang, C.; Ducati, C.; Sordan, R.; Torrisi, F. Fully Inkjet-Printed Two-Dimensional Material Field-Effect Heterojunctions for Wearable and Textile Electronics. *Nat. Commun.* **2017**, 8, 1202

8. Chen, B.; Jiang, Y.; Tang, X.; Pan, Y.; Hu, S. Fully Packaged Carbon Nanotube Supercapacitors by Direct Ink Writing on Flexible Substrates. *ACS Appl. Mater. Interfaces* **2017**, 9, 28433−28440.
9. Wu, W. Inorganic Nanomaterials for Printed Electronics: A Review. *Nanoscale* **2017**, 9, 7342−7372.
10. Huttunen, O.-H.; Happonen, T.; Hiitola-Keinãnen, J.; Korhonen, P.; Ollila, J.; Hiltunen, J. Roll-To-Roll Screen-Printed Silver Conductors on a Polydimethyl Siloxane Substrate for Stretchable Electronics. *Ind. Eng. Chem. Res.* **2019**, 58, 19909−19916.
11. Lo, L. W.; Shi, H.; Wan, H.; Xu, Z.; Tan, X.; Wang, C. InkjetPrinted Soft Resistive Pressure Sensor Patch for Wearable Electronics Applications. *Adv. Mater. Technol.* **2020**, 5, 1900717.
12. Lin, Z.; Huang, Y.; Duan, X. Van Der Waals Thin-Film Electronics. *Nat. Electron.* **2019**, 2, 378−388.
13. Perelaer, J.; Smith, P. J.; Mager, D.; Soltman, D.; Volkman, S. K.; Subramanian, V.; Korvink, J. G.; Schubert, U. S. Printed electronics: the challenges involved in printing devices, interconnects, and contacts based on inorganic materials. *J. Mater. Chem.* **2010**, 20, 8446.
14. Shimura, F. Single-Crystal Silicon: Growth and Properties, *Springer International Publishing, Cham.* **2017**, 293-307
15. Fisher, G.; Seacrist, M. R.; Standley, R. W. Silicon Crystal Growth and Wafer Technologies. *Proc. IEEE.* **2012**, 100, 1454−1474.
16. Minami, T. Present status of transparent conducting oxide thin-film development for Indium-Tin-Oxide (ITO) substitutes. *Thin Solid Films* **2008**, 516, 5822–5828

17. Lin, Z.; Chen, Y.; Yin, A.; He, Q.; Huang, X.; Xu, Y.; Liu, Y.; Zhong, X.; Huang, Y.; Duan, X. Solution Processable Colloidal Nanoplates as Building Blocks for High-Performance Electronic Thin Films on Flexible Substrates. *Nano Lett.* **2014**, 14 (11), 6547−6553.
18. Caironi, M.; Noh, Y. Y. Large Area and Flexible Electronics; *Wiley-VCH: Weinheim, Germany* **2015**.
19. Matsui, H.; Takeda, Y.; Tokito, S. Flexible and Printed Organic Transistors: From Materials to Integrated Circuits. *Org. Electron.* **2019**, 75, 105432.
20. Ong, B. S.;Wu, Y.; Liu, P.; Gardner, S. High-performance semiconducting polythiophenes for organic thin-film transistors. *J. Am. Chem. Soc.* **2004**, 126, 3378.
21. Pan, H.; Li, Y.; Wu, Y.; Liu, P.; Ong, B. S.; Zhu, S.; Xu, G. Lowtemperature, solution-processed, high-mobility polymer semiconductors for thin-film transistors. *J. Am. Chem. Soc.* **2007**, 129, 4112−4113.
22. McCulloch, I.; Heeney, M.; Bailey, C.; Genevicius, K.; MacDonald, I.; Shkunov, M.; Sparrowe, D.; Tierney, S.; Wagner, R.; Zhang, W.; Chabinyc, M. L.; Kline, R. J.; McGehee, M. D.; Toney, M. F. Liquid-Crystalline Semiconducting Polymers with High Charge-Carrier Mobility. *Nat. Mater.* **2006**, 5, 328–333.
23. Liu, J.; Zhang, R.; Sauve, G.; Kowalewski, T.; McCullough, R.´ D. Highly disordered polymer field effect transistors: N-alkyl dithieno[3,2-b:2′,3′-d]pyrrole-based copolymers with surprisingly high charge carrier mobilities. *J. Am. Chem. Soc.* **2008**, 130, 13167−13176.

24. Newman, C. R.; Frisbie, C. D.; da Silva Filho, D. A.; Bredas, J.-´ L.; Ewbank, P. C.; Mann, K. R. Introduction to Organic Thin Film Transistors and Design of n-Channel Organic Semiconductors. *Chem. Mater.* **2004**, 16, 4436−4451.
25. Talapin, D. V.; Lee, J.-S.; Kovalenko, M. V.; Shevchenko, E. V. Prospects of Colloidal Nanocrystals for Electronic and Optoelectronic Applications. *Chem. Rev.* **2010**, 110, 389−458.
26. Kim, J.-Y.; Kotov, N. A. Charge Transport Dilemma of Solution-Processed Nanomaterials. *Chem. Mater.* **2014**, 26, 134−152.
27. Xu, F. & Zhu, Y. Highly conductive and stretchable silver nanowire conductors. *Adv. Mater.* **2012**, 24, 5117–5122.
28. Wang, W.; Fernando, K. A. S.; Lin, Y.; Meziani, M. J.; Veca, L. M.; Cao, L.; Zhang, P.; Kimani, M. M.; Sun, Y.-P. Metallic SingleWalled Carbon Nanotubes for Conductive Nanocomposites. *J. Am. Chem. Soc.* **2008**, 130 (4), 1415−1419.

Chapter 2. Solution synthesis of colloidal 2D

2.1 Introduction

Since 2004 with the discovery of graphene, later winning the Nobel prize in 2010, the field of two-dimensional materials research has expanded rapidly.[1] New ultrathin materials have been discovered with a assortment of different electrical and optical properties finding new applications such as catalysis, optical devices, electronic devices, energy storage, and biomedical.[2-6] The early days of 2D material creation involved using Scotch tape to mechanically exfoliate layered crystals (Fig. 1). This could make pristine nanosheets with excellent electronic and mechanical properties but could not be scaled up to commercialization.[7,8] There have been some advances in this field such as using low residual tape or thermal release tape to deposit more crystals, but scalability is still a road block. Using mechanical exfoliation alone would limit 2D materials to strictly lab research with no chance of industrial applications.

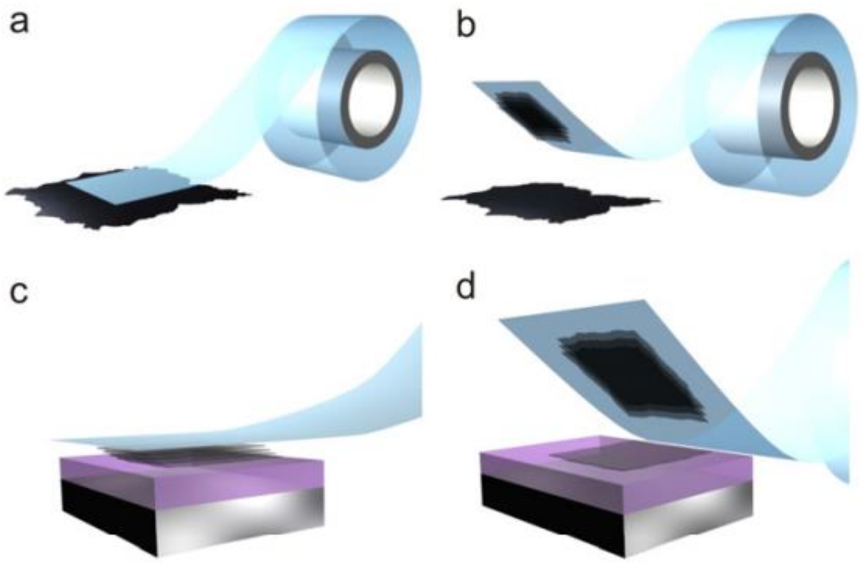

Figure 2.1 Tape exfoliation production of 2D nanostructures. (a) Tape is placed on the surface of a layered crystal. (b) The adhesive on the tape exfoliates layers of the material with nanometer thickness. (c) The tape is placed onto a substrate of choice. (d) Removal of the tape releases the crystals onto the substrate of choice. *Adapted from reference 8.*

Some early attempts to manufacture thin-films using 2D materials was done through chemical vapor deposition.[9] Chemical vapor deposition (CVD) is typically performed in a horizontal tube furnace; the reaction chamber consists of a tube of fused quartz (Fig .2).[10] The precursors are placed on the hot zone of the reaction chamber and a substrate is placed on the cold zone. As the system is heated the precursors vaporize, a carrier gas carries the vapors from the hot end to the colder end where the substrate sits. Chemical vapor deposition involves a reaction occurring in the vapor phase, for deposition processes where there is no chemical reaction is defined as physical vapor deposition. This method is more scalable than mechanical Scotch tape exfoliation but due to reaction chamber size limitations, it cannot be scaled to large area. Additionally, the high temperature of the deposition process also limits the types of substrates that can be used.

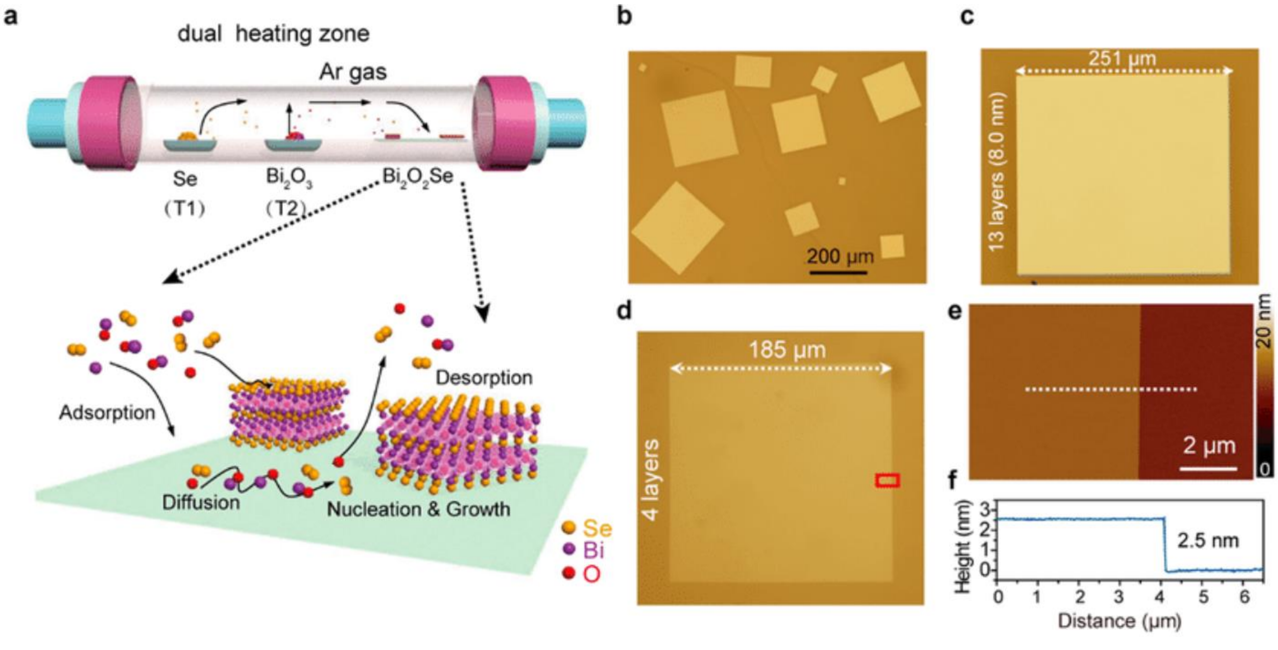

Figure 2.2 Chemical vapor deposition of 2D material. (a) The reaction chamber set up of typical vapor deposition. This is performed in a horizontal tube furnace with argon carrier gas. Selenium and bismuth oxide are the precursors which react in vapor phase before depositing on mica substrate. (b-d) Bi_2O_2Se crystals are grown using CVD. (e and f) Atomic force microscope data showing the thickness of the nanosheets on the nanometer scale. *Adapted from reference 10.*

A current endeavor that is being developed is chemical and physical methods to synthesize nanosheets into a stable colloidal solution. Chemical reaction in solution-phase is one of the leading methods of producing organic molecules and materials on the commercial scale. Using precursors as building blocks to synthesize nanostructured materials is known as bottom-up synthesis.[11] Bottom-up synthesis of nanostructured crystals have been researched for the past several decades, with many of the early focus on 0D quantum dots.[12] Since the early cadmium selenide quantum dots research, this field has developed included to include 1D and 2D structures to further understand quantum confinement effects.[13] Synthesizing nanosheets in solution-phase would allow further processing into functional inks which can then be used alongside printing technology to process into large-area thin-films. In this case the synthesis and the film deposition stages are separate which eliminates any temperature intensive steps allowing room temperature deposition onto a substrate. The challenge has been to synthesize 2D nanocrystals with proper composition, uniform thickness, and low defects.[14] Proper surfactants and reaction solvent must be used otherwise the nanosheets grown will self-assemble into nanoflower clusters (Fig. 3).[15]

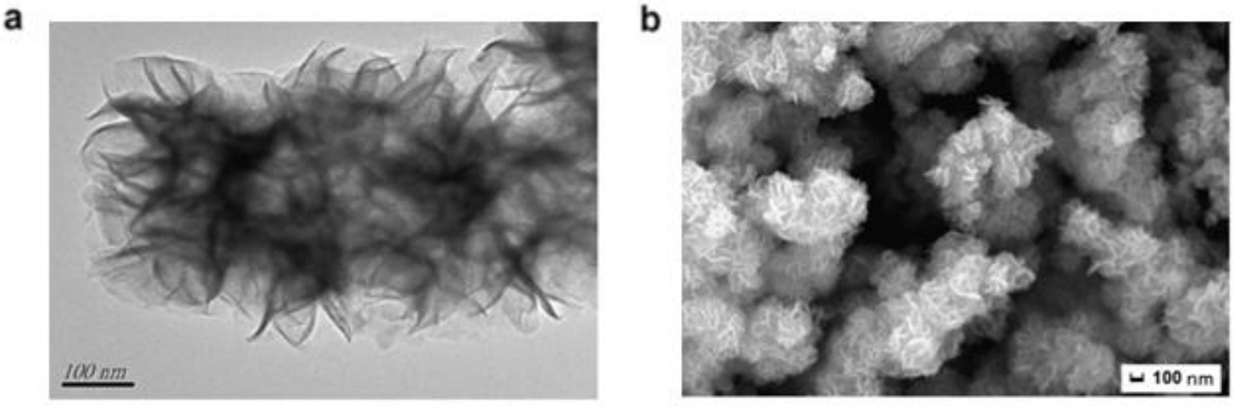

Figure 2.3 Nanoflower clusters of MoS_2. (a) High resolution transmission electron microscope image of an aggregated MoS_2 from solution synthesis. (b) Transmission electron microscope of multiple nanoflower clusters of MoS_2. *Adapted from reference 14.*

The methods of synthesizing two-dimensional nanosheets can be classified by its temperature profile and the method of assembly. For temperature profile there is heat-up and hot-injection. Heat-up generally involves a one pot synthesis and the temperature is ramped until the reaction occurs.[116] Hot-injection has two solutions with two separate precursors. Both are maintained at a specific temperature and while still hot, one is injected into the other.[17] For assembly methods you have self-assembled based on forming 2D phase of the crystal due to being the minima energy crystal structure. The second method is a soft templating assisted assembly. This involves using an oily solvent and using the proper surfactants. The surfactants form a bilayer inverse micelle. The force of the micelle formation assists the growth of nanosheet structure. This has been used to synthesize cadmium selenide from typical 0D nanostructure into 2D nanosheets (Fig .4)[18].

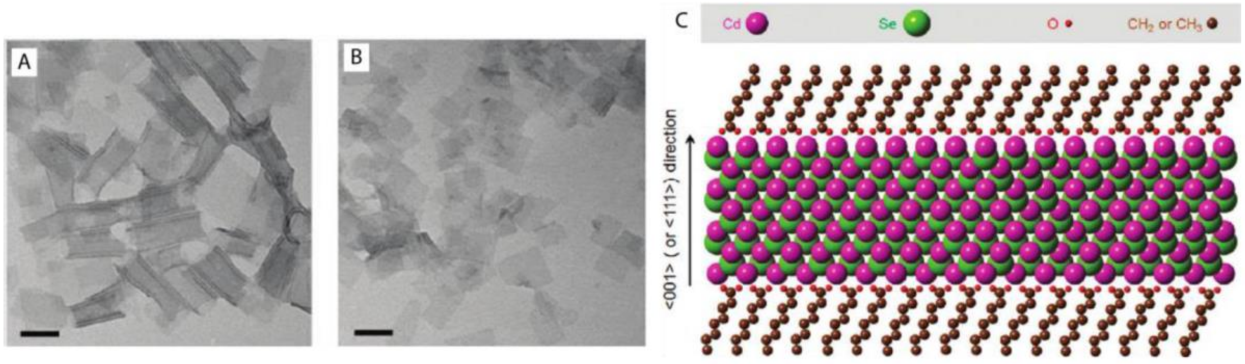

Figure 2.4 Cadmium selenide synthesized through hot-injection soft template method (a and b) CdSe nanosheets synthesized with different lateral dimensions. Here the scale bar is 50nm. (c) The bilayer inverse micelle design. Here the polar heads line up in a sandwich structure while the nonpolar tails interact with the oily solvent. The force of the micelle formation assists the 2D lateral growth of the nanosheet. *Adapted from reference 19.*

Utilizing different solution-phase crystal growth synthetic strategies, different 2D nanostructures can be synthesized. We will discuss two experimental ways of synthesizing 2D nanostructures, here the terms nanosheets and nanoplatelets can be used interchangeably. For bismuth selenide and bismuth telluride (Bi_2Se_3, Bi_2Te_3) a heat-up self-assembled method is used.

This is a simple one pot synthesis employs a polyglycol as the reducing agent and solvent where uniform hexagonal nanosheets grow. Using a similar one-pot method tin monoselenide (SnSe) could be grown by using HMDS as an inverse micelle template growth to produce square shaped nanosheets. Then finally we show how hot-injection can be used to grow indium monoselenide (InSe) nanosheets with triangular shape.

2.2 Experimental

Chemicals: Bismuth nitrate pentahydrate ($Bi(NO_3)_3 \cdot 5H_2O$, >99.9%), Sodium selenite ($NaSeO_3$, >99%), Sodium tellurite ($NaTeO_3$, >99%), Sodium hydroxide (NaOH, >99%), Poly(vinyl pyrrolidone) (PVP, MW≈ 40,000), Ethylene glycol (EG, >99%), Indium (III) chloride ($InCl_3$, 98%), Selenourea ($SeC(NH_2)_2$, 98%), Octadecylamine (ODA,>99%), 1-octadecene (technical grade, 90%), Acetone (practical grade), Toluene (practical grade), Isopropanol (practical grade), Tin(II) chloride ($SnCl_2$, 99%), Selenium (Se, powder ~ 100mesh, >99.5 trace metal basis), tri-n-octylphosphine (TOP, 97%), Oleylamine (OAm, technical grade 70%), hexamethyldisilazane (HMDS, >99%).

Characterization: Characterization was carried out using scanning electron microscopy (SEM, JEOL JSM-6700 FE-SEM) with energy dispersive spectroscopy (EDAX). EDAX was performed to confirm the elemental composition of the nanosheets. Transmission electron microscopy (TEM, T12 Quick CryoEM) was used to image the nanosheets. Samples were prepared by drop casting dilute samples onto copper transmission electron microscope grids. X-ray diffraction (XRD, Panalytical X'Pert Pro X-ray Powder Diffractometer) used to index the crystallinity of the nanosheets. Samples were made by drop casting concentrated nanosheets onto silica wafer substrate.

Synthesis of bismuth selenide nanoplates. This synthesis is not air sensitive and can be done in ambient settings. 0.2 mmol of bismuth nitrate pentahydrate $Bi(NO_3)_3 \cdot 5H_2O$ (0.0970 g), 0.3 mmol $NaSeO_3$ (0,0519 g) and 2 mmol PVP (0.2223 g) were dissolved in 10 mL ethylene glycol with no heating. The reaction vessel used was 30ml glass vials. Once the mixture became homogenous, it was heated in a 190°C oil bath with constant stir. This reaction was carried out for 1.5 hour, the reaction color went from a light yellow to a dark black with a grey shimmering effect indicating the completion of the synthesis. For the washing step, the solution was transferred to a 40ml centrifuge tube with an additional 10 mL acetone and 20mL isopropanol. This mixture was spun at 12 K rpm for 15 minutes. The supernatant was discarded and the sediments were redispersed in 40 mL isopropanol with bath sonication. Once fully dispersed the washing was continued by repeating the centrifuge, discarding supernatant, and redispersing the sediments into isopropanol. The washing steps are done a total of three times. After washing steps were done, the nanosheets were colloidally placed in isopropanol and stable for a month.

Synthesis of bismuth telluride nanoplates: The synthesis of bismuth telluride follows a similar recipe to bismuth selenide. 0.2 mmol $Bi(NO_3)_3 \cdot 5H_2O$ (0.0970 g), 0.3 mmol $NaTeO_3$ (0.0665 g), 4 mmol NaOH (0.1600 g pellets), and 2 mmol PVP (0.223 g) were dissolved in 10 mL ethylene glycol. This mixture was made in 30 mL glass vials and dissolved through sonication with no heat used. Once a homogenous light-yellow solution was formed, a stir bar was placed inside the vial and allowed to react in an oil bath set to temperature of 190 °C. After 1.5 hour of heating and stirring the mixture turned to a dark black with a grey shimmer indicating completion. The vials were removed from the oil bath before cooling to room temperature. The washing steps followed the same procedure as bismuth selenide by centrifuging and redispersing in isopropanol.

Synthesis of indium selenide triangular nanoplates: This synthesis is air sensitive. All precursors were prepared in an argon filled glovebox and reaction takes place on a Schlenk line. This reaction undergoes a hot injection so two separate three-necked flask labeled flask (A) and flask (B). Flask A had 5 ml of octadecylamine and 0.076 mmol of indium (III) chloride (17 mg powder). Flask B was filled with 5ml 1-octadecene and 0.3 mmol of selenourea (37 mg crystalline powder). The flasks were sealed with a rubber septum before being rapidly transferred to a Schlenk line. Flask A and flask B were both lightly heated and vacuum pumped to remove all trace oxygen for 1 hour. After 1 hour of vacuum pumping, argon gas was allowed to flow into both flasks. Flask A was heated to 130 ^{o}C to form a homogenous solution before being cooled down to 100 ^{o}C. During this heating step, flask B was heated to 220 ^{o}C under argon. The contents of flask B were injected into flask A by a glass syringe in a single motion. This reaction mixture was then brough up to 240 ^{o}C with stir and reacted for a total of 1 hour. After 1 hour of reaction the mixture turned into a dark brown color. This mixture was allowed to cool to room temperature with an additional 5 mL of toluene added to prevent aggregation. This whole mixture was placed into a 40ml centrifuge tube with another 25 mL acetone with 2 mmol PVP (0.2223 g) dissolved into the acetone. This whole mixture was sonicated to ensure complete dispersion for 5 minutes. This was then centrifuged at 12 K rpm for 10 minutes. The supernatant was discarded and the sediments were redispersed in isopropanol. The washing was then repeated further by centrifuging and redispersing in isopropanol before finally dispersing the nanosheets in isopropanol.

Synthesis of tin selenide square nanoplates: This synthesis is air sensitive. All precursors were prepared in a glovebox and reaction were done on a Schlenk line. In a scintillation vial, a 1M solution of selenium dissolved in tri-n-octylphosphine by dissolving 10 mmol selenium powder

(760 mg) into 10 mL of TOP. This mixture was sonicated until the selenium was fully dissolved going from a dark mixture into a clear solution. In an argon filled glovebox, a three-neck flask was filled with 20 mL of oleylamine (70%) and 0.21 mmol of $SnCl_2$ (40 mg). This was allowed to mix under constant stir until the tin chloride was fully dissolved. The mixture was vacuum pumped for 1 hour before being covered in argon flow. Using a syringe, 0.22 mL of the 1 M selenium TOP solution was injected in, followed by 1 mL of hexamethyldisilazane (HMDS, 99%). This mixture was heated to 240 °C with constant stirring and allowed to react for a total of 30 minutes. The washing steps followed a similar procedure to indium selenide triangles. The tin selenide nanoplates were first dispersed in acetone mixed with PVP. It then underwent three cycles of centrifuge and isopropanol washes.

2.3 Results and discussion

Both Bi_2Se_3 and Bi_2Te_3 are layered crystals with electronic properties categorized as topological insulators. This class of materials has interesting properties where the bulk material is insulating while the surface is metallic.[20] The crystal structure of Bi_2Se_3 and Bi_2Te_3 are a rhombohedral crystal structure with the space grouping of (R-3*m*). Each layer is five atomic layers forming the basic unit cell with a stoichiometry of 2 bismuth and 3 selenium.[21] Here Bi_2Se_3 was grown using polyglycol as the reducing agent and solvent. The polyvinylpyrrolidone acts as the surfactant and capping agent. This synthesis was simple and possible to do in air requiring only heat with some stir. The x-ray diffraction (XRD) sample was made by spin-coating a thick film on top of silica substrate. The x-ray diffraction showed proper peaks matching with the lattice constants of rhombohedral bismuth selenide (Fig. 5a). Here we only see the (00L) miller lattices being diffracted. This is because of the tendency of the ultrathin two-dimensional nanoplates to favor lying down flat on the substrate.

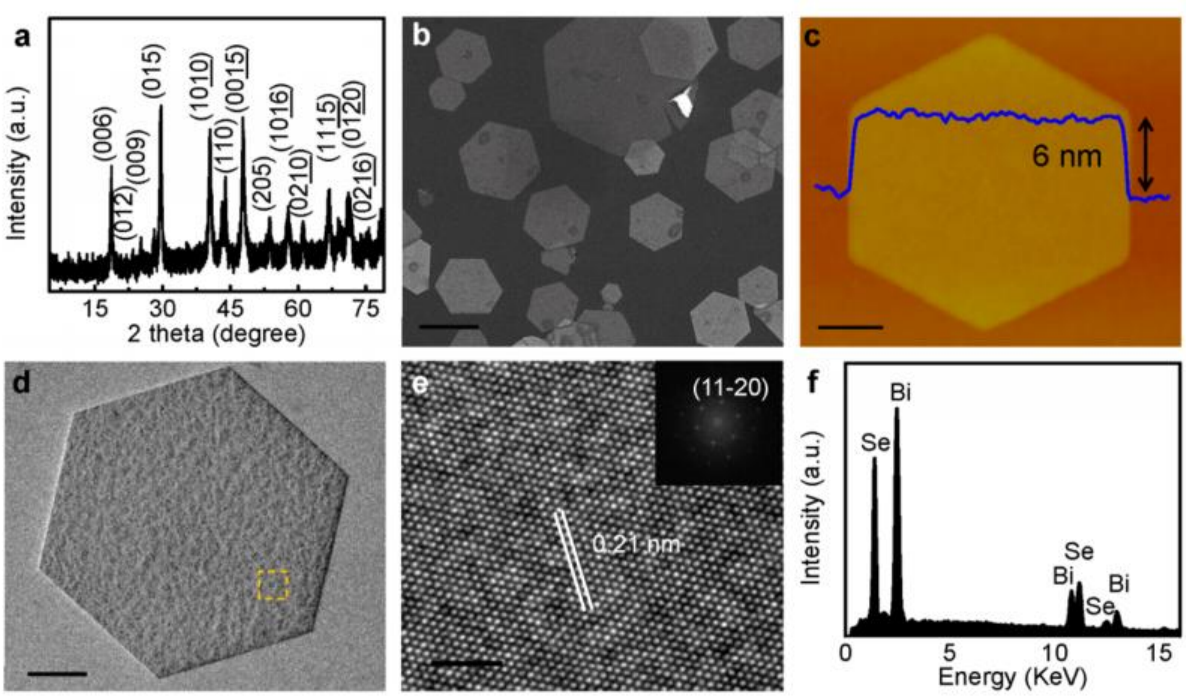

Figure 2.5 Various characterization methods of Bi_2Se_3. (a) Powder x-ray diffraction showing rhombohedral bismuth selenide. (b) SEM image of different sized Bi_2Se_3 nanoplates with hexagon shape. Here we see that some nanoplates can have lateral dimensions greater than one micron. Scale bar is 1000 nm. (c) Atomic force microscope with height profile showing a thickness of only 6 nanometers. Scale bar 300 nm. (d) Transmission electron microscope image showing hexagonal shape. Scale bar 300 nm. (e) High resolution transmission electron microscope of the yellow highlighted portion from the transmission electron microscope. Scale bar 2 nm. Inset is electron diffraction showing high crystallinity. The 0.21 nm matches with the (1120) lattice plane of Bi_2Se_3. (f) Energy dispersive spectroscopy calculating a ratio of 2:3 bismuth to selenium ratio. *Adapted from reference 22.*

Scanning electron microscope images were taken of a dilute sample of bismuth selenide solution deposited on silica. We see hexagonal shaped nanoplates with some sizes as large as 3 micrometers (Fig. 5b). A single nanoplate was isolated from the solution to measure the thickness. Using atomic force microscopy, the thickness of Bi_2Se_3 nanoplates synthesized through polyglycol reduction was on average 6 nm (Fig. 5c). Transmission electron microscope (TEM) was performed to show the uniform hexagonal structure (Fig. 5d). Following TEM, high-resolution TEM was performed to show highly ordered crystalline structure. The energy dispersive spectroscopy was used to show the elemental ratio of the nanosheets (Fig. 5f). The 2:3 ratio of bismuth to selenium gives further evidence that Bi_2Se_3 was successfully synthesized through a solution based polyglycol synthesis.

A single layer of indium selenide (InSe) consists of 4 atoms with the order being Se-In-In-Se. Indium is bonded to another indium with a 4^+ total charge and selenium with 2^- each. InSe is a direct bandgap semiconductor with potential application in electronic and optoelectronic applications.[23] This synthesis involved two different flasks with one containing indium precursor and the other containing selenium. Selenourea was used in place of pure selenium due to the difficulty of dissolving elemental selenium. One challenge of the synthesis was to avoid any oxygen to prevent early oxidation of the precursors. A hot injection is performed to start the nucleation process and then the mix is heated to allow further grow. The InSe nanoplates were grown with triangular shape. The InSe solution was washed to remove any excess solvents. For the first washing step it was necessary to rinse in acetone with PVP. Without the PVP the InSe nanoplate triangles would rapidly aggregate.

After washing a sample was made for x-ray diffraction by concentrating the nanoplates and depositing a thick film on top of a silica substrate. The XRD showed matching diffraction peaks, especially the (00l) series matching bulk pristine indium monoselenide (Fig. 6a). The (002), (004), and (006) matches with the lattice parameter of InSe (a = 0.400 nm). Indium selenide can exist as either InSe or In_2Se_3, both of these have different crystal structures and different electronic properties. Using energy dispersive x-ray spectroscopy to analyze the elemental composition gives further evidence that InSe was successfully made. The ratio between indium and selenium was 1:1 showing that InSe was made instead of In_2Se_3 (Fig. 6b).

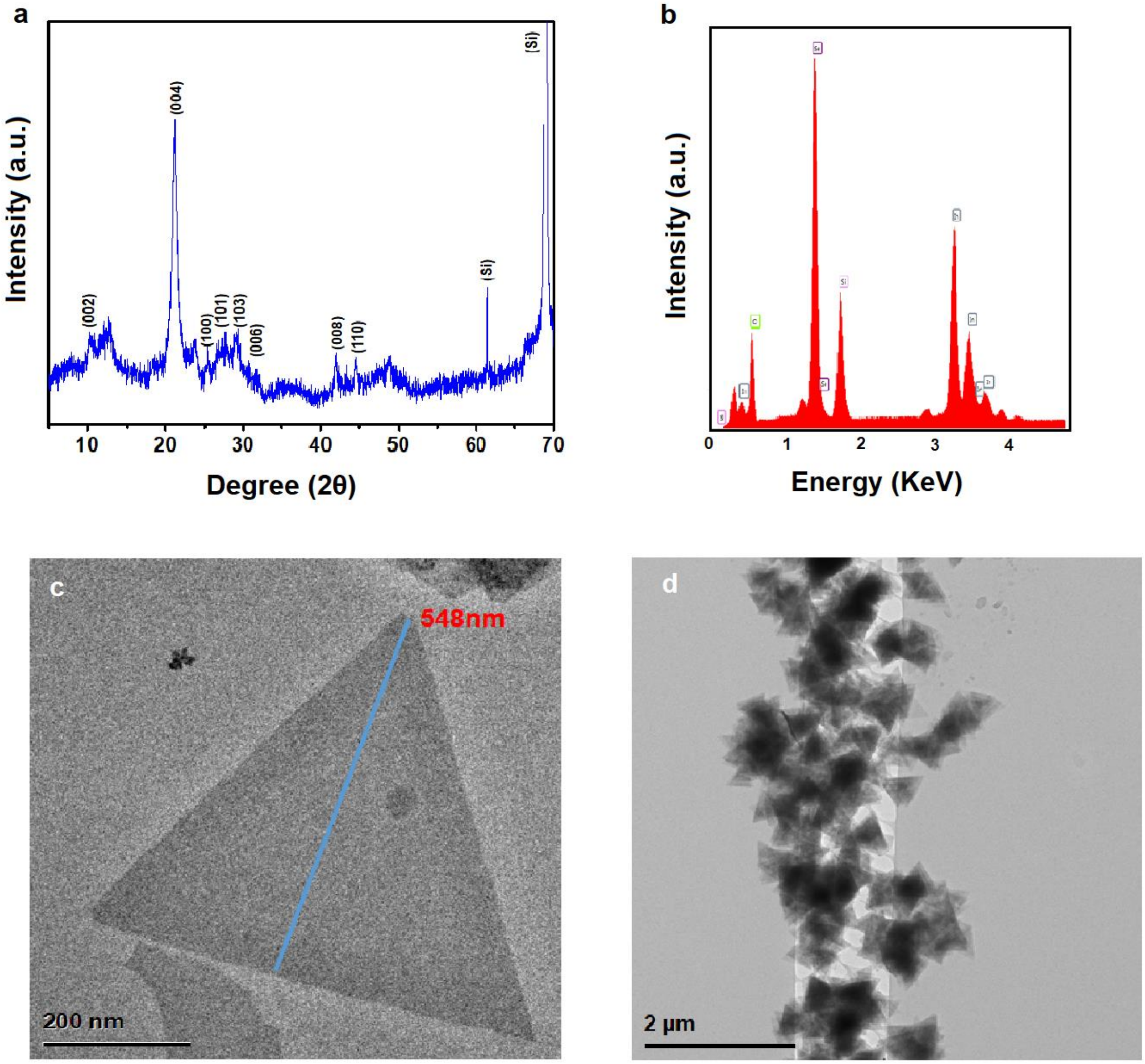

Figure 2.6 Characterization of InSe nanoplates. (a) Powder X-ray diffraction data of an InSe film showing matching peaks with pristine InSe. (b) Energy dispersive spectroscopy to give an elemental composition of the nanoplates. The ratio here was calculated to be 1:1 indium to selenium. (c) Transmission electron microscope image of a single triangular nanoplate of InSe. The lateral size of the nanoplates were on average 550 nm. (d) Scanning electron microscope image showing multiple samples of InSe triangular nanoplates. The size was very uniform.

To image the nanoplates, transmission electron microscopy was performed. The average shape of the nanoplates were 550 nm (Fig. 6c). The shape was that of an equilateral triangle. Scanning electron microscope was performed on a large sample of InSe naonplates. The microscope data shows that the size and shape were uniform throughout the sample.

Tin monoselenide, SnSe is a p-type semiconducting layered material with promising thermoelectric applications.[24] The crystal structure of SnSe is orthorhombic with the space grouping (Pnma) resembling a distorted NaCl.[25] Similar to indium monoselenide, the synthesis of SnSe is air sensitive requiring precursors to be prepared in a glovebox and the reaction carried out on a Schlenk line. After the reaction the resulting grey solution was washed in a similar process as InSe. Acetone with PVP was needed to further disperse the nanoplates otherwise complete aggregation was seen in 10 minutes. This synthesis was a one pot method, using TOP-Se to assist in dissolving the selenium and HMDS as a surfactant.

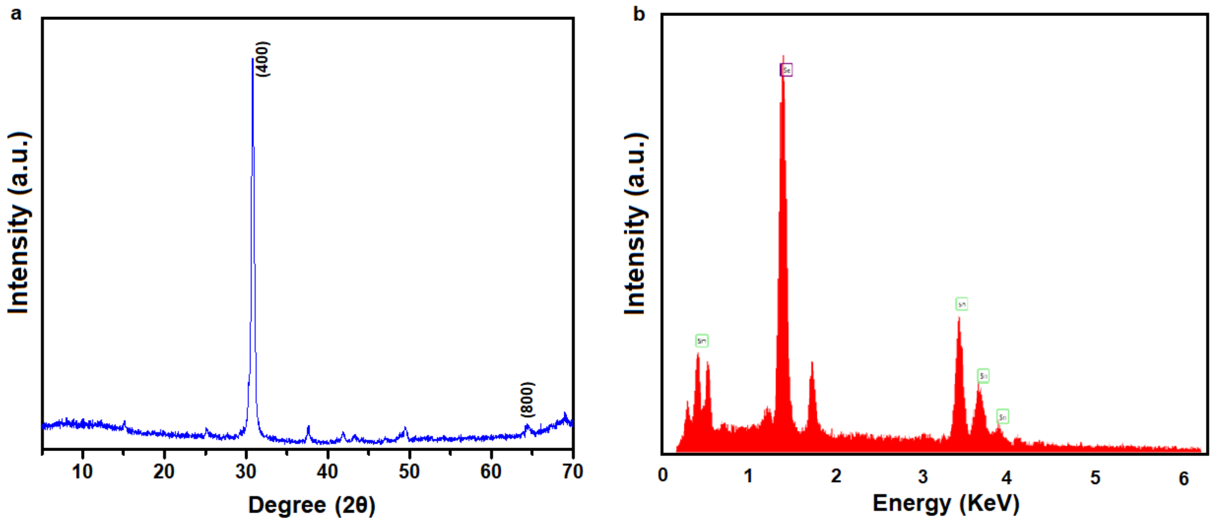

Figure 2.7 Characterization of SnSe. (a) X-ray diffraction is in good agreement with orthorhombic SnSe. (b) Energy dispersive spectroscopy shows a 1:1 ratio of tin and selenium.

After the washing steps, the SnSe was concentrated and deposited onto a silica substrate for x-ray diffraction. The main peaks (400) and (800) are in good agreement with literature values of SnSe diffraction peaks (Fig. 7a).[26] In addition to XRD, energy dispersive spectroscopy was also performed to further prove SnSe was made instead of variations such as $SnSe_2$. From the energy dispersive spectroscopy, we can calculate a ratio of 1:1 of tin to selenide.

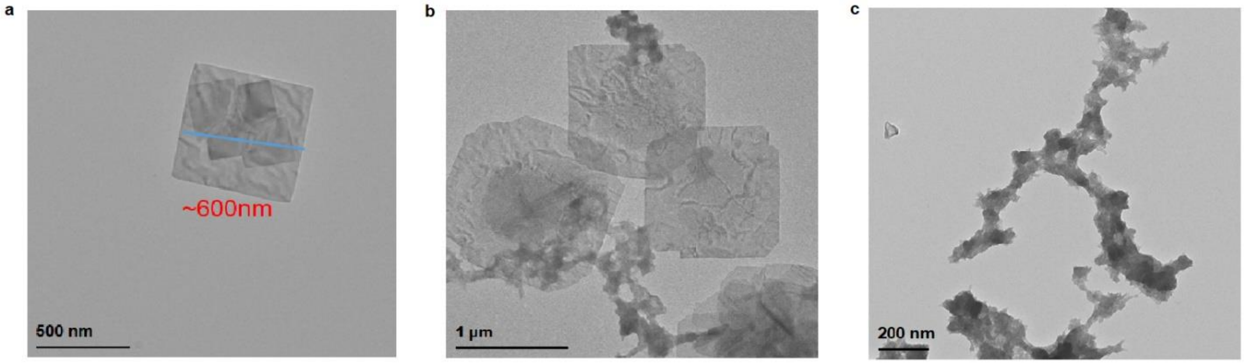

Figure 2.8 Electron microscope imaging of SnSe. (a) Transmission electron microscope of a single nanoplate. The nanoplate was square in shape and had smaller square nanoplates growing epitaxially (b) Several nanoplates with large sizes up to 1 micrometer. We once again see smaller plates growing epitaxially on the larger nanoplates. (c) Transmission electron microscope image of synthesis exposed to oxygen. This synthesis was purposely exposed to oxygen to see the effects it had on the synthesis.

To image the nanoplates, transmission electron microscope was performed. The nanoplates were square in shape and have sizes ranging from 500 nm to 1 micrometer. From transmission electron microscope the shapes were square nanoplates (Fig. 8a). The square nanoplates acted as templates for further crystals to grow atop of them. The size of the nanoplates could grow as large as a full micrometer (Fig. 8b). One difficulty of the synthesis was to keep everything oxygen free. Small oxygen impurities resulted in large amounts of aggregation instead of growing square shaped nanoplates (Fig. 8c). This would spin-coat extremely poor films with lots of aggregation and no uniformity. The transmission electron microscope images along with x-ray diffraction and energy dispersive x-ray spectroscopy shows that SnSe was successfully synthesized through a one-pot solution method. The colloidal nanoplates could be successfully be dispersed in isopropanol solution to be spin-coated onto different substrates.

2.4 Conclusion

Here we have successfully synthesized a variety of nanosheets using different bottom-up solution-based methods. Bi_2Se_3, InSe, and SnSe were all synthesized from raw precursors using chemical reactions and their resulting nanostructure shapes were very different due to their crystal structures. Bi_2Se_3 and Bi_2Te_3 were made in a simple ambient environment one-pot heat-up synthesis. The whole process took no more than 2 hours with washing included. SnSe synthesis was also very facile using one-pot heat-up, only difference is the need to degas the reaction system due to oxygen sensitivity. Here the HMDS acted as a soft template to drive the 2D growth. InSe shows we can utilize a hot-injection method then allowing the crystals to grow to synthesize 2D nanostructures. All of the 2D nanoplates made were successfully characterized using x-ray diffraction to show they had correct crystal lattices, and energy dispersive X-ray spectroscopy to calculate correct elemental composition. Transmission electron microscope along with scanning electron microscope was used to image the flakes individually and show uniformity in shape among a population. The nanoplates could all be successfully dispersed into solution for solution deposition. From the microscope images and diffraction data we see that all the nanoplatelets had a tendency to lay flat on the substrates. This is the preferred position for energy minima interaction between the plates face and the substrate. Lying flat onto a substrate means it is promising for forming a fully covered film where the active material has good overlapping contact to facilitate charge transfer. These studies further push bottom-up colloidal nanosheet to be used for printed based electronics.

2.5 References

1. Novoselov, K. S.; Geim, A. K.; Morozov, S. V.; Jiang, D.; Zhang, Y.; Dubonos, S. V.; Grigorieva, I. V.; Firsov, A. A. Electric Field Effect in Atomically Thin Carbon Films. *Science* **2004**, 306, 666–669.
2. Roy, T.; Tosun, M.; Kang, J. S.; Sachid, A. B.; Desai, S. B.; Hettick, M.; Hu, C. C.; Javey, A. Field-Effect Transistors Built from All Two-Dimensional Material Components. *ACS Nano* **2014**, 8, 6259− 6264.
3. Kong, N.; Ji, X.; Wang, J.; Sun, X.; Chen, G.; Fan, T.; Liang, W.; Zhang, H.; Xie, A.; Farokhzad, O. C.; Tao, W. ROS-Mediated Selective Killing Effect of Black Phosphorus: Mechanistic Understanding and Its Guidance for Safe Biomedical Applications. *Nano Lett.* **2020**, 20, 3943−3955.
4. Xia, F.; Wang, H.; Xiao, D.; Dubey, M.; Ramasubramaniam, A. Two-Dimensional Material Nanophotonics. *Nat. Photonics* **2014**, 8, 899−907.
5. Pomerantseva, E.; Gogotsi, Y. Two-dimensional heterostructures for energy storage. *Nat. Energy* **2017**, 2, 17089.
6. Chia, X.; Pumera, M. Characteristics and Performance of TwoDimensional Materials for Electrocatalysis. *Nat. Catal.* **2018**, 1, 909− 921.
7. Frank, I. W.; Tanenbaum, D. M.; van der Zande, A. M.; McEuen, P. L. Mechanical Properties of Suspended Graphene Sheets. *J. Vac. Sci. Technol. B.* **2007**, 25, 2558–2561.
8. Novoselov, K. S.; Neto, A. H. C. Two-Dimensional CrystalsBased Heterostructures: Materials with Tailored Properties. *Phys. Scr.* **2012**, 2012, 014006.

9. Cai, Z.; Liu, B.; Zou, X.; Cheng, H. M. Chemical Vapor Deposition Growth and Applications of Two-Dimensional Materials and Their Heterostructures. *Chem. Rev.* **2018**, 118, 6091−6133
10. Wu, J.; Qiu, C.; Fu, H.; Chen, S.; Zhang, C.; Dou, Z.; Tan, C.; Tu, T.; Li, T.; Zhang, Y.; Zhang, Z.; Peng, L. M.; Gao, P.; Yan, B.; Peng, H. Low Residual Carrier Concentration and High Mobility in 2D Semiconducting Bi2O2Se. *Nano Lett.* **2019**, 19, 197−202
11. Langille, M. R.; Personick, M. L.; Zhang, J.; Mirkin, C. A. Bottom-Up Synthesis of Gold Octahedra with Tailorable Hollow Features. *J. Am. Chem. Soc.* **2011**, 133, 10414−10417.
12. Murray, C. B.; Norris, D. J.; Bawendi, M. G. Synthesis and Characterization of Nearly Monodisperse Cde (E = Sulfur, Selenium, Tellurium) Semiconductor Nanocrystallites. *J. Am. Chem. Soc.* **1993**, 115 (19), 8706−8715.
13. Cheng, P.; Sun, L.; Feng, L.; Yang, S.; Yang, Y.; Zheng, D.; Zhao, Y.; Sang, Y.; Zhang, R.; Wei, D.; et al. Colloidal Synthesis and Optical Properties of All-Inorganic Low-Dimensional Cesium Copper Halide Nanocrystals. *Angew. Chem., Int. Ed.* **2019**, 58, 16087.
14. Nasilowski, M.; Mahler, B.; Lhuillier, E.; Ithurria, S.; Dubertret, B. Two-Dimensional Colloidal Nanocrystals. *Chem. Rev.* **2016**, 116, 10934−10982.
15. Tang, G.; Sun, J.; Wei, C.; Wu, K.; Ji, X.; Liu, S.; Tang, H.; Li, C. Synthesis and Characterization of Flowerlike MoS2 Nanostructures through CTAB-Assisted Hydrothermal Process. *Mater. Lett.* **2012**, 86, 9−12
16. Park, K. H.; Choi, J.; Kim, H. J.; Oh, D.-H.; Ahn, J. R.; Son, S. U. Unstable Single-Layered Colloidal TiS2 Nanodisks. *Small* **2008**, 4 (7), 945−950.

17. Huang, J. M.; Kelley, D. F. Synthesis and Characterization of MoSe2 and WSe2 Nanoclusters. *Chem. Mater.* **2000**, 12 (10), 2825− 2828.
18. Son, J. S.; Wen, X.-D.; Joo, J.; Chae, J.; Baek, S.; Park, K.; Kim, J. H.; An, K.; Yu, J. H.; Kwon, S. G.; et al. Large-Scale Soft Colloidal Template Synthesis of 1.4 Nm Thick CdSe Nanosheets. Angew. *Chem., Int. Ed.* **2009**, 48 (37), 6861−6864.
19. Li, Z.; Peng, X. Size/Shape-Controlled Synthesis of Colloidal CdSe Quantum Disks: Ligand and Temperature Effects. *J. Am. Chem. Soc.* **2011**, 133, 6578−6586.
20. Liu, S.; Kim, Y.; Tan, L. Z.; Rappe, A. M. Strain-induced ferroelectric topological insulator. *Nano Lett.* **2016**, 16 (3), 1663− 1668.
21. Zhang, W.; Yu, R.; Zhang, H.-J.; Dai, X.; Fang, Z. First-principles studies of the three-dimensional strong topological insulators Bi2Te3, Bi2Se3 and Sb2Te3 *New J. Phys.* **2010**, 12, 065013.
22. Lin, Z.; Chen, Y.; Yin, A.; He, Q.; Huang, X.; Xu, Y.; Liu, Y.; Zhong, X.; Huang, Y.; Duan, X. Solution Processable Colloidal Nanoplates as Building Blocks for High-Performance Electronic Thin Films on Flexible Substrates. *Nano Lett.* **2014**, 14, 6547−6553.
23. Lauth, J.; Gorris, F. E. S.; Samadi Khoshkhoo, M.; Chasse, T.;´ Friedrich, W.; Lebedeva, V.; Meyer, A.; Klinke, C.; Kornowski, A.; Scheele, M.; Weller, H. Solution-Processed Two-Dimensional Ultrathin InSe Nanosheets. *Chem. Mater.* **2016**, 28, 1728−1736.
24. Qin, B. C.; Wang, D. Y.; He, W. K.; Zhang, Y.; Wu, H. J.; Pennycook, S. J.; Zhao, L. D. Realizing high thermoelectric performance in p-type SnSe through crystal structure modification. *J. Am. Chem. Soc.* **2019**, 141, 1141−1149.

25. Shi, W.; Gao, M.; Wei, J.; Gao, J.; Fan, C.; Ashalley, E.; Li, H.; Wang, Z. Tin selenide (SnSe): growth, properties, and applications. *Adv. Sci.* **2018**, 5, 1700602.

26. Vaughn, D. D.; In, S.-I.; Schaak, R. E. A Precursor-Limited Nanoparticle Coalescence Pathway for Tuning the Thickness of Laterally-Uniform Colloidal Nanosheets: The Case of SnSe. *ACS Nano* **2011**, 5, 8852−8860.

Chapter 3 Top-down electrochemical intercalation synthesis of nanosheets

3.1 Introduction

A unique characteristic of 2D materials is the fact that they form the building blocks of layered bulk materials, many naturally occurring such as graphite or molybdenum disulfide.[1,2] This means that 2D nanosheets can not only be made from bottom-up synthesis using precursors and chemical reactions but also, they can be created top-down by breaking bulk layered materials into their distinct building blocks.[3] For bulk layered crystals the chemical bonds within an individual layer (intralayer) consists of covalent bonds, but in between the different stacked layered (interlayer) is a weaker van der Waals interaction.[4] This weaker interlayer attraction is what allows graphite to be used as writable material in pencil lead. There are two strategies for solution-phased top-down exfoliation of bulk crystals to 2D nanosheets. One is known as pure liquid exfoliation another is intercalation and exfoliation (Fig. 1).

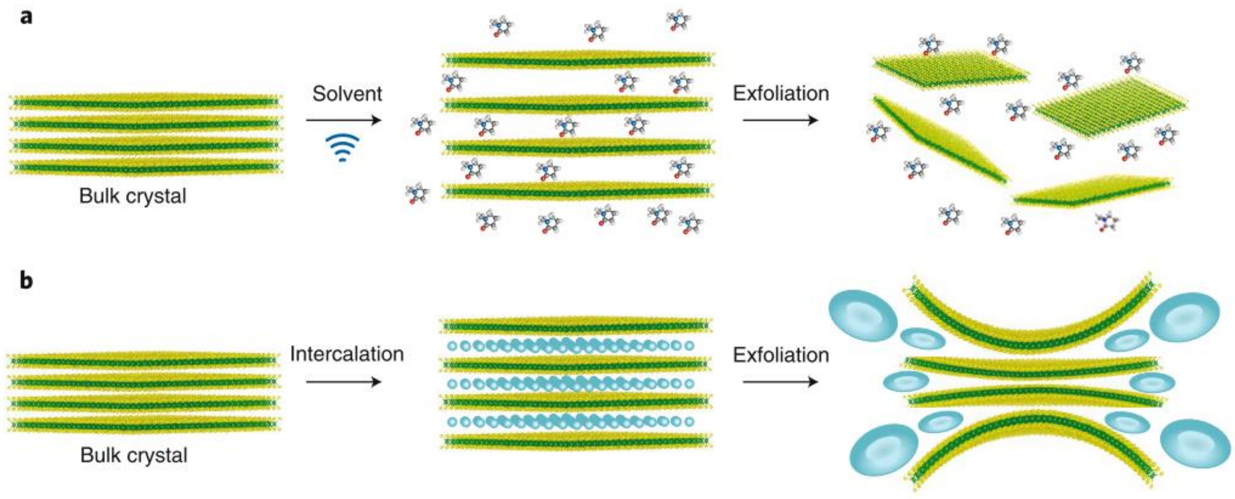

Figure 3.1 The two different methods of solution based top-down 2D nanosheet production. (a) Pure liquid exfoliation using appropriate solvent and high-powered sonication to rip apart the weakly bound nanosheets. (b) Intercalation and exfoliation involve first inserting a foreign molecule in between the layers to further diminish the van der Waals interaction making it easier to exfoliate.

Pure liquid exfoliation is the simplest method and cheap. It involves using a suitable solvent and high-powered probe sonicator to pulverize the bulk layered crystal into individual nanosheets. It has been found that the most appropriate solvents have matching surface tension as the surface energy of the bulk material.[5] Having the correct surface interaction allows the solvent to strongly interact with the layers to rip them apart. There have been numerous different 2D nanostructured materials made through this method such as graphene, boron nitride, transition metal dichalcogenides (TMDC), and layered oxides.[7-11] While this method can work on a variety of different bulk layered crystals, their resulting nanosheets produced are uneven in thickness distribution and highly defective due to the rough sonication which physically rips the layers apart.[12] MoS_2 films produced by pure liquid phase exfoliation showed mobility 10^{-4} $cm^2 \cdot V^{-1} \cdot s^{-1}$. This limitation prevents liquid phase exfoliation from being used to make commercially viable thin-films of electronic grade.

An alternative method to reduce the power in the defect causing sonication step is to first weaken the layer interaction. This is done by inserting foreign molecules into the host bulk layered crystal which further separates and weakens the van der Waal attraction, this is known as intercalation.[13] This can be done because between the layers is a lack of covalent chemical bonds, the van der Waals interaction is essentially a gap. The ability for layered crystals to insert molecules in between the layers is a core property of lithium-ion batteries where graphite is used as a layered host for lithium ions. Similar to pure liquid phase exfoliation, intercalation exfoliation can also produce a variety of different 2D materials such as graphene, transition metal dichalcogenides and layered phosphides.[14-17] Weakening the interlayer van der Waal attraction allows for a milder sonication or other expansion methods. The gentler exfoliation method results in nanosheets with more pristine qualities.

The typically used method of intercalation exfoliation involves the insertion of alkali metals.[18] Generally n-butyllithium is used as lithium source. Lithium inserts itself into the layers of a bulk layered material such as molybdenum disulfide. After intercalation, the bulk crystal is placed into water so that the lithium may react and form lithium hydroxide, this chemical reaction will create large expansion and exfoliate the layers (Fig. 2).[19,20]

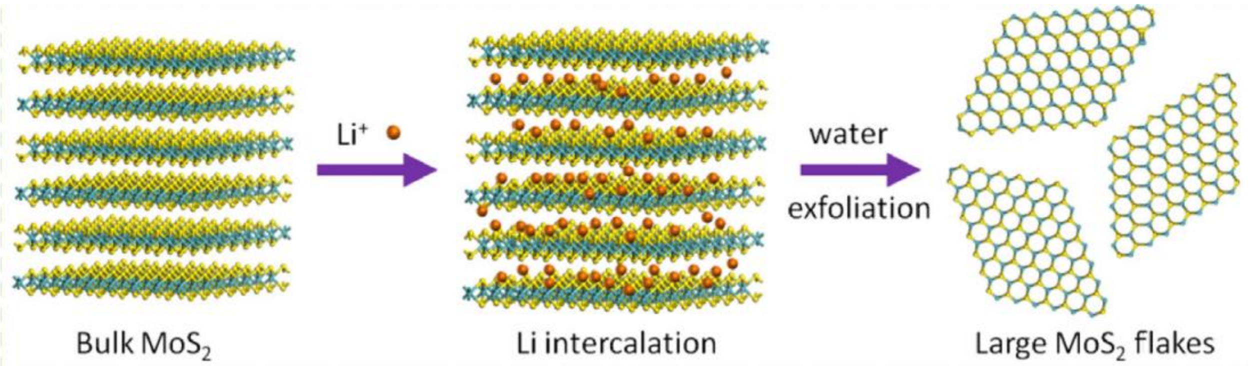

Figure 3.2 Typical process of intercalation and exfoliation involves the use of small alkali metal ions such as lithium. The lithium ion intercalates into the layers of the host layered material. After exposure to water, the rapid reaction of lithium into lithium hydroxide creates large expansion which exfoliates the layers. *Adapted from reference 20.*

This lithium intercalation and rapid expansion by reacting with water does create nanosheets and can produce nanosheets much quicker than pure liquid phase exfoliation. This rapid exfoliation and formation of lithium hydroxide unfortunately creates defects and oxygen vacancy sites on the molybdenum disulfide nanosheets. This results in film with a poor charge mobility of 0.04 $cm^2 \cdot V^{-1} \cdot s^{-1}$.[21] Another issue with smaller alkali metal is that it causes phase shift for certain materials such as MoS_2. Molybdenum disulfide in its naturally occurring form is 2H semiconducting, but when lithium is intercalated, it has a crystal structure phase shift into 1T which is intrinsically metallic.[22] This makes processing pure phase electronic thin films impossible. Additional treatment steps are required to revert the 1T phase MoS_2 back to original 2H phase.

The insertion of a Li^+ ion is followed with an electron being ejected into the MoS_2 host material. This injected electron is injected into the d-orbital of the molybdenum atom, which changes the oxidation state of molybdenum from 4^+ to a more negative state. This oxidation state change causes the phase change from 2H to 1T.[23,24] Based on theoretical studies a phase transition happens when electron injection surpasses a threshold, calculated to 0.29 electron per a formula unit of MoS_2.[25,26] The goal here is instead to intercalate a large organic molecule to reduce the total electron injected. Li^+ ions have a diameter of 2 Å, whereas larger tetraheptylammonium bromide (THAB) ions have a diameter of 20 Å. In terms of packing density, the THAB molecule would occupy 100 times the space in place of lithium ions. This large molecular size means a large amount of energy is required to insert between the layers requiring it to be done via an electric potential. Here we show that tetraheptylammonium ions can be intercalated into layered MoS_2 host driven by an electrochemical cell. Afterwards, the intercalated MoS_2 can be readily exfoliated down into nanosheets and processed into electronic thin-films.

3.2 Experimental

Chemicals: Bulk molybdenum disulfide (MoS_2), Acetonitrile (ACN, 99.8%), Tetraheptylammonium bromide (THAB, 98%), Dimethylformamide (DMf, 99.8%), Poly(vinyl pyrrolidone) (PVP, MW≈ 40,000), Isopropanol (practical grade), Graphite rod (low density, 99.995% trace metal basis), Bis(trifluoromethane)sulfonimide (TFSI, 95%). All chemicals were bought from Sigma-Aldrich except THAB which was bought from Alfa Aesar. The purchased chemicals were used as arrived with no additional modifications. Graphite rod was cut into appropriate sizes for the electrochemical cell.

Intercalation and exfoliation of MoS_2 into nanosheet ink. Starting with 40 mL of acetonitrile, 200 mg of THAB of added and mixed until a homogenous solution was formed. This acted as the electrolyte for the electrochemical cell setup. A thinly cleaved MoS_2 was cut with a razor from a bulk MoS_2. On average the MoS_2 cleaved was about 0.3 mm in thickness. The MoS_2 was attached to an 18-gauge copper wire by conductive copper tape. This was the cathode electrode in the cell, a negative bias was applied to the MoS_2. The negative applied voltage on the MoS_2 forced the insertion of tetraheptylammonium ions into the layered bulk crystal. This was a simple two electrode electrochemical cell; the counter electrode was a graphite rod. A voltage was applied through the use of a variable power supply, the negative lead connected to the MoS_2 (Cathode) and the positive lead (Anode) was attached to the graphite rod. The typical voltage used was 7 volts, this high potential allowed for a rapid intercalation process. Total intercalation time was 1 hour.

Under the applied voltage, the MoS_2 crystal could be seen visibly expanding. After 1 hour intercalation, the enlarged MoS_2 was removed from the electrochemical cell and placed into a separate beaker. Into this glass beaker 40 mL of dimethylformamide was added alongside with 8 mmol PVP (0.8889g). This was then sonicated in a bath sonicator for another 1 hour. As the mixture was sonicated, the solution went from a clear to a dark greenish black with a silver shimmer effect. This was collected into a 40 mL centrifuge tube and initially spun at 3 K rpm for 3 minutes to sediment any larger pieces that did not properly exfoliate. The black supernatant was collected and recentrifuged at 12 K rpm for 15 minutes. The clear supernatant was disposed and the silver sediment was redispersed in isopropanol to wash excess PVP. Centrifugation at 12 K rpm for 15 minutes and redispersion in isopropanol was repeated a total of 3 times. Finally, the MoS_2 nanosheets were concentrated down to 1.5 mL in isopropanol.

Film deposition and electronic measurements. Optical absorption with Beers law was used to normalize concentration between different MoS_2 ink samples. The ink solution was diluted by a factor of 50 and the absorption peak at 440 nm was normalized to 0.70. SiO_2/Si substrates were cleaned with isopropanol and treated with oxygen plasma for 5 minutes. The ink solution was then deposited onto SiO_2/Si substrate through spin coating at 2000 rpm for a total of 3 layers. This formed a uniform thin-film with a green color sheen. When making a film on polyimide film substrate, a solution of polyimide was first coated onto the film and then allowed to cure. The deposited films were then treated with 10 mg ml^{-1} bis(trifluoromethane)sulfonimide (TFSI) in 1,2-dichloroethane at 80 °C for 1 h to repair any sulfur vacancy defects. This was done by submerging the films into the TFSI solution while placed into an oven. Finally, to get rid of any remaining organics on the surface, the films were annealed in a tube furnace under constant argon atmosphere.

Thin-film transistors were fabricated through standard cleanroom using photolithography, reactive ion dry etch, and e-beam metal evaporation process. Typically, the electrodes used for source and drain were 30 nm of titanium capped off with 50 nm gold. To test single flake devices, electron beam lithography was used to pattern the source and drain. The electrodes for single flake device are the same as the thin-film transistor metals. Devices fabricated on polyimide plastic substrate, 60 nm of Al_2O_3 was deposited through atomic layer deposition to form top-gate devices. The entire process of intercalation, exfoliation and film deposition is shown in (Fig. 3)

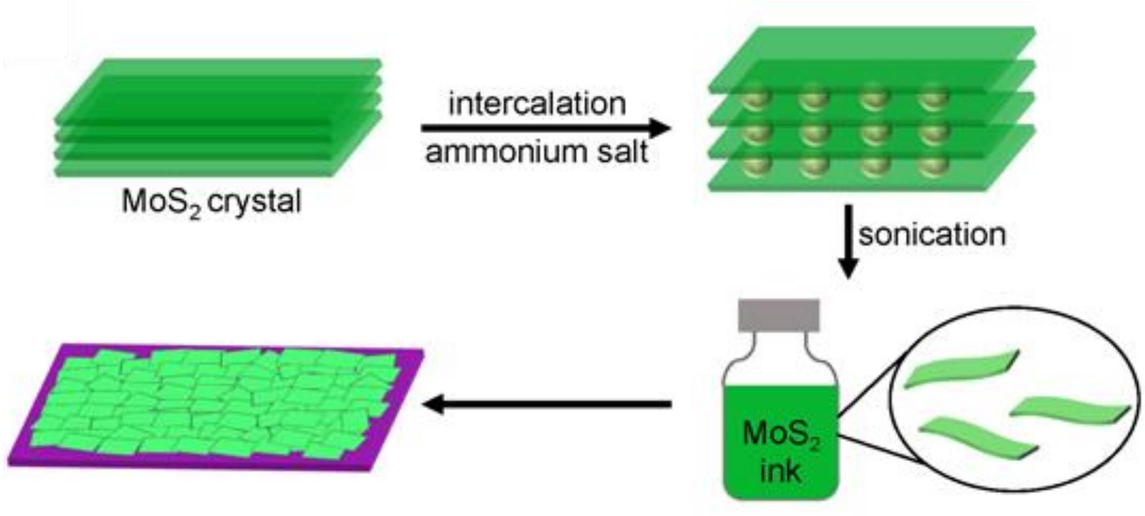

Figure 3.3 The entire process of intercalation, exfoliation through sonication, ink formulation, and finally film deposition.

Characterization. Characterization was carried out using multiple different instruments. For electron microscopy imaging scanning electron microscope (JEOL JSM-6700F FE-SEM) with EDS (EDAX), transmission electron microscope (T12 Quick CryoEM using acceleration voltage, 120 KV) and high-resolution transmission electron microscope (Titan S/TEM FEI: acceleration voltage, 300 KV). X-ray diffraction (XRD, Panalytical X'Pert Pro X-ray Powder Diffractometer) was used to confirm crystal lattice of the MoS_2. UV–vis–NIR absorption spectroscopy (Shimadzu 3100 PC) was performed on the ink solution to normalize concentration. Atomic force microscopy (AFM, Bruker Dimension Icon Scanning Probe Microscope) in tapping mode was used to measure the thickness of MoS_2 flakes. X-ray photoelectron spectroscopy (XPS, AXIS Ultra DLD) measured the oxidation state of the molybdenum atoms. For Raman and photoluminescence, a 488-nm wavelength laser was used as excitation light from Horiba. Electrochemical measurements were done using an electrochemical analyzer/workstation (CHI 600E).

3.3 Results and discussion

The large size of the tetraheptylammonium ion requires a significant amount of applied energy to insert its self into the MoS_2 layered bulk material. To perform the intercalation, process an electrochemical cell was used to apply a voltage to drive the process forward (Figure. 4). The MoS_2 was attached to a copper wire by copper tape and placed on the negative cathode side of the electrochemical cell. A graphite rod was attached to the positive anode side to act as a counter electrode. This was purely a two-electrode system so no reference was used. The electrolyte used in the cell was acetonitrile and tetraheptylammonium bromide salt. Acetonitrile was used because it is an aprotic polar solvent. Aprotic gives no hydrogen evolution side reaction and the polarity of the solvent allowed for rapid solvation of the electrolyte salt. Other aprotic polar solvents such as dimethylformamide (DMF) and n-methyl-2-pyrrolidone (NMP) also worked but acetonitrile was ultimately chosen due to its low boiling point making it easier to wash off. A clear solution was formed with a little mixing indicating the THAB was fully dissolved into the solution in homogenous concentration.

Tetraalkylammonium salts were used due to their wide electrochemical window ensuring stability when a voltage is applied.[27] Tetraheptylammonium molecule consists of a nitrogen with 4 alkyl carbon chains with 7 carbons in length. Heptyl was chosen since it was the largest size molecule that could be efficiently inserted. The intercalation of a large organic molecule increases the van der Waal gap weakening the interlayer interaction. Shorter carbon chains such as tetrabutylammonium, tetrapropylammonium, tetraethylammonium, and tetramethylammonium could be intercalated but showed poor exfoliation. Larger chains such as tetradecylammoniums broke down the MoS_2 crystal instead of efficiently intercalating into the layers.

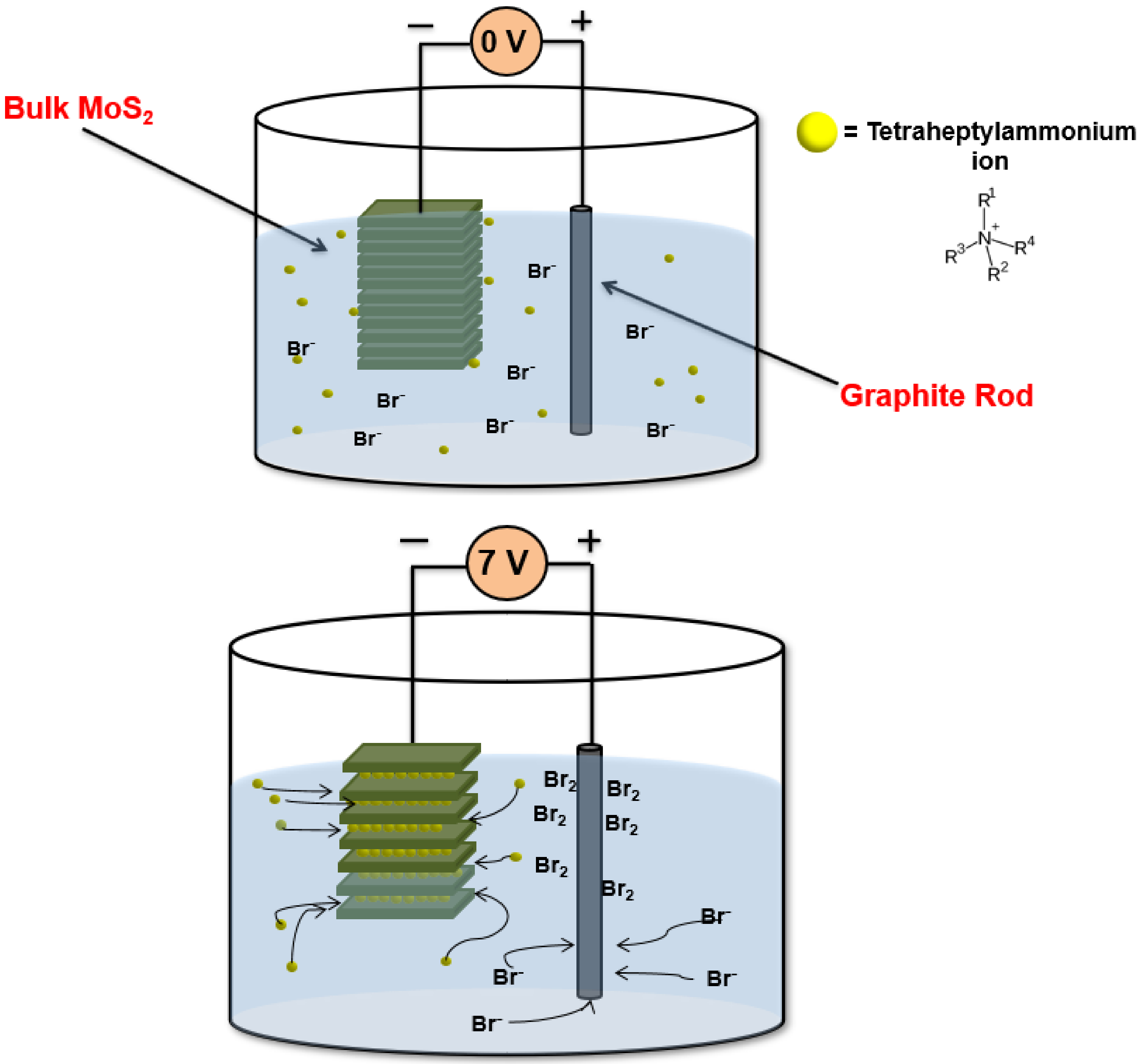

Figure 3.4 Electrochemical two-electrode cell set up for the intercalation process. Before any voltage is applied, molybdenum disulfide cathode and graphite rod counter were placed into the electrolyte solution. The electrolyte was a homogenous mix of tetraheptylammonium ions and bromide ions in acetonitrile. When a voltage was applied, typically 7 volts was used, the tetraheptylammonium ions with positive charge were intercalated into MoS_2 with the applied negative charge. The bromine ions were oxidized at the graphite rod.

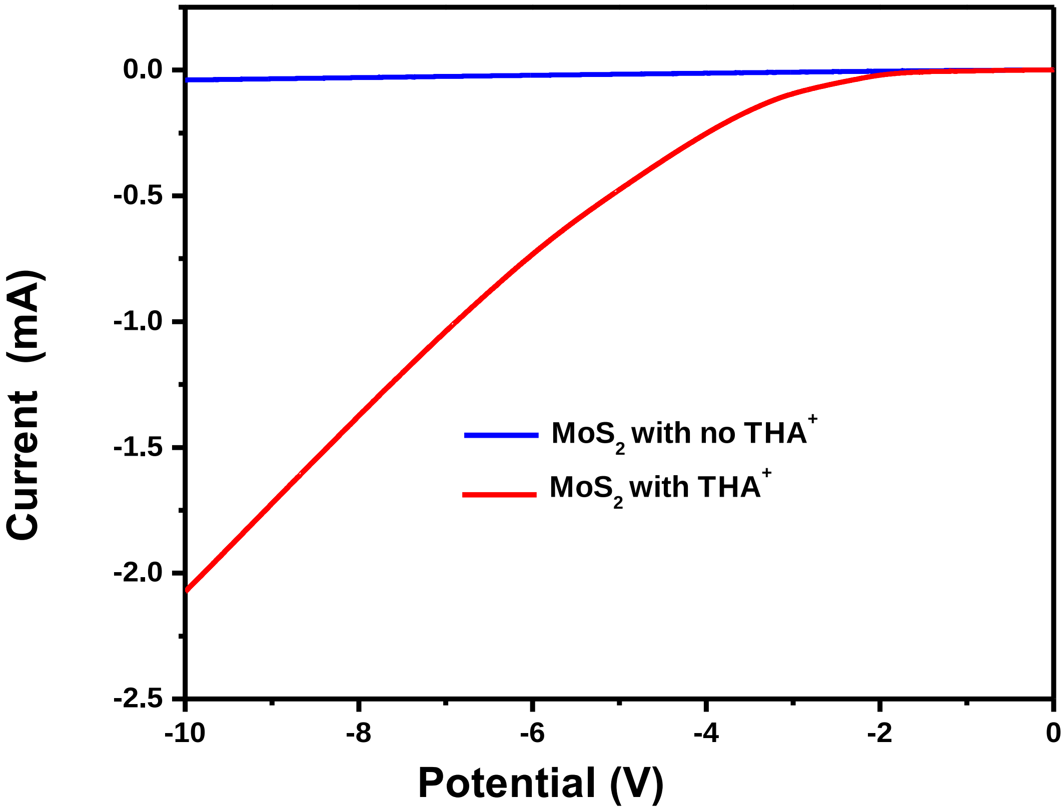

Figure 3.5 Electrochemical two-electrode potentiometry data. This electrochemical data shows there is no side reaction with MoS_2 and acetonitrile. When a voltage is applied with no added THAB, there is no current. With the addition of THAB a current is seen starting at roughly 3 V indicating the intercalation process.

Using electrochemical analyzer (CHI), it was shown that MoS_2 had no reaction with the solvent acetonitrile (Fig. 5). Even when a large voltage of 10 V was applied, there was little current, the small amount of current is likely due to the breakdown of the solvent. No expansion was seen on the MoS_2 crystal. When the THAB salt was added to form an electrolyte, starting from roughly 3 V is when a current occurred. This current is due to the intercalation process of THAB into the layers of MoS_2. As the voltage increased the current increase indicating a faster intercalation time. A voltage of 7 was ultimately chosen since it was a good balance of fast intercalation without stripping the bulk of MoS_2 from the copper wire. During the intercalation process it was important to make sure only the MoS_2 crystal was inserted into the electrolyte solution otherwise the copper would rust.

An indicator the intercalation process was working is the yellow color that forms at the graphite rod. This yellow color was due to bromine ions being oxidized. Another more noticeable indication was the MoS_2 crystal expanding in size as tetraheptylammonium ions inserted into the layers. Similar to lithium intercalation there is an electron injected into the molybdenum atom followed by the intercalation of a positively charged ion. This reaction can be seen in formula (1) below. Each electron injected combined with tetraheptylammonium forms an intercalation compound with a single formula unit of MoS_2. This all occurs on the cathode side of the two-electrode electrochemical cell. On the anode side with the graphite rod, bromine ions are oxidized to Br_2 shown in formula (2).

$$\mathrm{MoS_2} + x\mathrm{THA}^+ + xe^- \rightarrow (\mathrm{THA}^+)_x\mathrm{MoS}_2^{x-} \tag{1}$$

$$x\mathrm{Br}^- \rightarrow (x/2)\mathrm{Br_2} + xe^- \tag{2}$$

The starting piece of MoS_2 was a bulk crystal of naturally occurring from a mined source and not lab grown (Fig. 5a). Using this bulk crystal, due to the layered structure, it could be easily cleaved into thin flat pieces controlled to be 0.3 mm in thickness (Fig. 5b). A thin flat piece ensured the most efficient and most complete intercalation. It was found with larger pieces the outer layer would be intercalated but the inner core was not able to come in contact with THAB. After the 1-hour intercalation process the MoS_2 expanded like a popcorn. The post intercalation thickness was 12.4 mm from 0.3 mm, this was a size increase of 41 times (Fig. 5c).

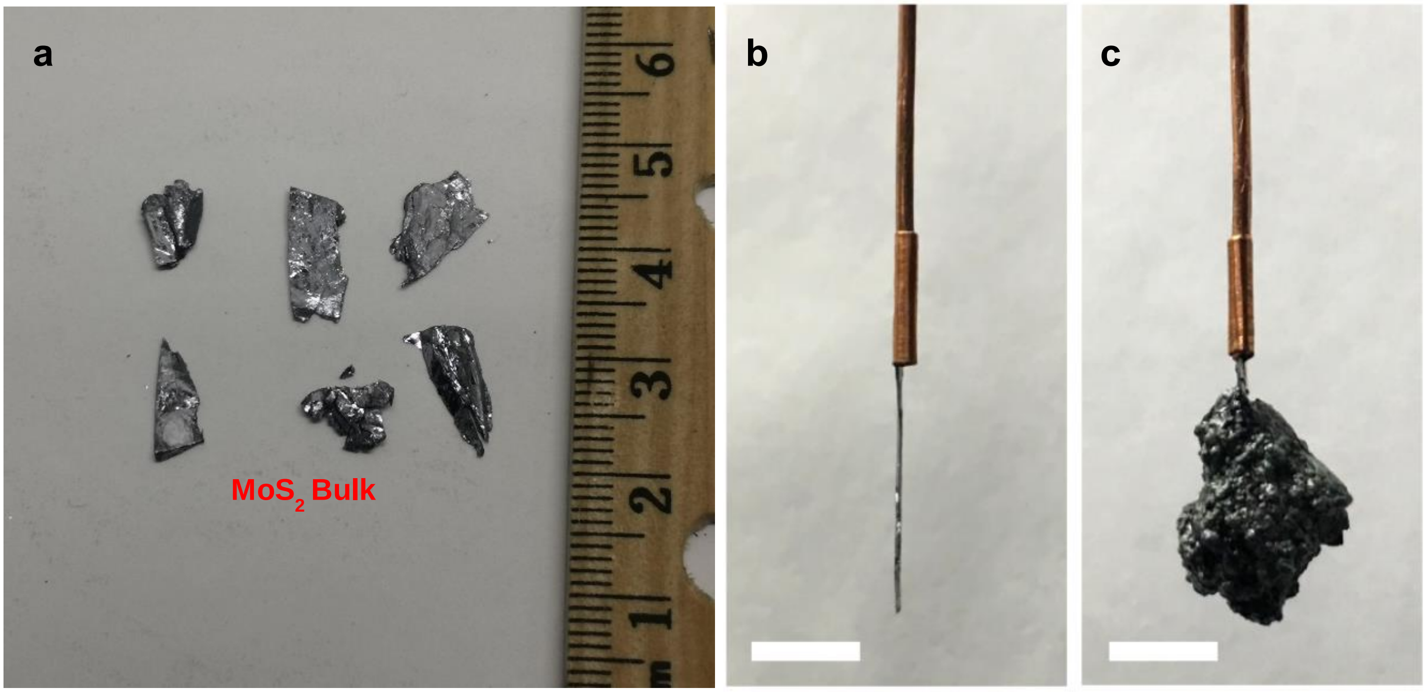

Figure 3.6 Pictures of MoS_2 in bulk form, pre-intercalated, and post intercalation. (a) bulk pieces of MoS_2 were sizes upwards of an inch, some being even larger. (b) Cleaved piece of thin flat MoS_2 with average thickness of 0.3 mm. Here the scale bar is 1 cm. The length is still 1 inch in length since the crystals were cleaved along the face of the crystals. (c) After intercalation the new MoS_2 became a fluffy popcorn like structure. This expansion of size is one of the first pieces of evidence the intercalation process was successful. The new length was 12.4 mm, an increase of 41 times. Scale bar is 1 cm.

The intercalated expanded MoS_2 was then placed in DMF with 0.8 mmol of PVP. The PVP acted as a stabilizing agent for the nanosheets to prevent any aggregation. Without any PVP added, rapid aggregation was observed. DMF was chosen since it has been shown to act as a great exfoliation solvent for layered crystals.[28] 40 mL of DMF was placed into a 250 mL beaker along with the PVP and MoS_2. The intercalation of a large organic molecule greatly weakened the van der Waals interaction. When a piece of intercalated MoS_2 was exfoliated in DMF solution, a homogenous dark greenish solution formed. This color was a result of colloidal MoS_2 nanosheets in the solution. When compared to a piece of MoS_2 with no intercalation, the intercalated piece showed 1000 times greater exfoliation (Fig. 7). In both cases a 0.3mm thickness piece of MoS_2 normalized to a weight of 250 mg. The non-intercalated MoS_2 sonicated with bath sonication only showed 0.01 mg per mL, while the intercalated solution had a concentration of 10 mg per mL.

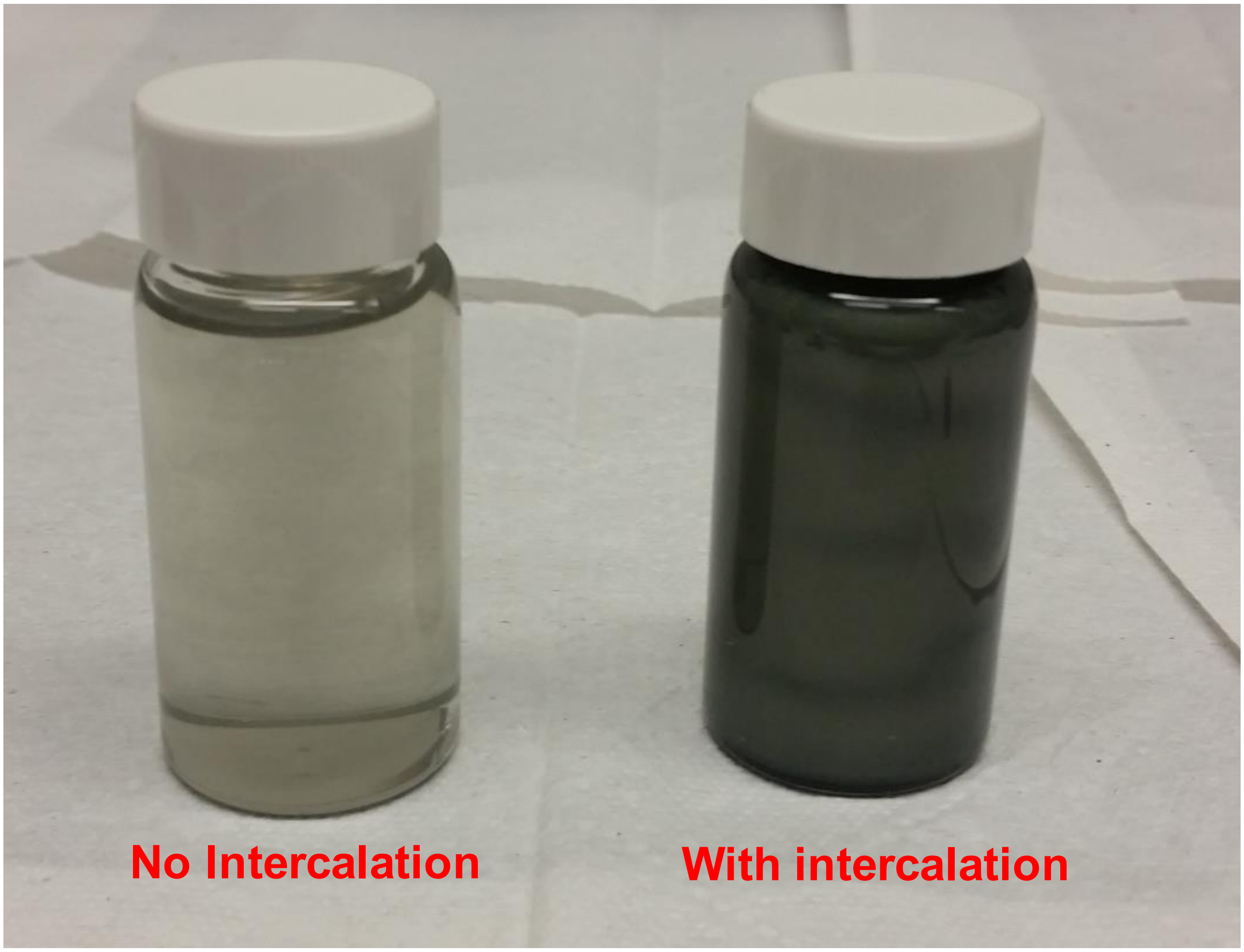

Figure 3.7 Comparison of exfoliation efficiency between pure flake of MoS_2 and intercalated MoS_2. The solution on the left was a piece of MoS_2 placed into DMF/PVP solution. It was sonicated for a total of one hour. The light green color showed there was slight exfoliation. The solution on the right was a piece of MoS_2 first being intercalated with tetraheptylammonium. It expanded into a popcorn structure before being placed into a DMF/PVP solution. Both solutions were sonicated for a total of 1 hour in the same bath sonicator. The concentration of the non-intercalated piece showed 0.01 mg/mL whereas the intercalated MoS_2 had a concentration of 10 mg/mL. Both MoS_2 pieces used were 0.3mm in thickness and weighed approximately 250 mg.

To prove intercalation happened X-ray diffraction was performed on the intercalated MoS_2 (Fig. 8). Pure bulk MoS_2 has a (002) peak and a (004) peak matching with the d-spacing of the van der Waal gap. After intercalation with tetraheptylammonium ions, there were a series of new peaks that arose due to the increase in gap size. The original (002) and (004) peaks still remained showing that not every single layer was intercalated. The new peaks (002*) was calculated to be 22 Å. This matches with the size of tetraheptylammonium which has a molecular diameter of 20 Å, the extra gap spacing is likely due to DMF solvent intercalating along with the THA^+.

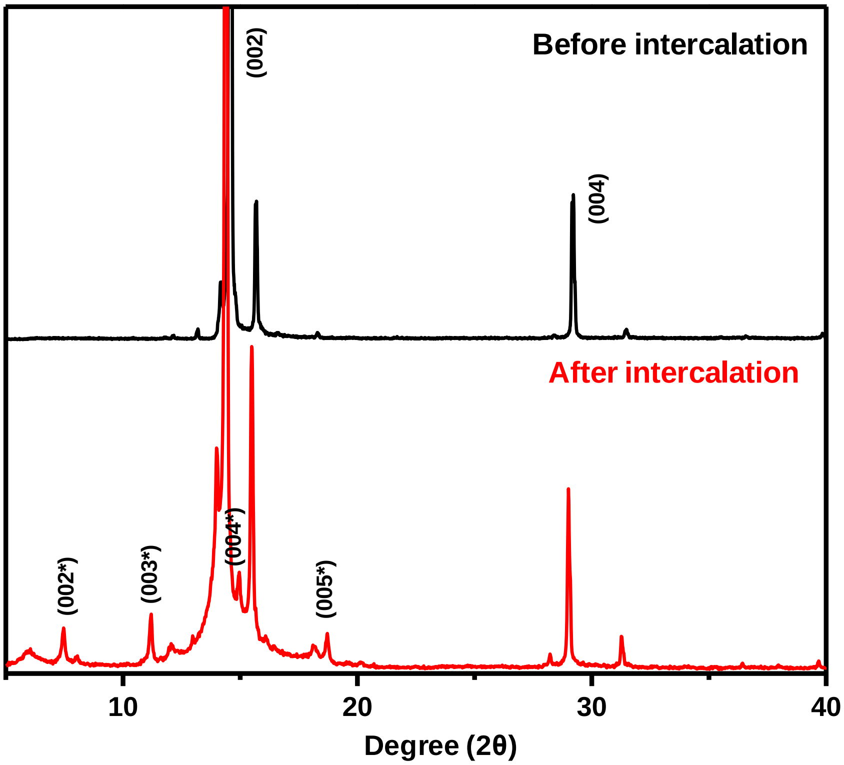

Figure 3.8 X-ray diffraction data of pure MoS_2 flake before and after intercalation. The MoS_2 was scanned along the (002) plane, along the cleaved face. Before intercalation the main peaks were (002) and (004). After intercalation these original peaks still existed, but several new peaks appeared. A new (002*) peak occurred at about 6 degrees which was calculated to be 22 Å. This diffraction data is proof that intercalation did occur and the new gap size matches the size of the molecule intercalated.

After intercalation and exfoliation, the MoS_2 nanosheets were washed with isopropanol. The colloidal nanosheet solution could be dispersed in multiple different solvents such as isopropanol, ethanol and DMF depending on the need. For film deposition, isopropanol was used. The colloid was found to be stable for several weeks showing little aggregation which could be redispersed with sonication. Atomic force microscopy (AFM) was used to measure the thickness of the nanosheets (Fig. 9). The latteral size ranged from 200 nm to 1 μm. This sample was made by spin coating a dilute sample of MoS_2 in isopropanol onto silica wafer.

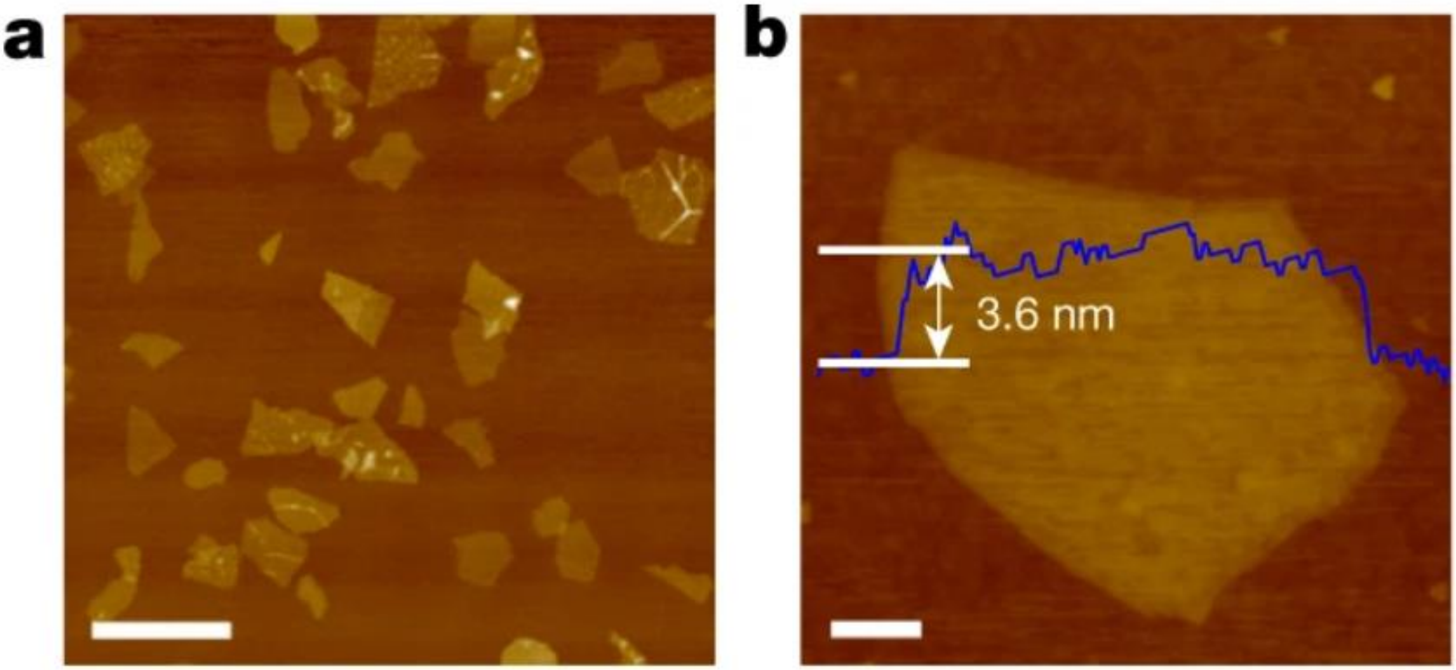

Figure 3.9 Atomic force microscopy data. (a) A view of general population of nanosheets. The lateral sizes ranged with sizes up to 1 μm. The thickness of the sample was fairly uniform with thickness ranging from 2 nm to 8 nm. The average thickness was 4 nm. Scale bar here is 2 μm. (b) A thickness measurement of a single flake shows a thickness of 3.6 nm. All of the sheets had a thickness well under 100 nm making them true 2D nanostructure materials. Scale bar here is 200 nm.

The average thickness of the nanosheets was 4 nm. Multiple flake thickness was measured showing a narrow distribution of thickness (Fig. 10). The total range showed that some nanosheet thickness were as thin as 2 nm to some thicker at 8 nm. The majority were 3-5 nanometers, this narrow size distribution will later equate to uniformity in film deposition.

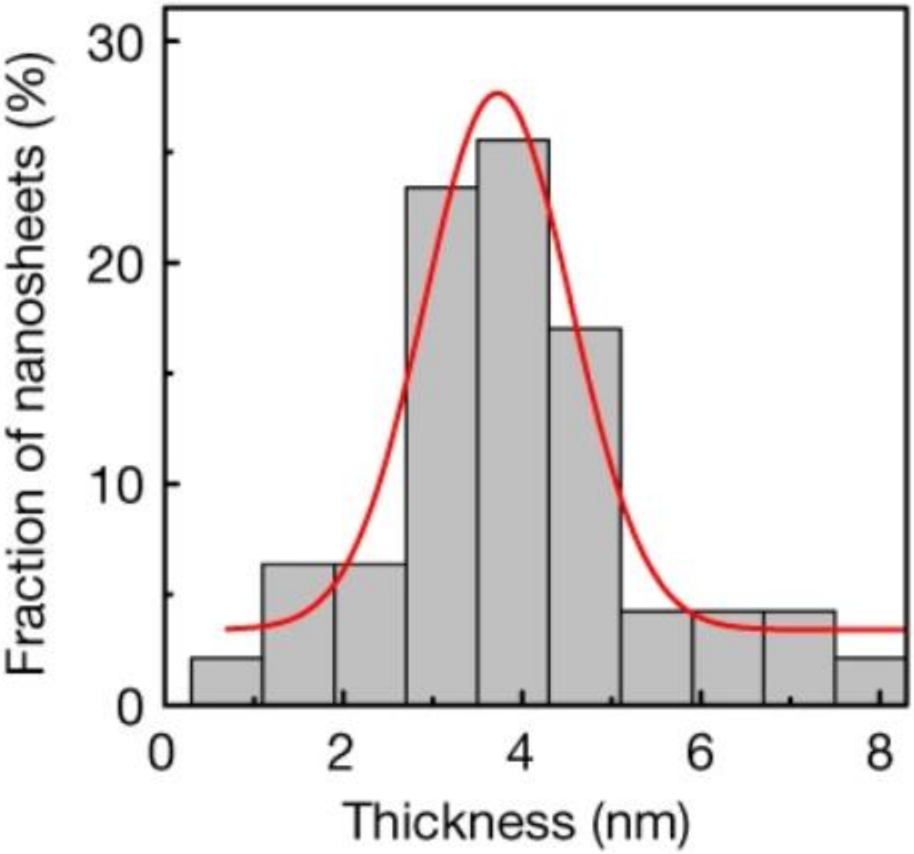

Figure 3.10 Thickness distribution of the exfoliated nanosheets. The majority ranged from 3-5 nanometers in thickness.

Using Raman spectroscopy, the $E^1{}_2g$ and A_1g peaks were found at 383.6 cm$^-$1 and 408.3 cm$^-$1 respectively (Fig. 11). This down shift in the A_1g when compared to bulk MoS_2 is consistent with few layer MoS_2 further confirming nanosheets were produced.[29] The ratio of intensity of A_1g and E_2g was 0.9 demonstrates little sulfur vacancy defects in the resulting nanosheets.[30] This Raman data further displays the few layered nanosheets high quality.

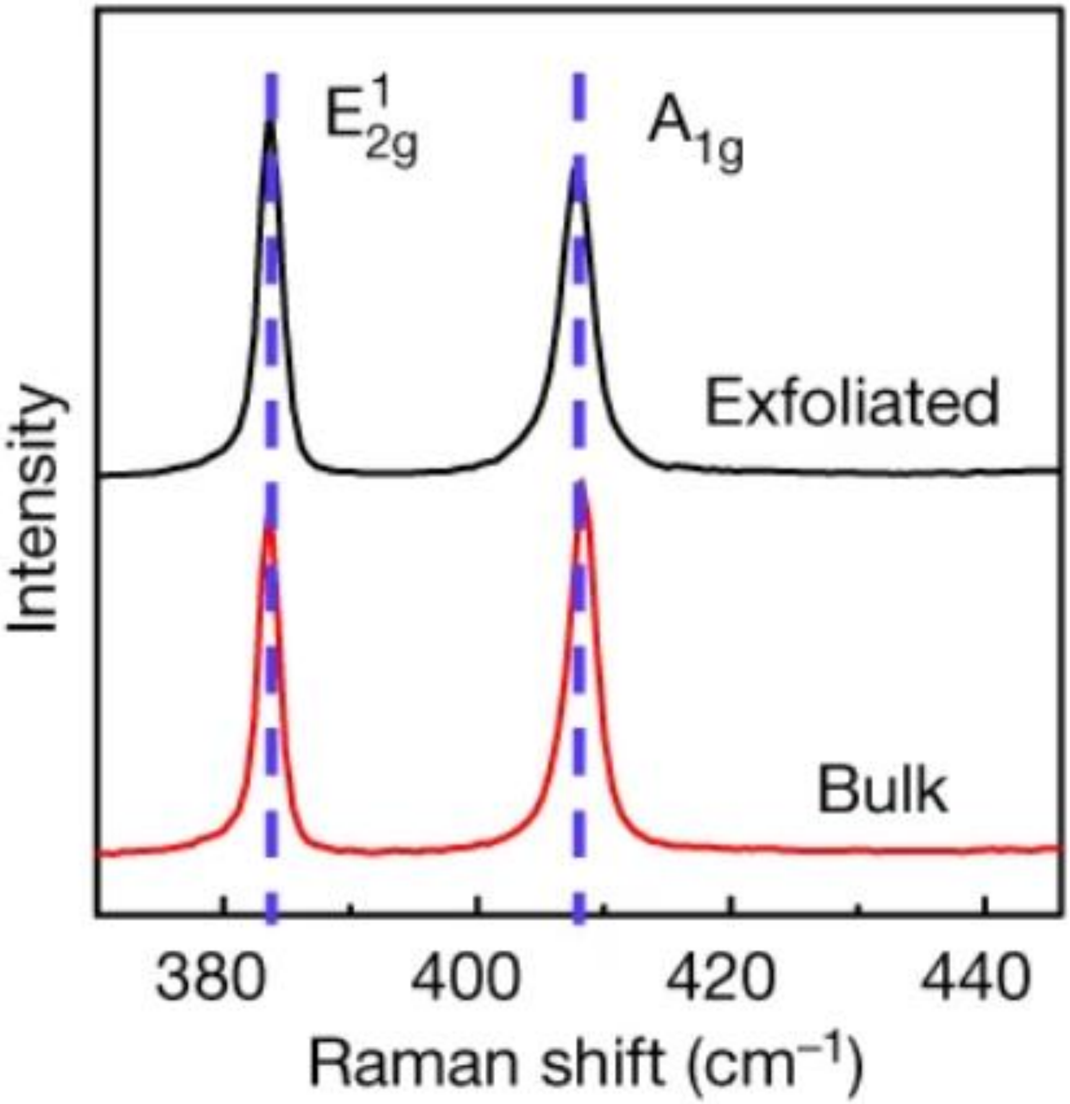

Figure 3.11 Raman spectroscopy analysis using a 488 nm laser. The top black line is from an intercalated exfoliated piece of MoS_2. The bottom red shows a bulk MoS_2.

Using a scanning electron microscope Energy-dispersive X-ray spectroscopy (EDS) was performed on a large sized single flake (Fig. 12). The calculated ratio of molybdenum and sulfur was 1:2. This further confirms the crystal did not break down or generate a significant amounts of sulfur vacancy. Even after intercalation of a foreign molecule and exfoliation, the nanosheets still remained MoS_2.

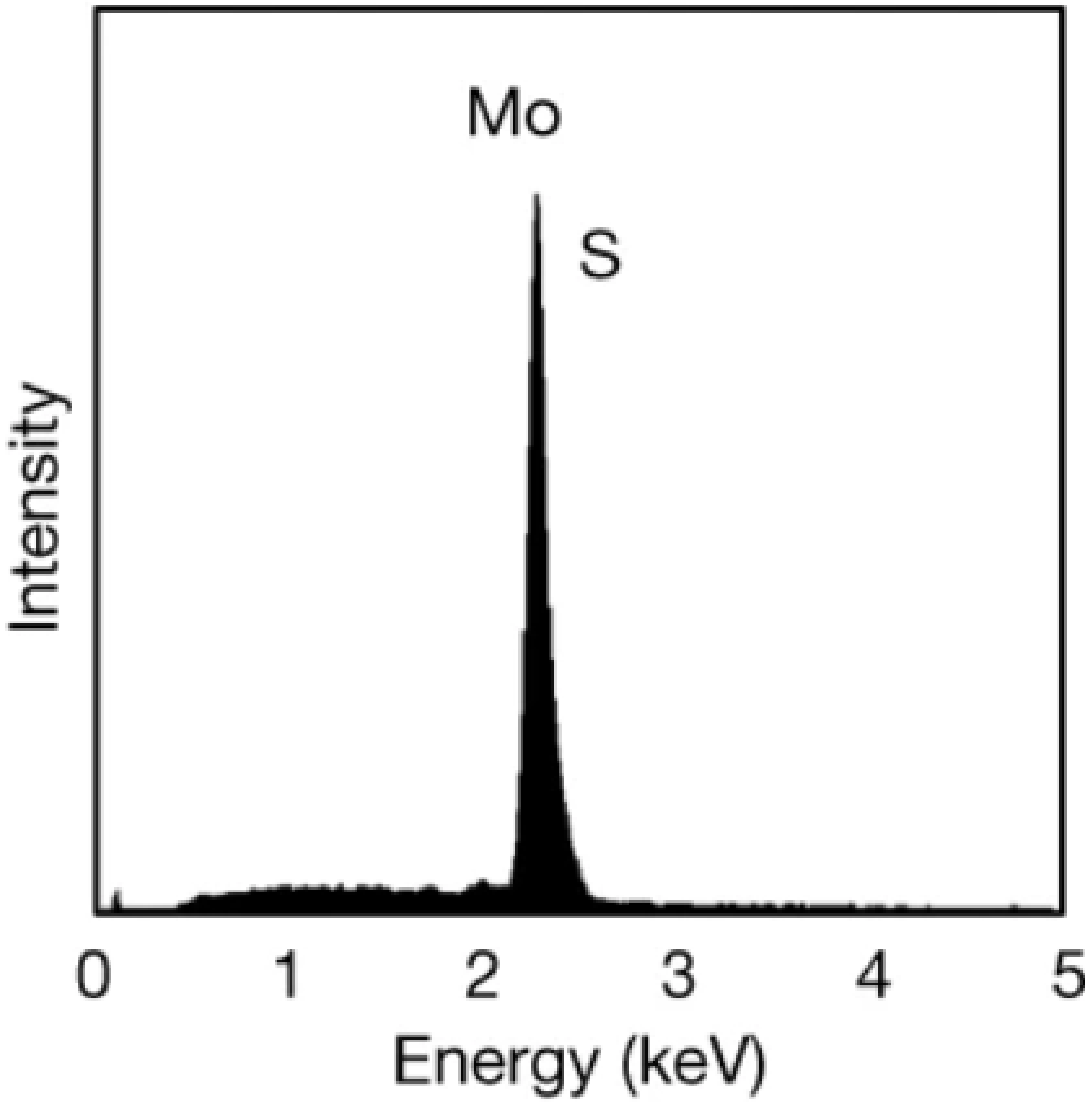

Figure 3.12 Energy-dispersive X-ray spectroscopy (EDS) showed the ratio of molybdenum to sulfur was 1:2. This is consistent with the formula unit of MoS_2.

Transmission electron microscope was used to analyze the crystallinity and quality of the nanosheets (Fig 13). The transmission electron microscope (TEM) image presented a low contrast between the nanosheet and the background indicating thin nature of the nanosheets. From TEM it can also be seen that the thickness was uniform with no fracturing in the nanosheet.

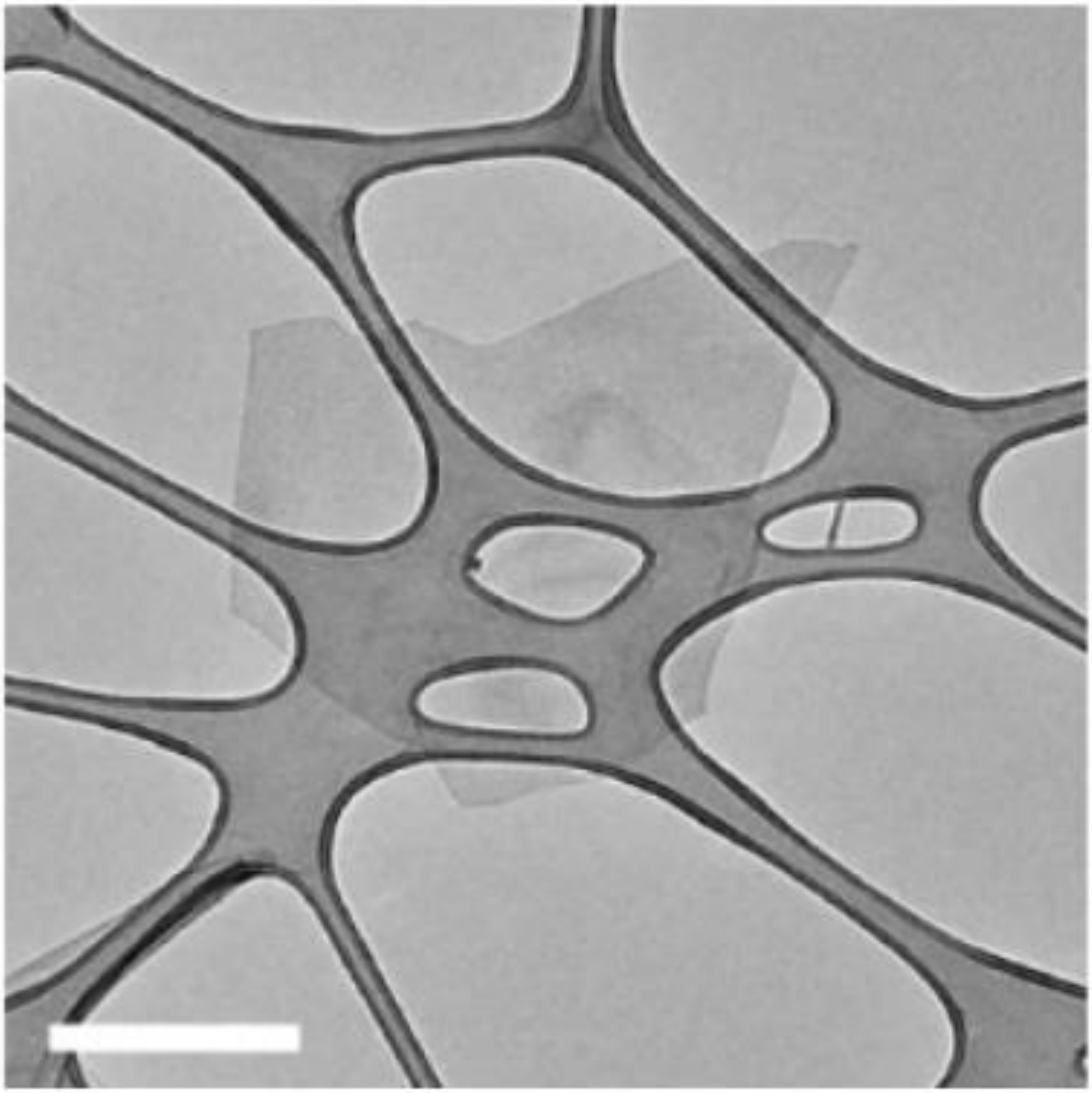

Figure 3.13 Typical transmission electron microscope image of MoS_2 nanosheet that is produced through intercalation exfoliation. Scale bar is 500 nm.

On the same flake electron diffraction was performed to further confirm crystallinity (Fig. 14). The diffraction showed a hexagonal pattern. The single spot diffraction pattern represents high crystallinity and no polycrystallinity. The hexagonal spot diffraction was indexed to MoS_2 (100) plane.

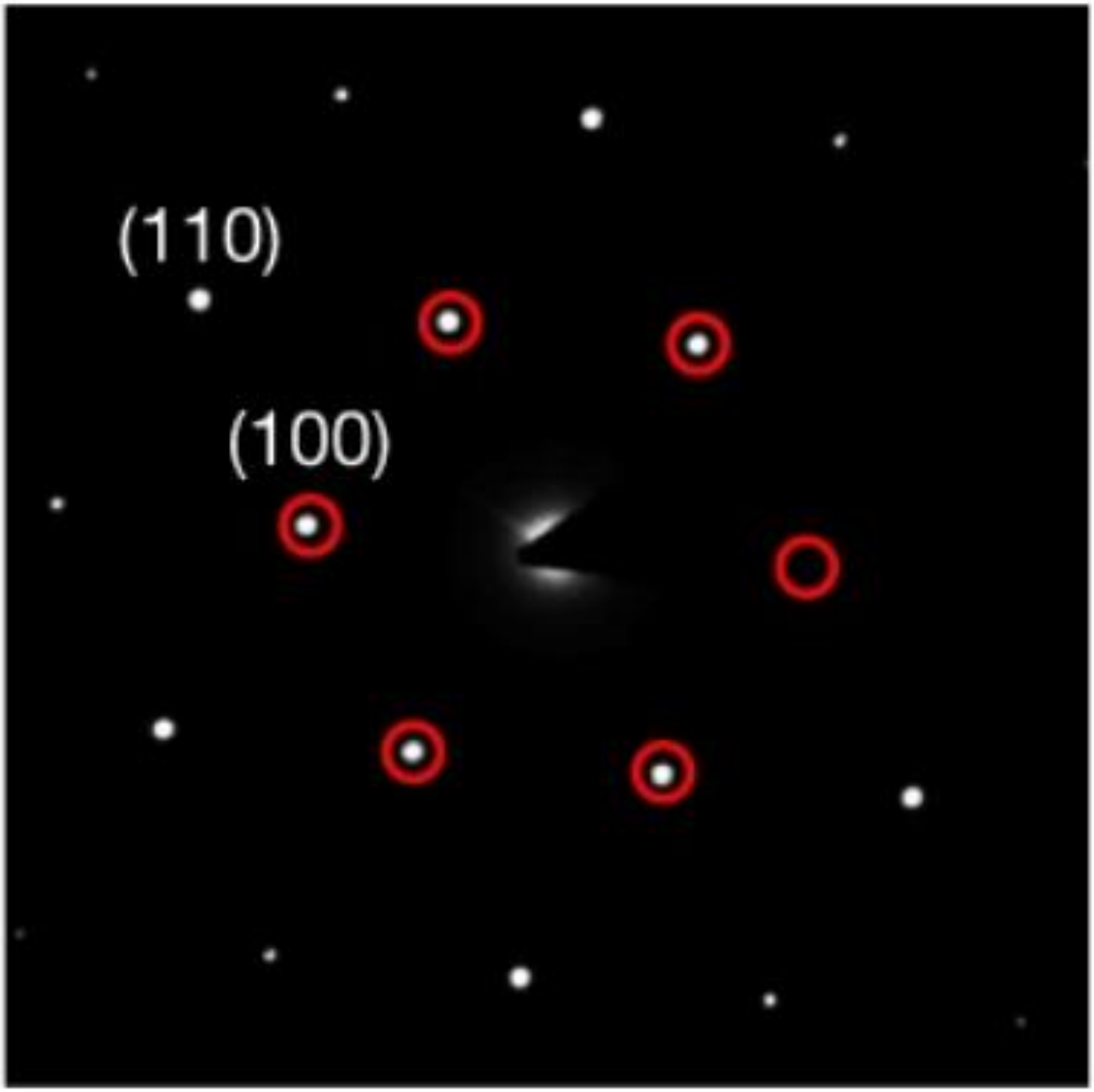

Figure 3.14 Electron diffraction pattern of exfoliated MoS_2 nanosheet. The diffraction pattern was indexed to (100) plane and showed hexagonal crystal structure.

High resolution transmission electron microscope (HR-TEM) was also performed to further confirms the high crystallinity within the individual nanosheets (Fig. 15). The HR-TEM along the (100) plane had a lattice spacing of 0.28 nm, consistent with pristine MoS_2. The orderly lattice array of atoms demonstrates the highly ordered crystallinity of the exfoliated nanosheet.

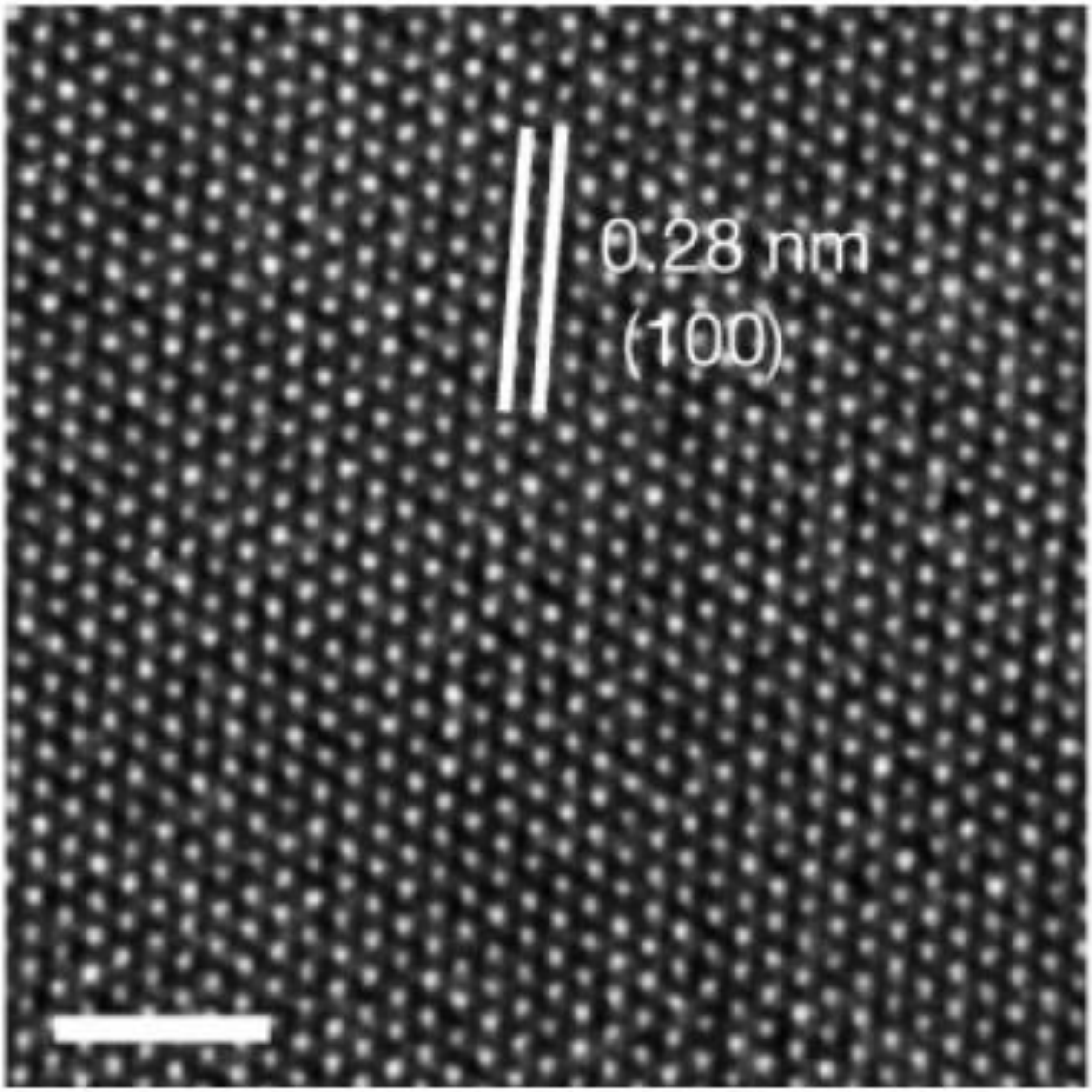

Figure 3.15 High-resolution transmission electron microscope image of an exfoliated nanosheet. Scale bar is 2 nm.

Besides simply largely expanding the van der Waal interaction to the point where only gentle bath sonication is required to completely exfoliate the bulk down to nanosheets. A unique property of using a large organic molecule such as tetraheptylammonium is the reduction in electrons being injected into the MoS_2. Typically, when a foreign molecule or atom is intercalated, it is followed by an electron injected into the d-orbital of the molybdenum. For many transition metal dichalcogenides such as MoS_2 and $MoSe_2$, there is a crystal phase shift when a large number of electrons is injected. This crystal shift turns the crystals from a 2H phase to a 1T. There are many property differences between 2H and 1T. 2H is semiconducting while 1T is metallic. A unique property of using large tetraheptylammonium molecules is the packing density is 100 times greater than lithium ions, reducing the amount of electron injections by 100 times (Fig. 16). Nanosheets produced with lithium intercalation shows large amounts in 1T phase, whereas using THA^+ retains its intrinsic 2H phase.

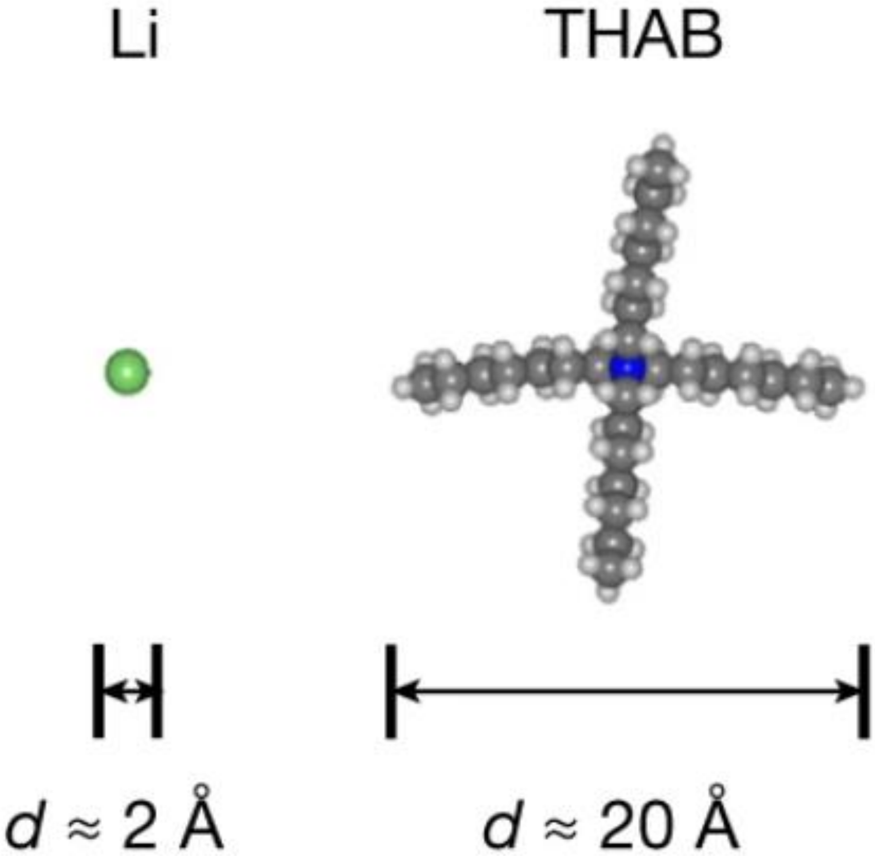

Figure 3.16 The size difference of lithium versus tetraheptylammonium. A single lithium atom is 2 Å, tetraheptylammonium is 20 Å. With a diameter difference of 10 times, the packing density of lithium is 100 times smaller than tetraheptylammonium.

The pure phase 2H MoS_2 solution is dark green in color. This is due to the partial absorption of visible light. 1T MoS_2 solution is metallic with no bandgap, showing a black solution. This is seen in ultraviolet-visible absorption spectroscopy (Fig. 17). Here 2H has noticeable absorption peaks and 1T has no strong absorption in the visible range. This absorption spectroscopy data is one piece of evidence of pure phase 2H retention when intercalated with THA^+.

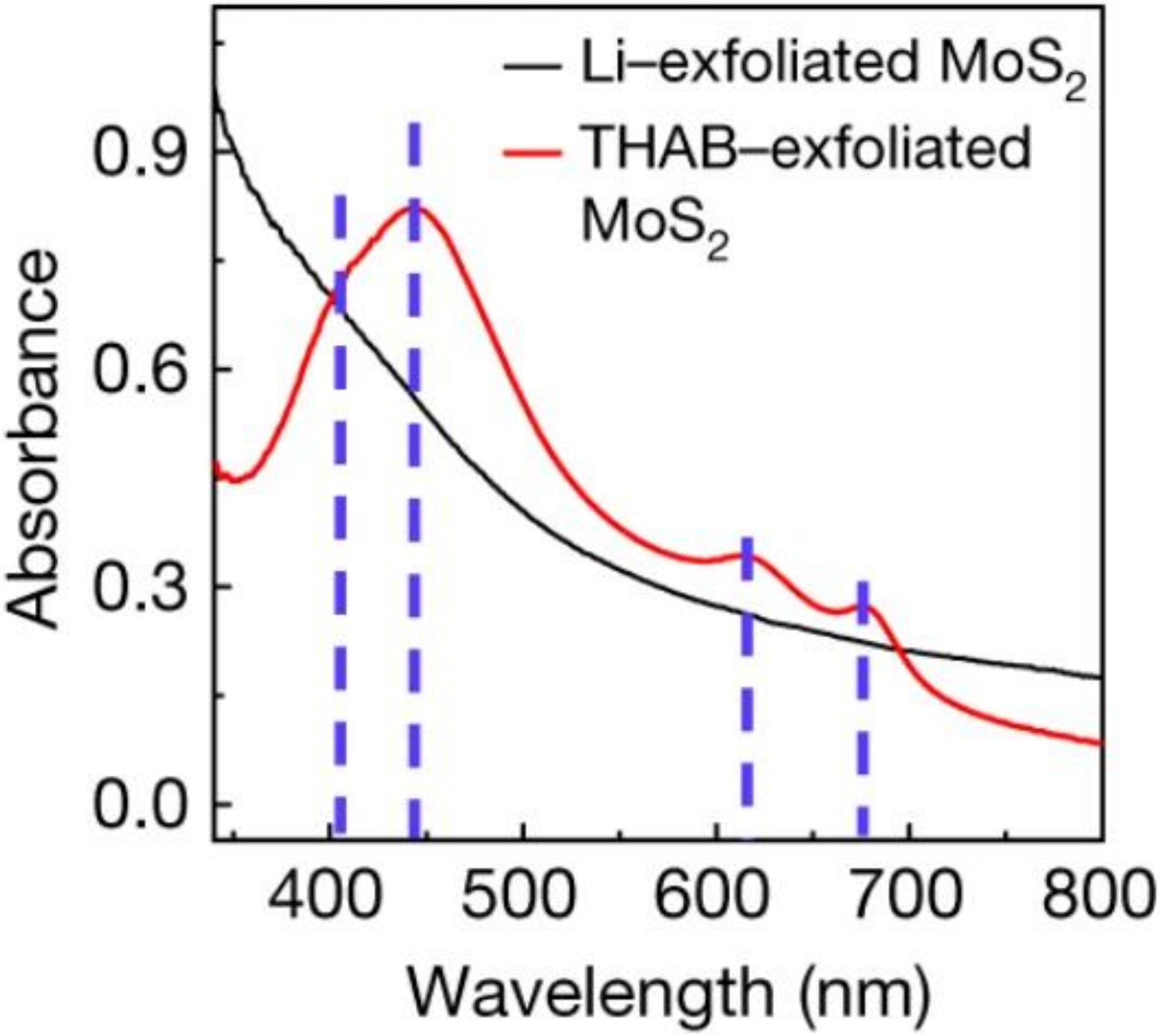

Figure 3.17 Using THAB to intercalate MoS_2 shows noticeable peaks in Uv-vis spectroscopy. Using lithium intercalated MoS_2 shows significant 1T phase shift. The 1T phase of MoS_2 shows no noticeable absorption peaks in the visible range.

X-ray photoelectron spectroscopy (XPS) was also performed to better understand the oxidation state of the molybdenum atom (Fig.18). Characteristically, as electrons are injected into molybdenum, the binding energy decreases since the positive charge of the molybdenum interacting with the shell electrons weakens. What can be seen from XPS data is the nanosheets from tetraheptylammonium intercalated resulted in no shift in binding energy. With the lithium intercalated XPS there is a mix phase of both 2H and 1T. THA^+ shows pure phase 2H MoS_2.

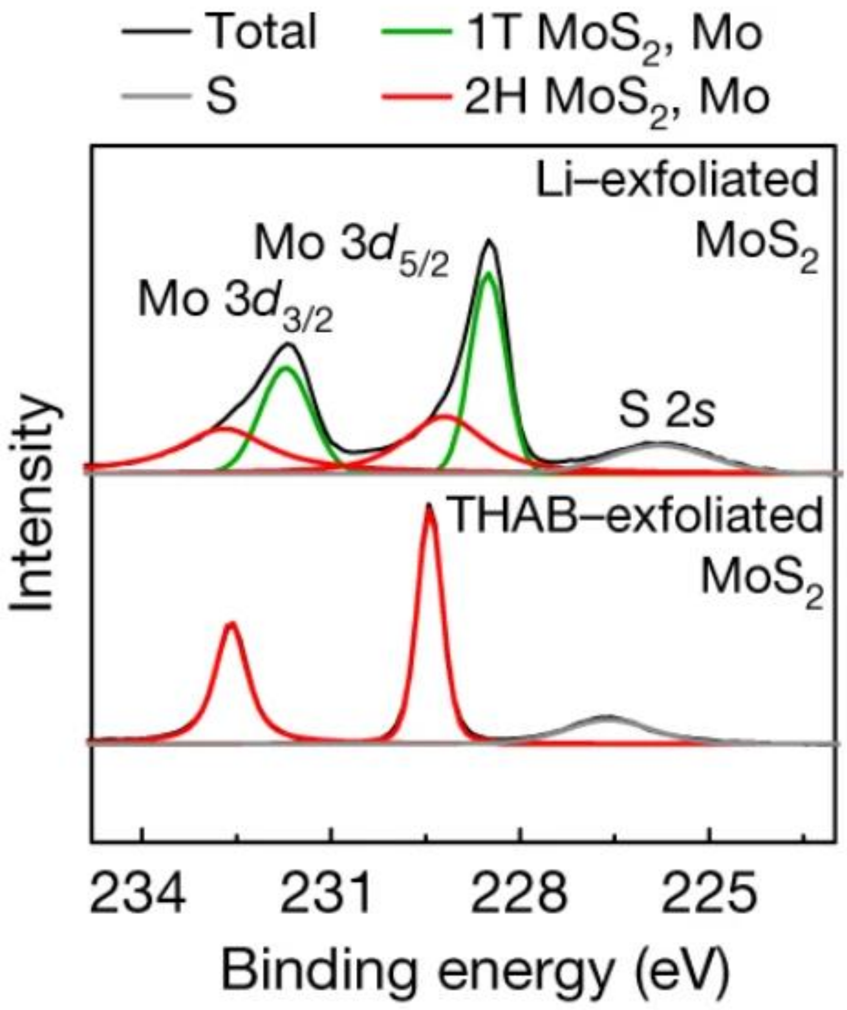

Figure 3.18 XPS data of both lithium intercalated and exfoliated MoS_2 shown on top. On the bottom is tetraheptylammonium intercalated and exfoliated MoS_2. The THA^+ intercalated MoS_2 shows pure 2H phase with no presence of 1T.

The pure 2H phase MoS_2 from tetraheptylammonium intercalated and exfoliated had a strong photoluminescence response (Fig. 19). Compared to 1T MoS_2 produced from lithium intercalation presented a lack of photoluminescence due to absence of an energy bandgap.

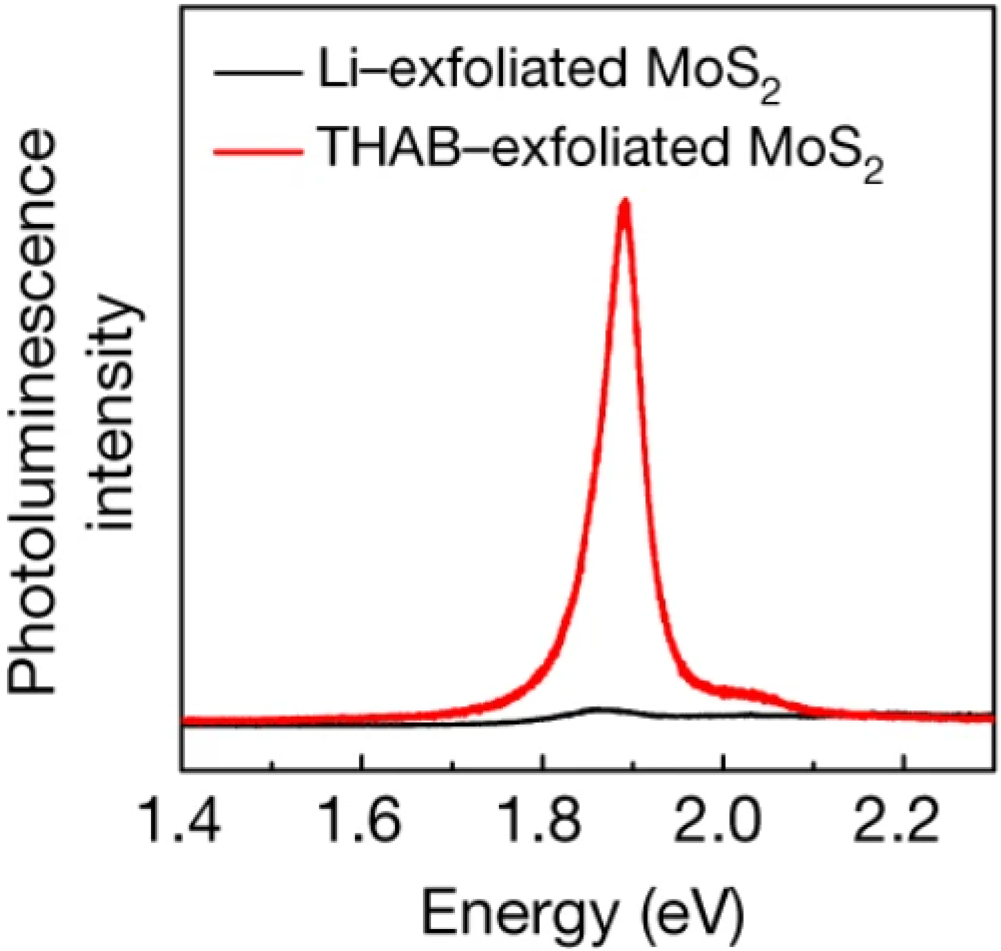

Figure 3.19 Photoluminescence data of both nanosheets produced from lithium intercalation shown in black. The red line is photoluminescence response from nanosheets produced by tetraheptylammonium intercalation.

One final piece of evidence that shows tetraheptylammonium intercalation retains the 2H phase is from gate response when a back-gate transistor is made (Fig. 20). This transistor was made on a single flake of both lithium intercalation and THA^+ intercalation. The electrodes were deposited through e-beam evaporation using electron beam lithography to pattern. Both were devices fabricated on SiO_2/Si using the p-doped Si as a back-gate. The 2H semiconducting MoS_2 behaves like a proper semiconductor with gate tunability. The 1T phase metallic MoS_2 from lithium intercalation shows no gate modulation at all. The mobility of the 2H single flake was 10 $cm^2 \cdot V^{-1} \cdot s^{-1}$.

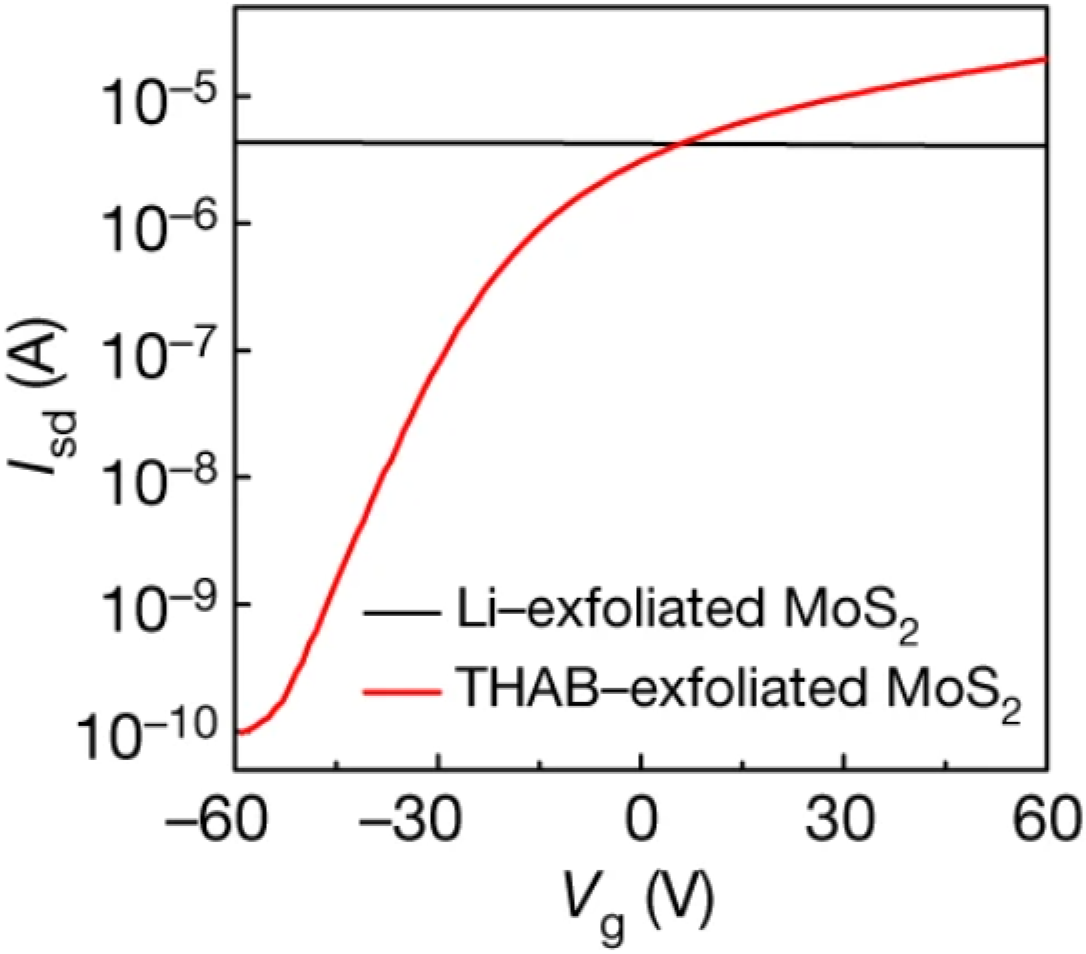

Figure 3.20 Back-gate $I_{sd} - V_g$ transfer characteristic data. The black line is the current response as voltage is applied to a lithium intercalated and exfoliated MoS_2 nanosheet. The red line is from tetraheptylammonium intercalated and exfoliated MoS_2 nanosheet. The 2H semiconducting phase retained by THA^+ intercalation shows gate modulation, typical of semiconductors.

It has been evident that intercalating a large tetraheptylammonium ion in between layered crystals is possible. The large molecule expands the layers and weakens the van der Waals interactions even further which allows for efficient exfoliation using gentle bath sonication. This produces a colloidally stable solution of nanosheets. These nanosheets retain their 2H semiconducting phase due to low number of electrons injected. Also, the nanosheets remain MoS_2 with no defects or destruction in crystallinity. Now knowing that MoS_2 nanosheets can be produced in solution-phase through intercalation and exfoliation of a large organic molecule, the colloid can be concentrated down into a suitable solvent for film deposition. In this case isopropanol was chosen due to the quick evaporation and low toxicity. This ink could be used to print an electronic thin-film over a large area. The whole deposition process was low in temperature and requires no vacuum. To demonstrate, the MoS_2 was spin-coated into a thin-film over an entire 100 mm silica wafer (Fig. 21).

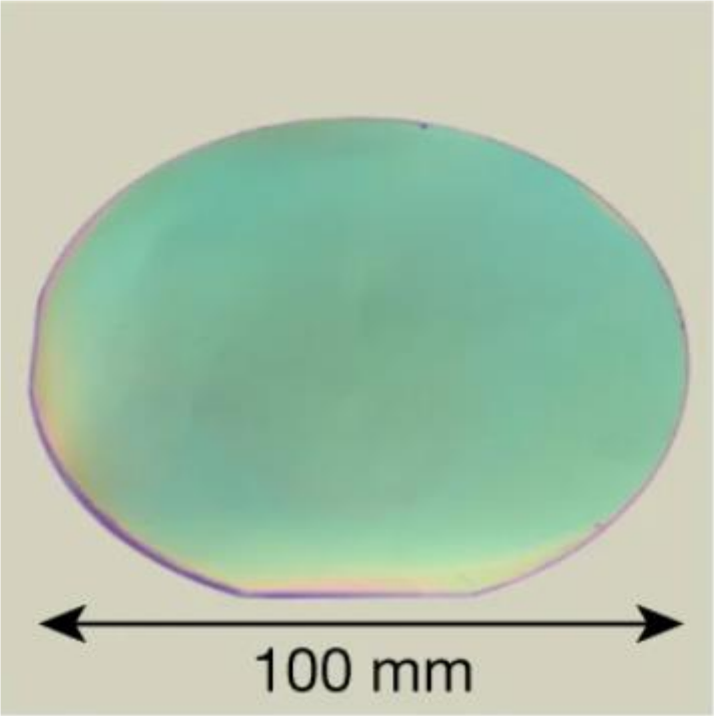

Figure 3.21 A large 100 mm silica wafer. On top of it is a spin-coated thin-film of MoS_2. The entire deposition done through a solution-based method.

The films were further annealed between 200-300 degrees Celsius to burn off any organic residues. This low temperature annealing ensures that plastic substrates such as polyimide could be used. X-ray diffraction was performed on the deposited film to ensure crystallinity of the MoS_2 maintained. The XRD showed pure (001) peak lattice diffractions matching with pristine bulk MoS_2 (Fig. 22). The exfoliation step was successful at breaking the intercalated MoS_2 down into nanosheets, with no THA^+ ions stuck in between the sheets.

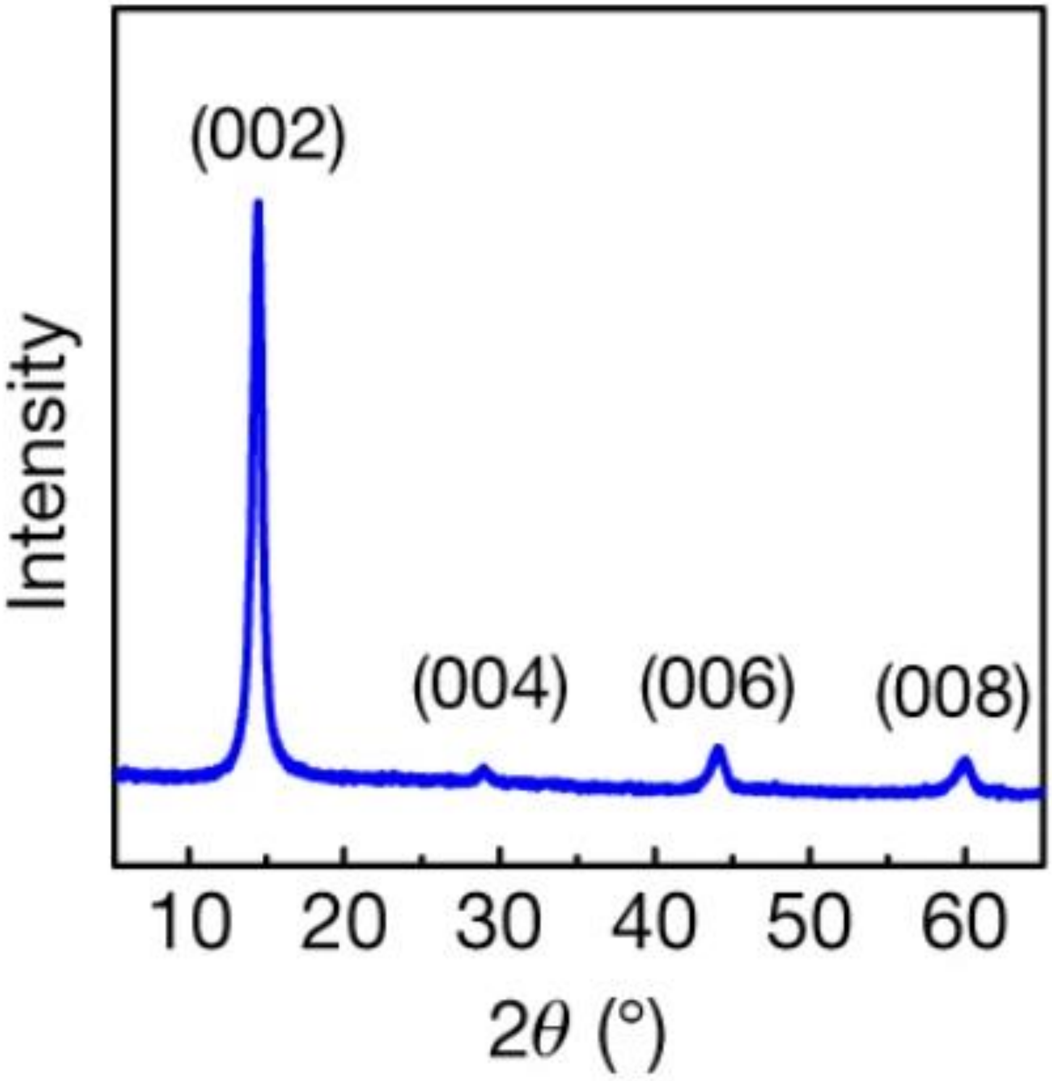

Figure 3.22 X-ray diffraction data of the solution deposited MoS_2 thin-film. This XRD data shows controlled flat assembly along the (001) direction.

Scanning electron microscope (SEM) imaging showed further proof of flat assembly on silica wafer (Fig. 23). From the SEM image we see the face of many different MoS_2 nanosheets.

All lying flat on the silica, none folded or in other strange orientations. The MoS_2 nanosheets form a complete film with facial contact with each other after spin-coating.

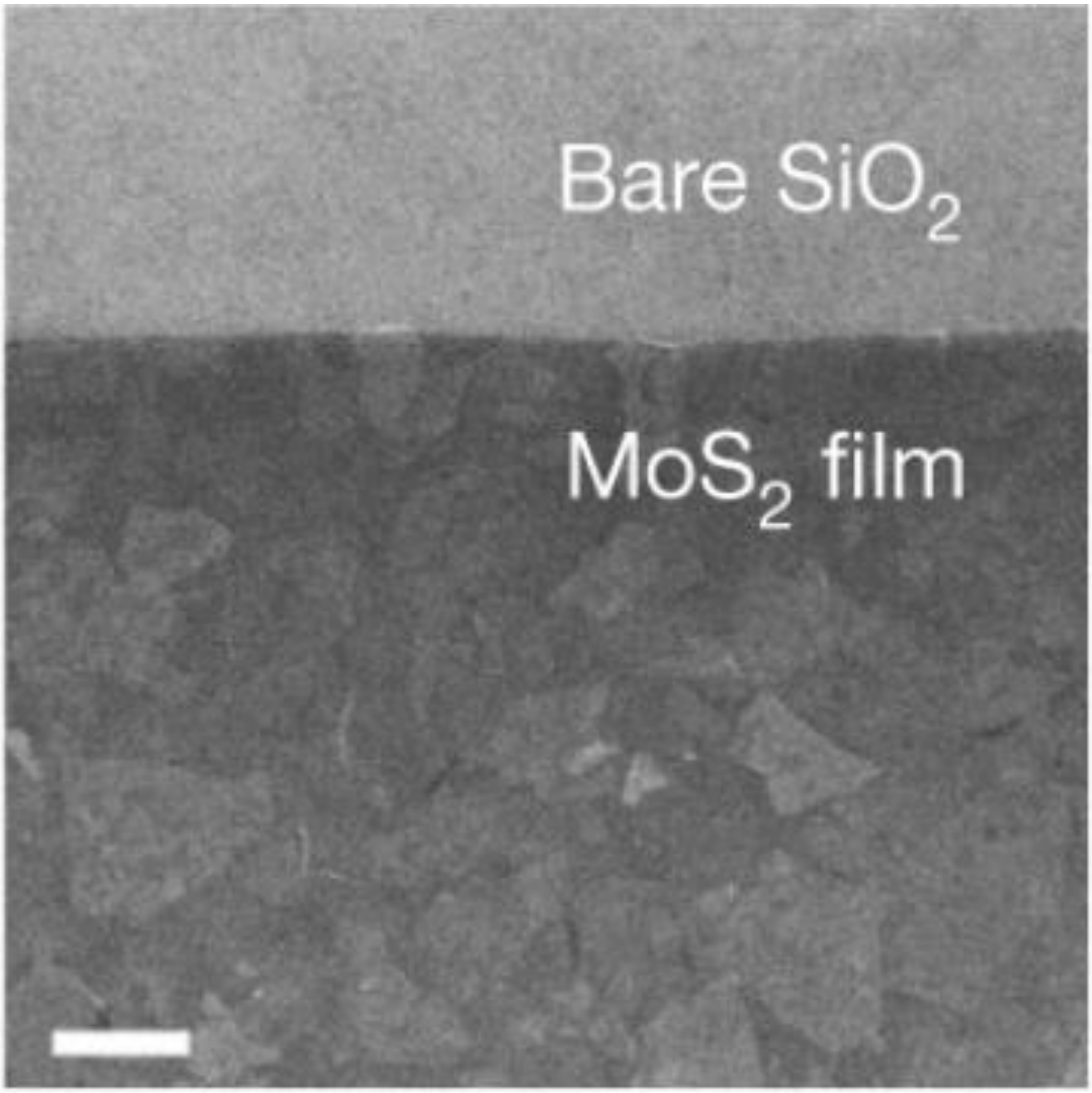

Figure 3.23 Scanning electron microscope image of solution deposited MoS_2 nanosheet film. The high-resolution imaging shows flat orientation of the nanosheets on the SiO_2 wafer. Scale bar is 1 μm.

To show devices could be made over a large area, photolithography along with reactive ion etch and metal evaporation was used to make several transistor devices across an entire wafer (Fig. 24). A positive photoresist was used to pattern and CF_4 gas was used as the etching agent. The metal electrodes used were 30 nm titanium capped with 50 nm gold.

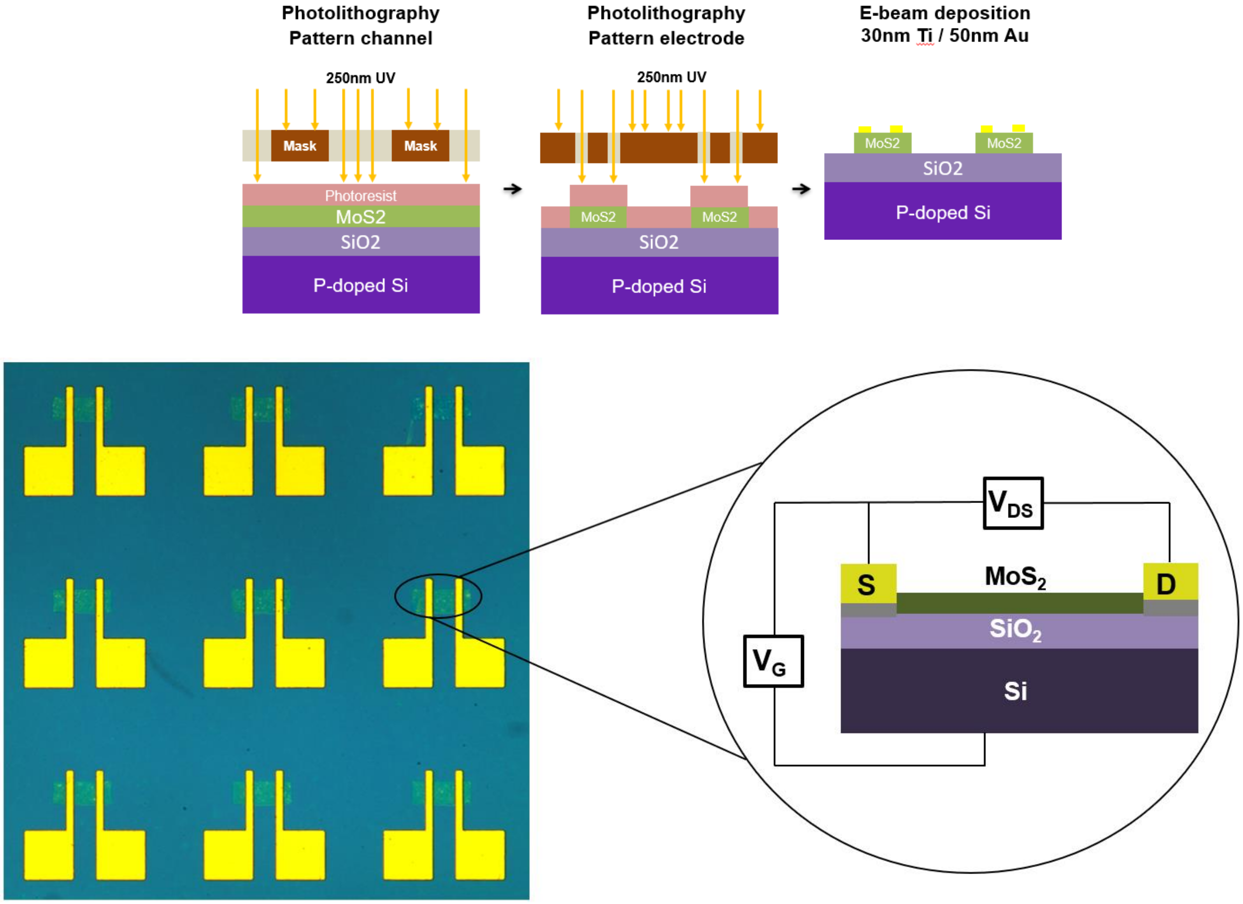

Figure 3.24 Photolithography process of patterning and etching the deposited film into semiconducting channels is detailed in the diagram above. These channels then had titanium/gold metal deposited as source and drain. An optical microscope picture showed the channels (40 μm by 100 μm). The devices fabricated were back-gate transistor devices.

The photolithography process could be successfully applied to form channels across the entire wafer (Fig. 25a). Using a mask, multiple sets of back-gate transistor devices could be made across the entire wafer. Using atomic force microscopy, the film thickness was measured to be 10 nm (Fig. 25b). Being able to apply photolithography allows large area devices to made on wafer scale with readily available technology. Fabricating multiple devices over a 100 mm (4 inch) wafer shows 2D nanostructure material can be used to solution process large-area electronics.

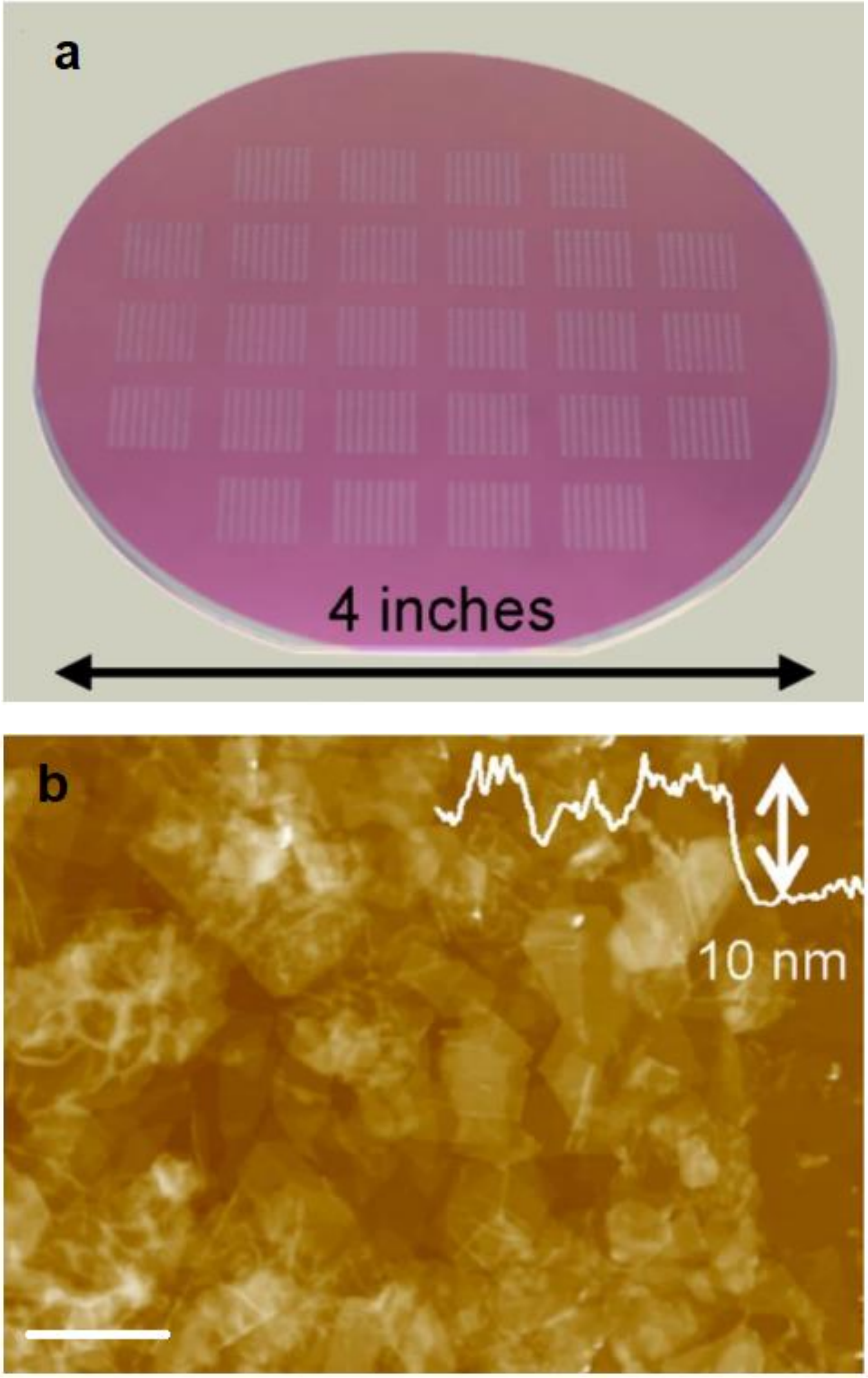

Figure 3.25 Devices made from the solution deposited MoS_2 thin-film. (a) The entire wafer that was previously covered with a thin-film of MoS_2 nanosheets through spin-coating was processed into multiple sets of transistor devices. (b) Atomic force microscopy image showing the average thickness of the film was 10 nm. The scanning bar was 2 μm.

The output characteristic ($I_{sd} – V_{sd}$) of the transistor devices made exhibited great linearity meaning the titanium electrodes were successfully deposited with no Schottky barrier (Fig. 26a).[31] The output was from devices fabricated on 90 nm SiO_2/Si wafer scanning from -10 V_g to 40 V_g. The transfer characteristics ($I_{sd} – V_g$) was typical of n-type MoS_2 transistor device (Fig.26b).[32] The devices made featured a large I_{on}/I_{off} ratio of 10^6. The thin-film device mobility ranged from 7-11 $cm^2 \cdot V^{-1} \cdot s^{-1}$. This matched closely with the single flake device mobility demonstrating the clean dangling bond free contacts between the layers. Ultimately the outstanding thin-film device data displays the superiority of 2D nanostructure contacts in thin-film when compared to other nanomaterials. The mobility of all devices was calculated using the formula shown below.

$$\mu = [\mathrm{d}I_{\mathrm{ds}}/\mathrm{d}V_{\mathrm{bg}}] \times [L/(WC_{\mathrm{i}}V_{\mathrm{ds}})]$$

The low temperature processing means plastic substrates could be used to produce flexible devices. Polyimide was used since its glass transition temperature is higher than the annealing temperature. MoS_2 thin-film was deposited onto a substrate of polyimide, and using atomic layer deposition, Al_2O_3 was deposited to act as a top gate dielectric (Fig. 27). Top-gate transistor devices were fabricated on polyimide and remained flexible after deposition of MoS_2. The transfer characteristics of the polyimide device showed similar performance as the one solution deposited onto 90 nm SiO_2/Si. This successfully demonstrated the ability to print flexible devices using 2D structured nanosheets.

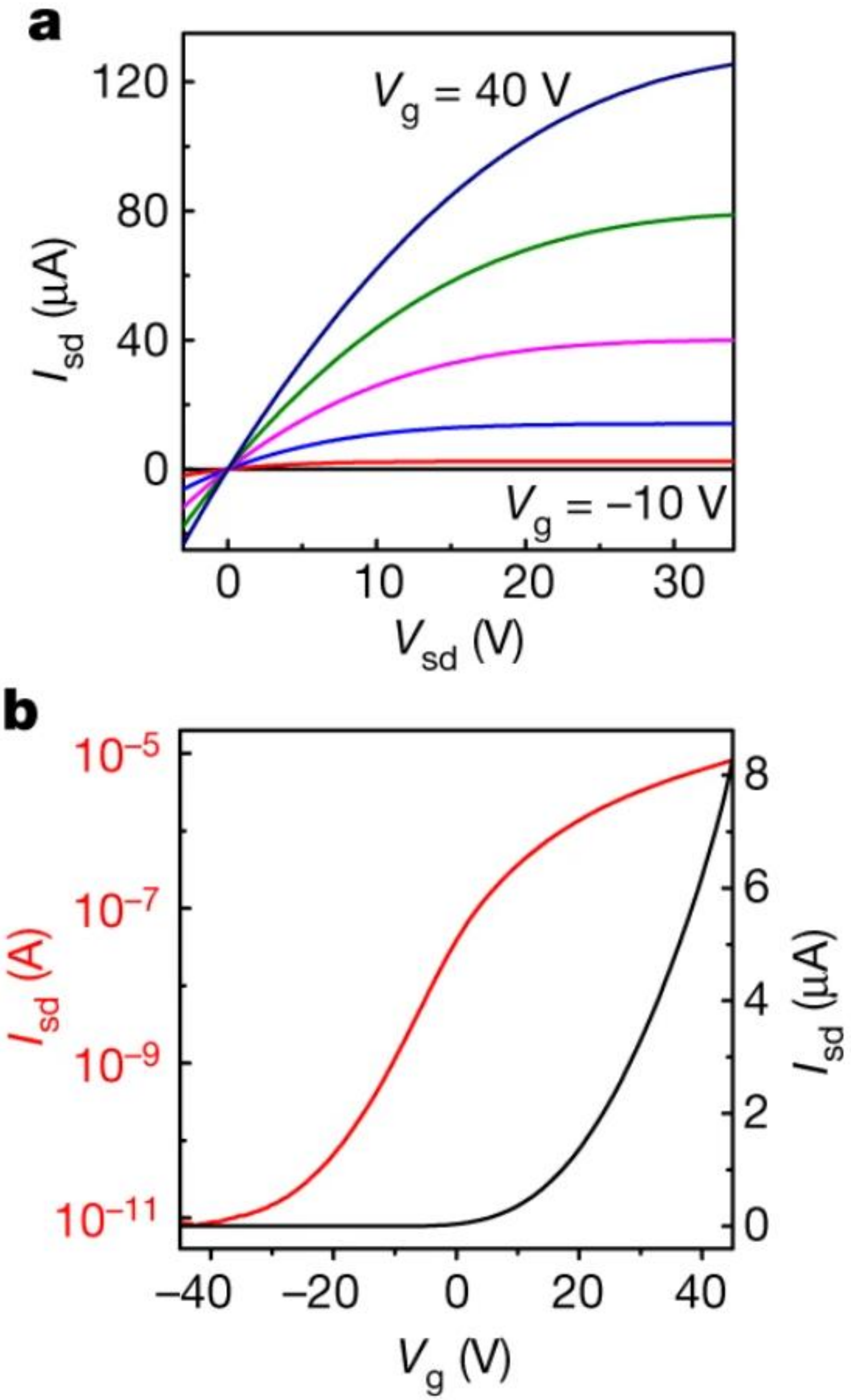

Figure 3.26 Devices characteristics of transistors fabricated on 90 nm SiO_2/Si. (a) Output characteristic scanning from -10 V_g to 40 V_g. (b) Transfer characteristic of the devices. Red line shows data in logarithmic form.

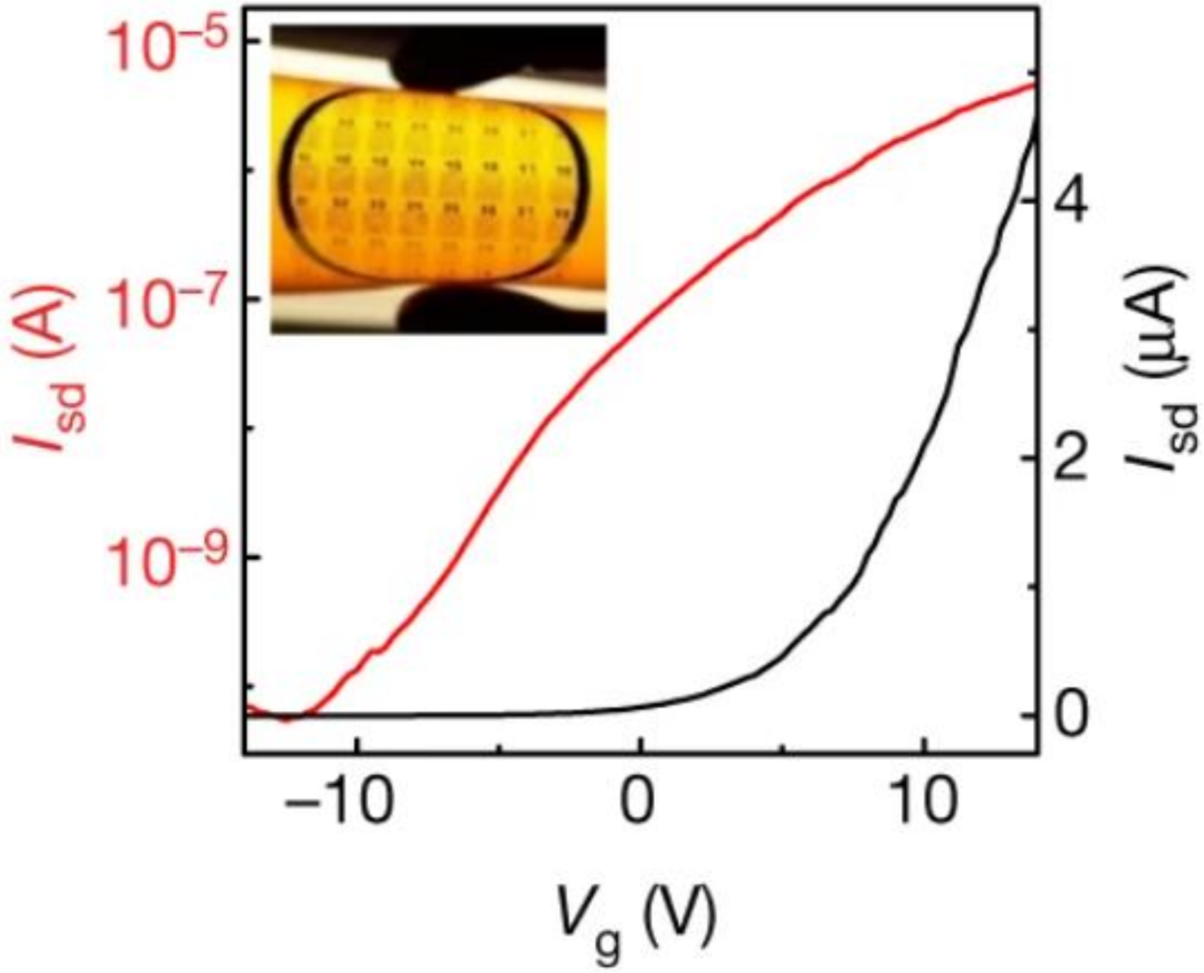

Figure 3.27 Flexible device made on polyimide substrate. The top-gate transfer characteristic shown is similar performance to the device produced on SiO_2.

3.4 Conclusion

Using electrochemistry, a top-down method was successfully employed to exfoliate bulk layered crystals down to nanosheets. Compared to pure liquid phase exfoliation, intercalation creates defect free nanosheets with very uniform thickness. Intercalating large tetraalkylammonium molecules weakens the van der Waals interaction between the layers allowing for gentle bath sonicator exfoliation. The intercalation proceeded using the crystal as a cathode in an electrochemical cell setup, avoiding any oxidation reactions from causing defects. Avoiding the large amounts of electron injected into the crystal prevented any phase change from occurring. The colloidal nanosheets that were produced could be concentrated down to an ink and dispersed in a variety of different solvents. The ink was shown to deposit large-area films through established printing processes. Using photolithography fabrication, devices could be made over an entire wafer. Avoiding any high temperature in the entire process means flexible devices could be made on plastic substrates. This confirms large organic molecule intercalation and exfoliation as a promising top-down method for producing colloidal 2D functional inks for printable large area electronics. For the next chapter we will show how by using crystal growth and whole library of layered crystals can be used as cathodic material to be intercalated and exfoliated. This allows the creation of a variety of different nanosheet inks.

3.5 Reference

1. Allen, M. J.; Tung, V. C.; Kaner, R. B. Honeycomb Carbon: A Review of Graphene. *Chem. Rev.* **2010**, 110, 132−145.
2. Singh, E.; Singh, P.; Kim, K. S.; Yeom, G. Y.; Nalwa, H. S. Flexible Molybdenum Disulfide (MoS2) Atomic Layers for Wearable Electronics and Optoelectronics. *ACS Appl. Mater. Interfaces* **2019**, 11, 11061−11105.
3. Han, J. H.; Kwak, M.; Kim, Y.; Cheon, J. Recent Advances in the Solution-Based Preparation of Two-Dimensional Layered Transition Metal Chalcogenide Nanostructures. *Chem. Rev.* **2018**, 118, 6151−6188.
4. Yi, M.; Shen, Z. A review on mechanical exfoliation for the scalable production of graphene. *J. Mater. Chem. A* **2015**, 3, 11700−11715.
5. Nicolosi, V.; Chhowalla, M.; Kanatzidis, M. G.; Strano, M. S.; Coleman, J. N. Liquid Exfoliation of Layered Materials. *Science* **2013**, 340, 1420.
6. Nicolosi, V.; Chhowalla, M.; Kanatzidis, M. G.; Strano, M. S.; Coleman, J. N. Liquid Exfoliation of Layered Materials. *Science* **2013**, 340, 1420.
7. Du, W. C.; Lu, J.; Sun, P. P.; Zhu, Y. Y.; Jiang, X. Q. Organic saltassisted liquid-phase exfoliation of graphite to produce high-quality graphene. *Chem. Phys. Lett.* **2013**, 568, 198−201.
8. Zhi, C. Y.; Bando, Y.; Tang, C. C.; Kuwahara, H.; Golberg, D. Large-Scale Fabrication of Boron Nitride Nanosheets and Their Utilization in Polymeric Composites with Improved Thermal and Mechanical Properties. *Adv. Mater.* **2009**, 21, 2889−2893.

9. Bang, G. S.; Nam, K. W.; Kim, J. Y.; Shin, J.; Choi, J. W.; Choi, S. Y. Effective Liquid-Phase Exfoliation and Sodium Ion Battery Application of MoS2 Nanosheets. *ACS Appl. Mater. Interfaces* **2014**, 6, 7084−7089.
10. Coleman, J. N.; Lotya, M.; O'Neill, A.; Bergin, S. D.; King, P. J.; Khan, U.; Young, K.; Gaucher, A.; De, S.; Smith, R. J.; Shvets, I. V.; Arora, S. K.; Stanton, G.; Kim, H.-Y.; Lee, K.; Kim, G. T.; Duesberg, G. S.; Hallam, T.; Boland, J. J.; Wang, J. J.; Donegan, J. F.; Grunlan, J. C.; Moriarty, G.; Shmeliov, A.; Nicholls, R. J.; Perkins, J. M.; Grieveson, E. M.; Theuwissen, K.; McComb, D. W.; Nellist, P. D.; Nicolosi, V. TwoDimensional Nanosheets Produced by Liquid Exfoliation of Layered Materials. *Science* **2011**, 331, 568−571.
11. Hanlon, D.; Backes, C.; Higgins, T. M.; Hughes, M.; O'Neill, A.; King, P.; McEvoy, N.; Duesberg, G. S.; Mendoza Sanchez, B.; Pettersson, H.; Nicolosi, V.; Coleman, J. N. Production of Molybdenum Trioxide Nanosheets by Liquid Exfoliation and Their Application in High-Performance Supercapacitors. *Chem. Mater.* 2014, 26, 1751− 1763.
12. Zeng, X.; Hirwa, H.; Metel, S.; Nicolosi, V.; Wagner, V. Solution Processed Thin Film Transistor from Liquid Phase Exfoliated MoS2 Flakes. *Solid State Electron.* **2018**, 141, 58−64.
13. Abdelkader, A. M.; Cooper, A. J.; Dryfe, R. A. W.; Kinloch, I. A. How to Get Between the Sheets: a Review of Recent Works on the Electrochemical Exfoliation of Graphene Materials from Bulk Graphite. *Nanoscale* **2015**, 7, 6944−6956.
14. Lukowski, M. A.; Daniel, A. S.; Meng, F.; Forticaux, A.; Li, L.; Jin, S. Enhanced Hydrogen Evolution Catalysis from Chemically Exfoliated Metallic MoS2 Nanosheets. *J. Am. Chem. Soc.* **2013**, 135, 10274−10277.

15. Yuwen, L. H.; Yu, H.; Yang, X. R.; Zhou, J. J.; Zhang, Q.; Zhang, Y. Q.; Luo, Z. M.; Su, S.; Wang, L. H. Rapid Preparation of Single-Layer Transition Metal Dichalcogenide Nanosheets via Ultrasonication Enhanced Lithium Intercalation. *Chem. Commun.* **2016**, 52, 529−532.

16. Ambrosi, A.; Sofer, Z.; Pumera, M. Lithium Intercalation Compound Dramatically Influences the Electrochemical Properties of Exfoliated MoS2. *Small* **2015**, 11, 605−612.

17. Yoon, G.; Seo, D.-H.; Ku, K.; Kim, J.; Jeon, S.; Kang, K. Factors Affecting the Exfoliation of Graphite Intercalation Compounds for Graphene Synthesis. *Chem. Mater.* **2015**, 27 (6), 2067−2073.

18. Grayfer, E. D.; Kozlova, M. N.; Fedorov, V. E. Colloidal 2D Nanosheets of MoS2 and Other Transition Metal Dichalcogenides Through Liquid-phase Exfoliation. Adv. Colloid *Interface Sci.* **2017**, 245, 40−61.

19. Jawaid, A.; Nepal, D.; Park, K.; Jespersen, M.; Qualley, A.; Mirau, P.; Drummy, L. F.; Vaia, R. A. Mechanism for Liquid Phase Exfoliation of MoS2. *Chem. Mater.* **2016**, 28 (1), 337−348.

20. Qiao, W.; Yan, S.; Song, X.; Zhang, X.; He, X.; Zhong, W.; Du, Y. Luminescent Monolayer MoS2 Quantum Dots Produced by Multiexfoliation Based on Lithium Intercalation. *Appl. Surf. Sci.* **2015**, 359, 130−136.

21. Zeng, Z. Y.; Yin, Z. Y.; Huang, X.; Li, H.; He, Q. Y.; Lu, G.; Boey, F.; Zhang, H. Single-Layer Semiconducting Nanosheets: HighYield Preparation and Device Fabrication. Angew. *Chem., Int. Ed.* **2011**, 50, 11093−11097.

22. Fan, X.; Xu, P.; Zhou, D.; Sun, Y.; Li, Y. C.; Nguyen, M. A. T.; Terrones, M.; Mallouk, T. E. Fast and Efficient Preparation of Exfoliated 2H MoS2 Nanosheets by Sonication-

Assisted Lithium Intercalation and Infrared Laser-Induced 1T to 2H Phase Reversion. *Nano Lett.* **2015**, 15, 5956−5960.

23. Kappera, R.; Voiry, D.; Yalcin, S. E.; Branch, B.; Gupta, G.; Mohite, A. D.; Chhowalla, M. Phase-Engineered Low-Resistance Contacts for Ultrathin MoS2 Transistors. *Nat. Mater.* **2014**, 13, 1128− 1134.
24. Eda, G.; Yamaguchi, H.; Voiry, D.; Fujita, T.; Chen, M.; Chhowalla, M. Photoluminescence from Chemically Exfoliated MoS2. *Nano Lett.* **2011**, 11, 5111−5116.
25. Duerloo, K. A.; Li, Y.; Reed, E. J. Structural Phase Transitions in Two-Dimensional Mo- and W- Dichalcogenide Monolayers. *Nat. Commun.* **2014**, 5, 4214.
26. Li, Y.; Duerloo, K.-A. N.; Wauson, K.; Reed, E. J. Structural Semiconductor-to-Semimetal Phase Transition in Two-Dimensional Materials Induced by Electrostatic Gating. *Nat. Commun.* **2016**, 7, 10671.
27. Mousavi, M. P. S.; Kashefolgheta, S.; Stein, A.; Bü hlmann, P. Electrochemical Stability of Quaternary Ammonium Cations: An Experimental and Computational Study. *J. Electrochem. Soc.* **2016**, 163, H74−H80
28. Jawaid, A.; Nepal, D.; Park, K.; Jespersen, M.; Qualley, A.; Mirau, P.; Drummy, L. F.; Vaia, R. A. Mechanism for Liquid Phase Exfoliation of MoS2. *Chem. Mater.* **2016**, 28, 337−348.
29. Lee, C.; Yan, H.; Brus, L. E.; Heinz, T. F.; Hone, J.; Ryu, S. Anomalous Lattice Vibrations of Single- and Few-Layer MoS2. *ACS Nano* **2010**, 4, 2695−2700.
30. Parkin, W. M.; Balan, A.; Liang, L.; Das, P. M.; Lamparski, M.; Naylor, C. H.; Rodríguez-Manzo, J. A.; Johnson, A. T. C.; Meunier, V.; Drndic, M. Raman Shifts in Electron-Irradiated Monolayer MoS´ 2. *ACS Nano* **2016**, 10, 4134−4142.

31. Zhou, H. L.; Wang, C.; Shaw, J. C.; Cheng, R.; Chen, Y.; Huang, X. Q.; Liu, Y.; Weiss, N. O.; Lin, Z. Y.; Huang, Y.; Duan, X. F. Large area growth and electrical properties of p-type WSe2 atomic layers. *Nano Lett.* **2015**, 15, 709−713.
32. Radisavljevic, B.; Radenovic, A.; Brivio, J.; Giacometti, V.; Kis, A. Single-Layer MoS2 Transistors. *Nat. Nanotechnol.* **2011**, 6, 147–150.

Chapter 4. Bulk crystal growth of layered crystals for electrochemical exfoliation

4.1 Introduction

Cathodic electrochemical intercalation and exfoliation of van der Waals layered crystals is the current state of the art method for producing top-down nanosheets.[1] The previous chapter demonstrated that it is possible to exfoliate pristine highly crystalline nanosheets that retain their intrinsic value while avoiding any defects from heavy sonication found in pure liquid phase exfoliation. Performing intercalation on the cathode avoids anodic based oxidation from intercalation of negatively charged species.[2] For cathodic intercalation an electrochemical cell is utilized to drive the intercalation process forward. A positively charged species such as large ammonium ions are used as the foreign intercalant to be inserted into the layered host crystal. In the case of anodic intercalation, electrons are withdrawn from the layered crystal thereby oxidizing the material in order to drive a negatively charged ion into the layers (Fig. 1).

The layered crystal itself acts as the electrode while a counter such as graphite or platinum is used to complete the circuit.[3-5] Typically, a polar aprotic solvent is used with a solubilized salt to form the electrolyte. A requirement of cathodic electrochemical intercalation exfoliation is that the crystal must be large enough to be suspended in the electrochemical cell and must be highly crystalline.[6] Pieces that are too small or powdered samples cannot be attached to the suitable substrate to be used as a standalone electrode. In contrast pure liquid exfoliation can simply disperse nonhomogeneous powder form of layered crystals in solution and pulverized into nanosheets. Naturally occurring layered crystals are limited to graphite, molybdenite, tungstenite, muscovite, and clays.[7-12] These crystals are usually from mined sources and not always large enough in size to act as electrodes for an electrochemical cell. The previous chapter used MoS_2 from mined byproduct, with pieces large enough to be used.

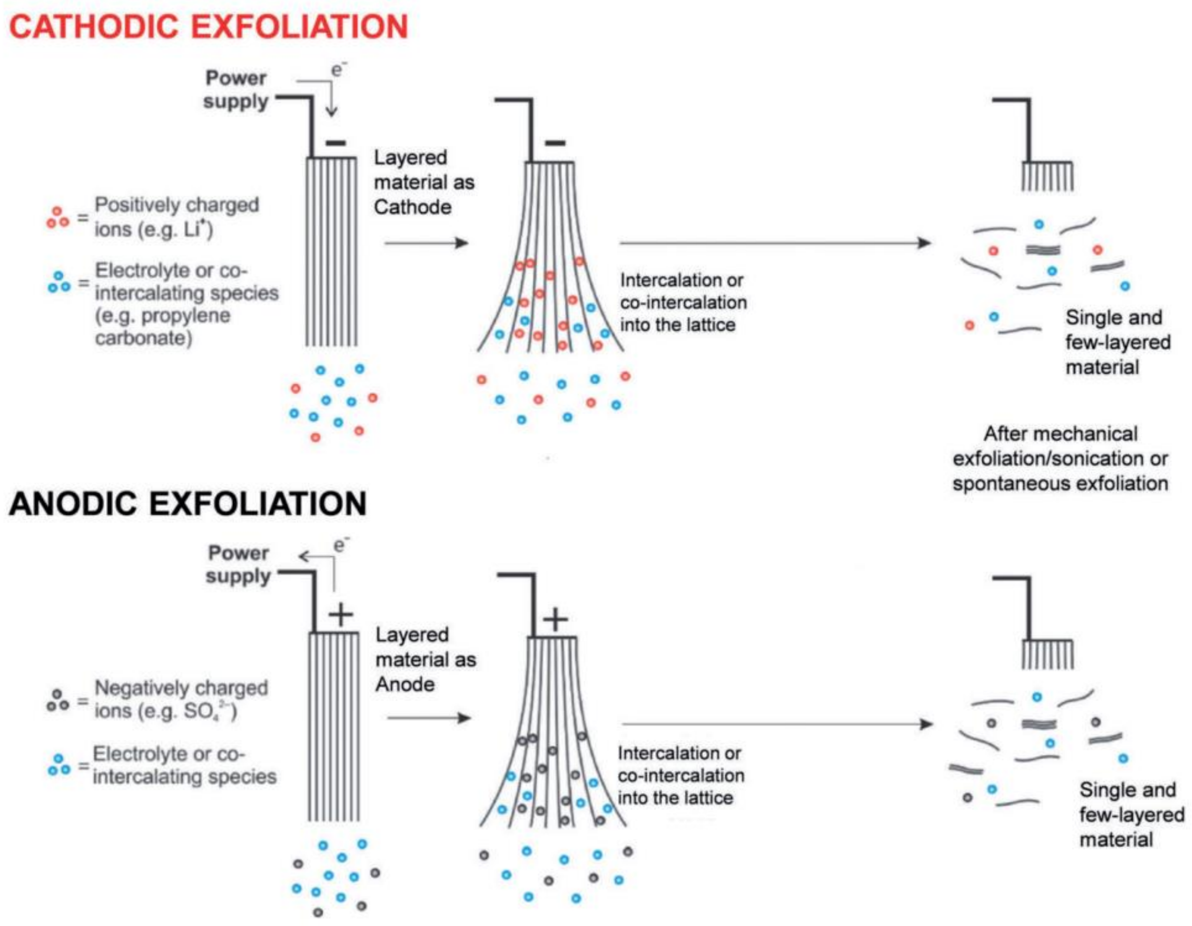

Figure 4.1 Electrochemical intercalation both on cathode side and anode side. Cathode side intercalates positively charged ions by injection electrons into the layered crystal. Anode involves oxidizing the layered material to intercalate negatively charged ions. *Adapted from reference 6.*

To be able to really expand on cathodic top-down exfoliation requires access to a variety of different crystals with different properties. These crystals need to be grown large enough (minimum of 0.5 cm in length) to be used as electrodes. Instead of being limited to naturally occurring van der Waal layered crystals, which are few in nature, crystal growth can be used to expand the possible nanosheets to be exfoliated. Crystal growth is the center piece of modern technology. Being able to grow monocrystalline silicon in large quantities has been the key to modern day integrated computer chips, photovoltaic cells and sensors.[13,14] Using crystal growth synthesis a large number of van der Waals layered crystals can be grown on the centimeter scale.

Many of these bulk layered materials have different electronic, physical and optoelectronic properties ranging from insulator to superconductors.[15-19] This wide range of different properties means the nanosheets from exfoliated bulk has found applications from electronic devices, energy storage, catalysis, sensors and even biomedicines.[20-32] Being able to exfoliate them down to nanosheets in colloidal phase allows them to be used as building blocks in large-area solution-based applications. Using cathodic intercalation and exfoliation ensures pristine nanosheets that retain the bulk properties. This allows a wider scope of solution based 2D nanosheet applications than just relying on graphite or MoS_2.

When it comes to crystal growth of van der Waals layered crystals there is mainly three different techniques to exploit. The first is known as melt solidification which includes Bridgeman-Stockbarger.[33] Here the precursors are melted into a homogenous mix, the reaction occurs in molten liquid phase and the crystallization occurs through slow cooling of the melt. Flux crystal growth is another liquid phased crystal growth technique. Here typically salts or metals that liquify at high temperatures are used as solvents for the crystal growth. The precursors become soluble in the flux where it is allowed to react. Afterwards the mixture is cooled and the desired crystal is precipitated out of the flux.[34] Vapor transport crystal growth is considered the most versatile technique since it does not depend on using soluble precursors or precursors with low melting points.[35] The precursor typically the raw metal, metal oxides and chalcogenides are placed on one side of an ampoule. A volatile transport agent along with a temperature gradient is used to transport the precursor to the cold ampoule side. The reaction occurs in vapor phase before being deposited as a solid.[36] Some typical vapor transport agents are halogens and chalcogens such as chlorine, iodine, selenium, and bromine.

We will show in this chapter that using bulk crystal growth techniques a wide variety of van der Waals layered crystals can be grown. Utilizing melt-solidification and vapor transport crystal growth techniques a multitude of different crystals are grown, such as: InSe, In_2Se_3, Sb_2Se_3, black phosphorus, Bi_2Se_3, SnS_2, $SnSe_2$, $MoSe_2$, and WSe_2. These could be grown on centimeter scale to act as electrode material for electrochemical intercalation. We show that similar to naturally occurring layered crystals, ones grown in lab can also be intercalated and exfoliated down to nanosheets. This allows for the creation of a wide variety of different nanosheets and opens the possibility for further production of electrochemical nanosheet synthesis by intercalation and exfoliation in order to create a library of functional inks.

Many of the crystals grown have different properties both electronically and physically. We also show that because of the low in plane Young's modulus of crystals such as InSe, In_2Se_3, and Bi_2Se_3 allows them to be exfoliated down to monolayer. While crystals such as MoS_2 and graphite are typically exfoliated down to multilayers (3-12).[37] Nanosheet monolayers act as the purest and most versatile building blocks from bulk crystals. By capping the monolayers with different organics in solution, these can be reassembled into superlattices with varying properties. This allows the fabrication of superlattice thin-films to be assembled through printed methods with tunable properties based on the different organic molecule used.

4.2 Experimental

Chemicals: Indium (100 mesh powder, 99.99% metal basis), Bismuth (100 mesh powder, 99.99% metal basis), Tin (100 mesh powder, 99.99% metal basis), Antimony (100 mesh powder, 99.99% metal basis), Sulfur (powder, 99.98% metal basis), Selenium (100 mesh powder, 99.99%), Tungsten(IV) selenide (WSe_2, 99.8%), Molybdenum(IV) selenide ($MoSe_2$, 99.9%), Acetonitrile (ACN, 99.8%), Tetraheptylammonium bromide (THAB, 98%), Tetrabutylammonium bromide (TBAB, 98%), Tetradecylammonium bromide (TDAB, 98%), Cetrimonium bromide (CTAB, 98%), Sodium Chloride (NaCl, 99.0%), Dimethylformamide (DMf, 99.8%), Poly(vinyl pyrrolidone) (PVP, MW≈ 40,000), Isopropanol (practical grade), Acetone (practical grade), Graphite rod (low density, 99.995% trace metal basis), Red phosphorus lump (powder, 99.999% metal basis), Iodine (crystals, 99.9% metal basis), Ammonium thiocyanate (NH_4SCN, 99.99% metal basis). All chemicals were purchased from Sigma-Aldrich with no further processing.

Melt solidification crystal growth. For van der Waals layered crystals with metals that are easily melted (<1000 °C), melt solidification offers a great approach to growing large sized crystals. For crystals such as InSe, In_2Se_3, Bi_2Se_3, Sb_2Se_3, SnS_2, and $SnSe_2$ could be grown by simply melting the precursors together and allowing the mix to slowly cool to allow crystallization. A 1-centimeter diameter fused quartz tube was sealed on one end to form a sharp point to allow nucleation. All quartz ampoules were cleaned with soap, soaked in nitric acid overnight and then finally rinsed with isopropanol. The precursor was placed in stoichiometric contents. After precursor placement, the quartz tube was vacuumed down to a pressure of 5 millitorr and held for 1 hour to get rid of all oxygen in the environment. While under vacuum the tube was sealed using an acetylene oxygen torch. For some precursors such as indium or bismuth which react with quartz through a process called devitrification, a carbon coating was needed. A carbon coating was formed by coating the inside walls of a quartz tubes with 0.5 mL acetone. Afterwards this was heated with acetylene oxygen torch until a homogenous carbon coating was formed. The melt solidification synthesis was slowly heated in a tube furnace to appropriate temperature at the rate of 10 °C per hour until the desired temperature was reached. This slow heating ramp ensured the selenium or sulfur precursor would not vaporize too quickly and destroy the quartz ampoule. It was then typically held there for 72 hours before being slowly cooled at the rate of 5 °C per hour. This extremely slow cooling rate took place typically over the course of a week to allow high level of crystallization.

Vapor transport crystal growth. Similar to melt solidification crystal growth, a 0.5-inch quartz tube was sealed on one end. The ampoule was then cleaned with DI water, soap, soaked in nitric acid overnight and finally rinsed with isopropanol. For molybdenum diselenide ($MoSe_2$) and tungsten diselenide (WSe_2) was placed into the ampoule. The transport agent used was iodine for $MoSe_2$ and selenium for WSe_2. The transport agent concentration was roughly 7 mg per mL of quartz ampoule volume. Once precursor and transport agent were placed into the quartz ampoule, it was attached to a vacuum and pumped down for 1 hour. When iodine was used as the transport agent, the ampoule was vacuumed while the submerged in liquid nitrogen to prevent iodine from evaporating. For the vapor transport of black phosphorus, red phosphorus was used as the phosphor precursor. The transport agent was a mixture of tin to iodine in a 1:4 ratio. When heated this forms SnI_2 which vaporizes and transports the phosphorus. The precursor with transport agent side of the ampoule tube was placed in the center hot zone of the horizontal tube furnace. The growth region on the opposite side was placed into the cooler side of the furnace. The heating rates, and cooling rates were same as melt solidification. The temperature gradient was held for typically 9 days.

Monolayer intercalation exfoliation of synthetic layered crystals: A two electrode electrochemical cell was used. The crystals that were able to be intercalated and exfoliated down to monolayers (InSe, In_2Se_3, and Bi_2Se_3) were attached to copper clips acting as cathode electrode. The anode was a graphite rod with no additional modifications. An ammonium ion (CTAB, TBAB, THAB, TDAB) were dissolved in acetonitrile in concentration of 10 mg per mL acting as the electrolyte. The voltage applied was 5 volts to drive the intercalation process. Unlike MoS_2 the crystal faces broke off as intercalation went on. After 1 hour of intercalation, the acetonitrile was discarded and the solids were collected and sonicated in DMF. The nanosheets were collected after sonication and washed in DMF before being concentrated in DMF. For ligand exchange the nanosheets were dispersed into a 1 M DMF solution with the ligand of choice. This was allowed to exchange for a total of 3 hours.

Characterization. Characterization was carried out using multiple different instruments. For electron microscopy imaging scanning electron microscope (JEOL JSM-6700F FE-SEM) with EDS (EDAX), transmission electron microscope (T12 Quick CryoEM using acceleration voltage, 120 KV). X-ray diffraction (XRD, Panalytical X'Pert Pro X-ray Powder Diffractometer) was used to confirm crystal lattice of the crystals. UV–vis–NIR absorption spectroscopy (Shimadzu 3100 PC) was used to characterize the absorption characteristics. Atomic force microscopy (AFM, Bruker Dimension Icon Scanning Probe Microscope) using tapping mode was used to measure the thickness of the exfoliated nanosheet flakes. X-ray photoelectron spectroscopy (XPS, AXIS Ultra DLD) measured the oxidation state of the indium atom. For Raman and photoluminescence, a 488-nm wavelength laser was used as excitation light from Horiba. Electrochemical measurements were done using an electrochemical analyzer/workstation (CHI 600E).

4.3 Results and discussion

The sealed ampoules had dimensions of 15 centimeters in length and 1 centimeter in diameter. All glass used was pure quartz that was washed and etched with nitric acid. A vacuum system was assembled to pump down the ampoules to ensure no oxygen was present to oxidize the precursors. The total weight of the precursors ranged typically from 3 grams to 5 grams.

Adding too much of the precursors generated excess pressure which would break the quartz ampoule during crystal growth. The easiest method of growing van der Waals layered crystals was using melt solidification. This works well on for metal chalcogenides where the metal has a low melting point. The crystals were grown using a temperature programmed horizontal tube furnace. Since the reaction happens in the melt phase, this could grow large ingots of crystals. Some typical crystals grown using this method were tin selenide ($SnSe_2$) shown in (Fig. 2a) accompanied with its x-ray diffraction pattern shown in (Fig. 2b). In the case of tin selenide, the crystal could be grown as large as 4 centimeters.

Some metals that have low melting points can also react with the glass ampoules. This reaction is known as devitrification. In the case of devitrification typically results in the glass ampoule weakening making it more susceptible to breakage during the growth process. In addition to the grown crystals having strain defects, it is also very difficult to separate the crystals from the ampoule. In order to grow crystals such as indium monoselenide (InSe) and bismuth selenide (Bi_2Se_3), a carbon coating is required. A carbon coating is formed by applying a thin coating of acetone on the quartz ampoule and heating with an oxygen acetylene torch. This may need to be repeated to ensure a complete coating. After the coating is formed, it is rinsed and sonicated with methanol to remove any excess carbon that did not form a coating. In (Fig. 3a) and (Fig. 3b) are carbon coated grown InSe along with its x-ray diffraction pattern. Bismuth selenide was grown in a similar manner shown in (Fig. 4a) with accompanying x-ray diffraction pattern (Fig. 4b). From the x-ray diffraction we show no lattice strain and perfect crystallization along the (00l) plane. The sharp x-ray diffraction data with no peak broadening shows the high crystallinity of the final crystals grown. These ingots ranged in size from 1-2 cm and were easily cleavable with a razor along the layered planes.

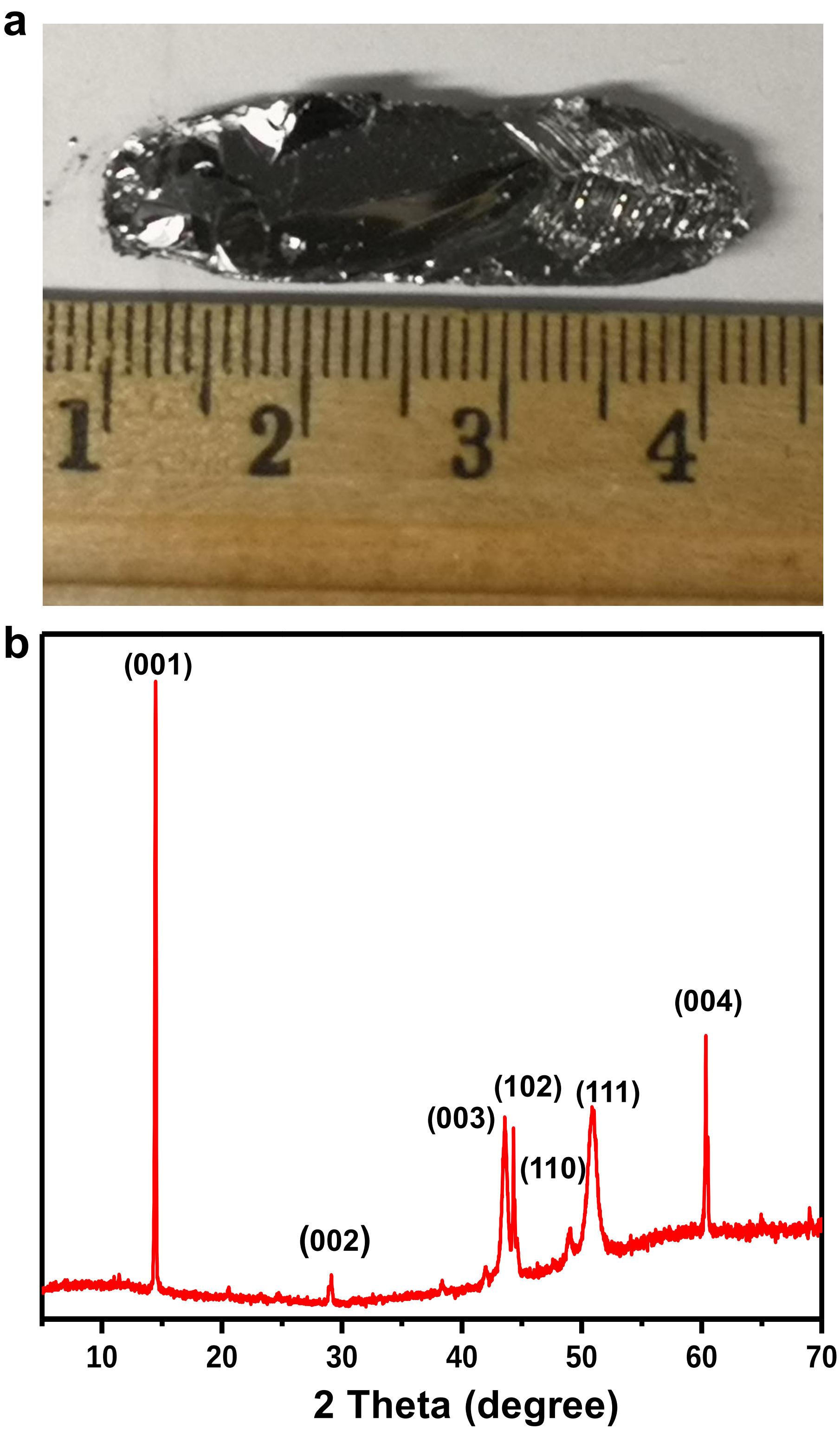

Figure 4.2 SnSe$_2$ crystal. (a) Picture of large SnSe$_2$ ingot grown from melt solidification. (b) X-ray diffraction pattern of SnSe$_2$.

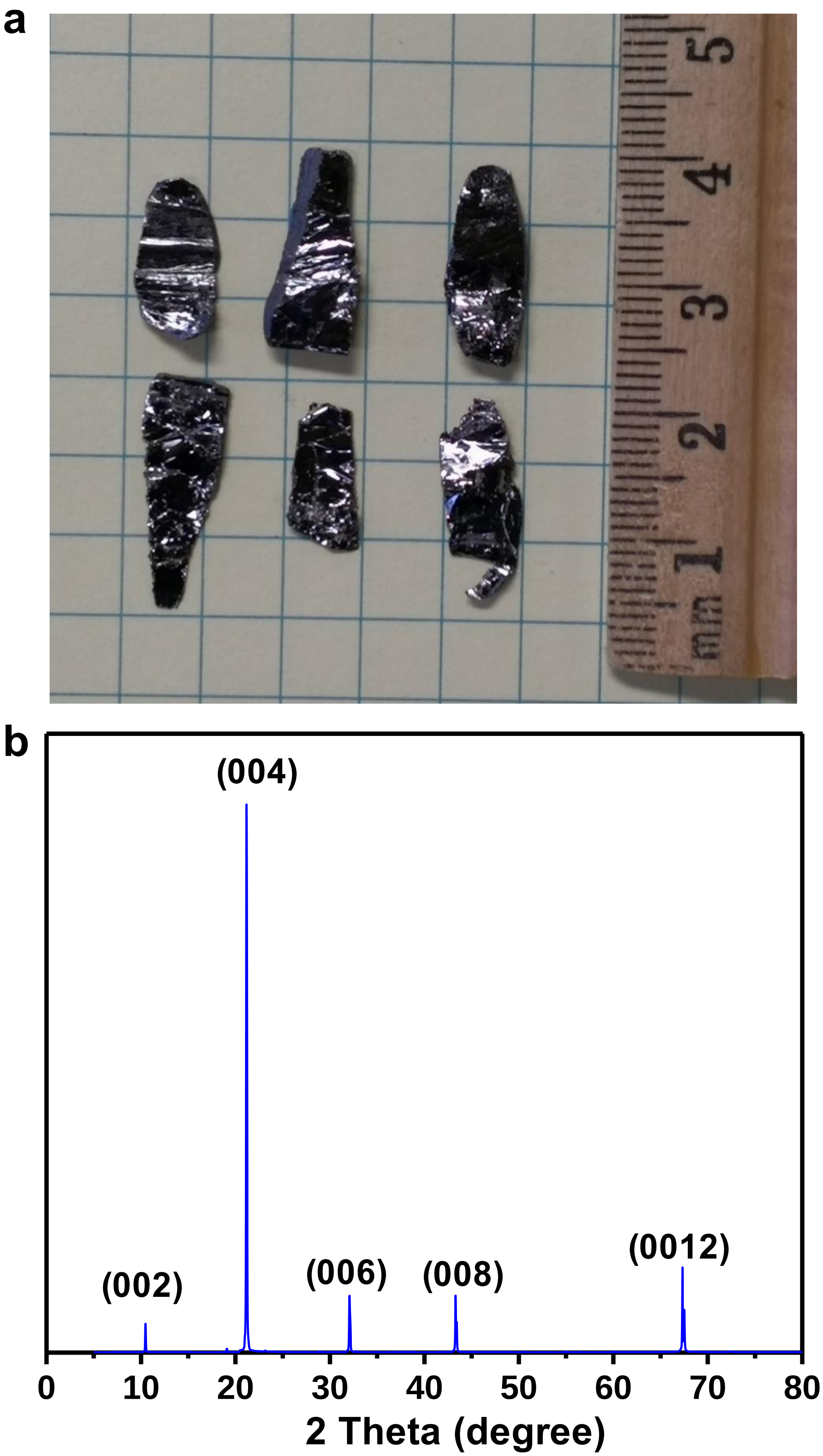

Figure 4.3 InSe crystal. (a) Picture of InSe crystals grown from melt. (b) X-ray diffraction pattern of InSe.

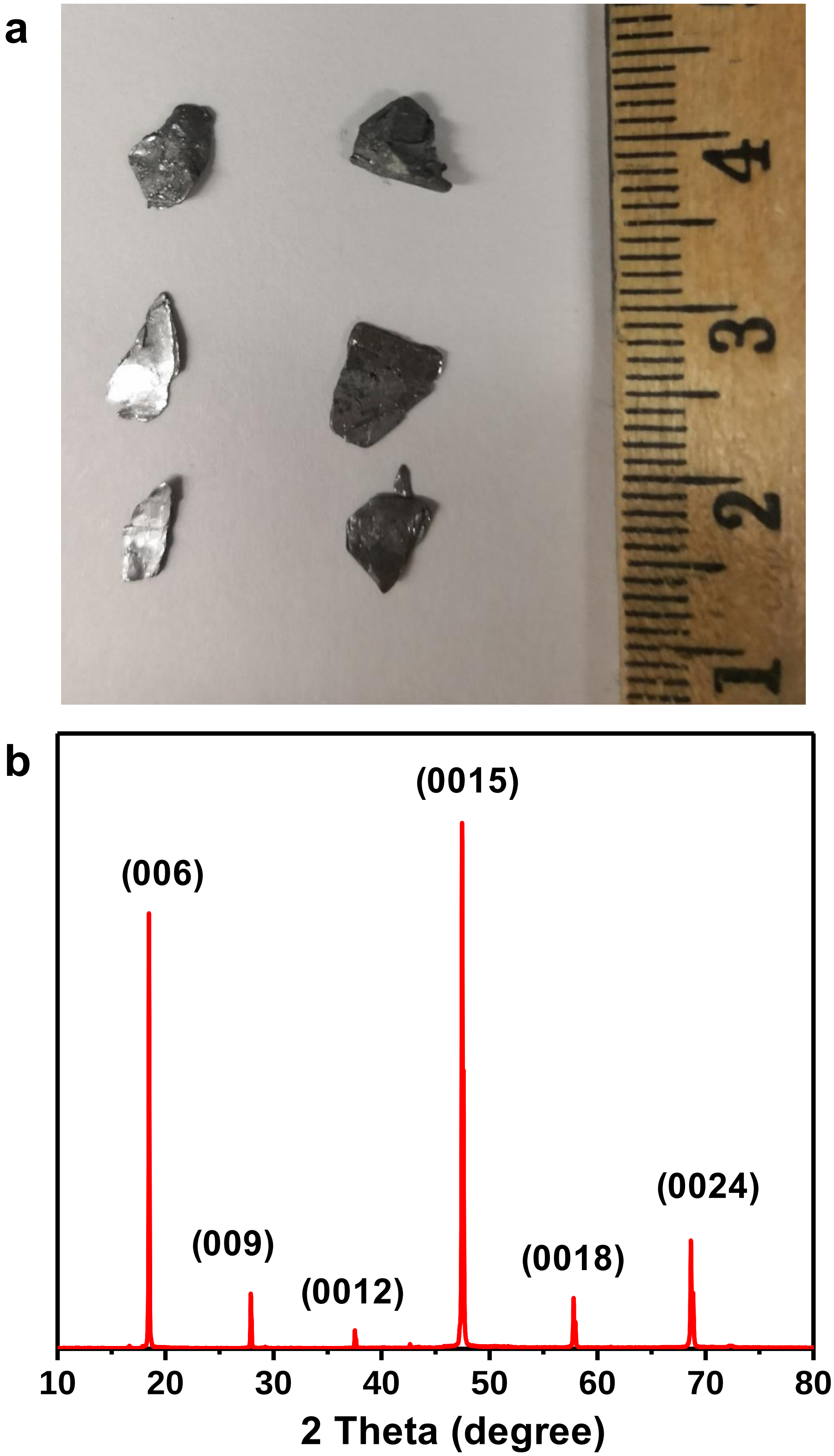

Figure 4.4 Bi_2Se_3 crystal. (a) Picture of Bi_2Se_3 crystals grown from melt. (b) X-ray diffraction pattern of Bi_2Se_3.

When growing crystals that used metals with high melting points (>1100 °C), vapor transported was needed. Many of the ampoule preparation steps were the same as melt solidification. The difference was the addition of a transporting agent. Here a volatile compound is added which transports the precursors through vapor phase from a hot side to a cool side. The reaction occurs in the vapor phase as it is deposited. For crystals such as molybdenum selenide ($MoSe_2$) and tungsten selenide (WSe_2), iodine was used as the transport agent. Black phosphorus (BP) was a unique case in that iodine combined with tin was needed to act as transport agent. The crystals grown using vapor transport were smaller than melt solidification but were still large enough to act as electrodes for electrochemical top-down intercalation exfoliation. The grown crystals of $MoSe_2$, BP, and WSe_2 are shown in (Fig. 5) with accompanying x-ray diffraction patterns.

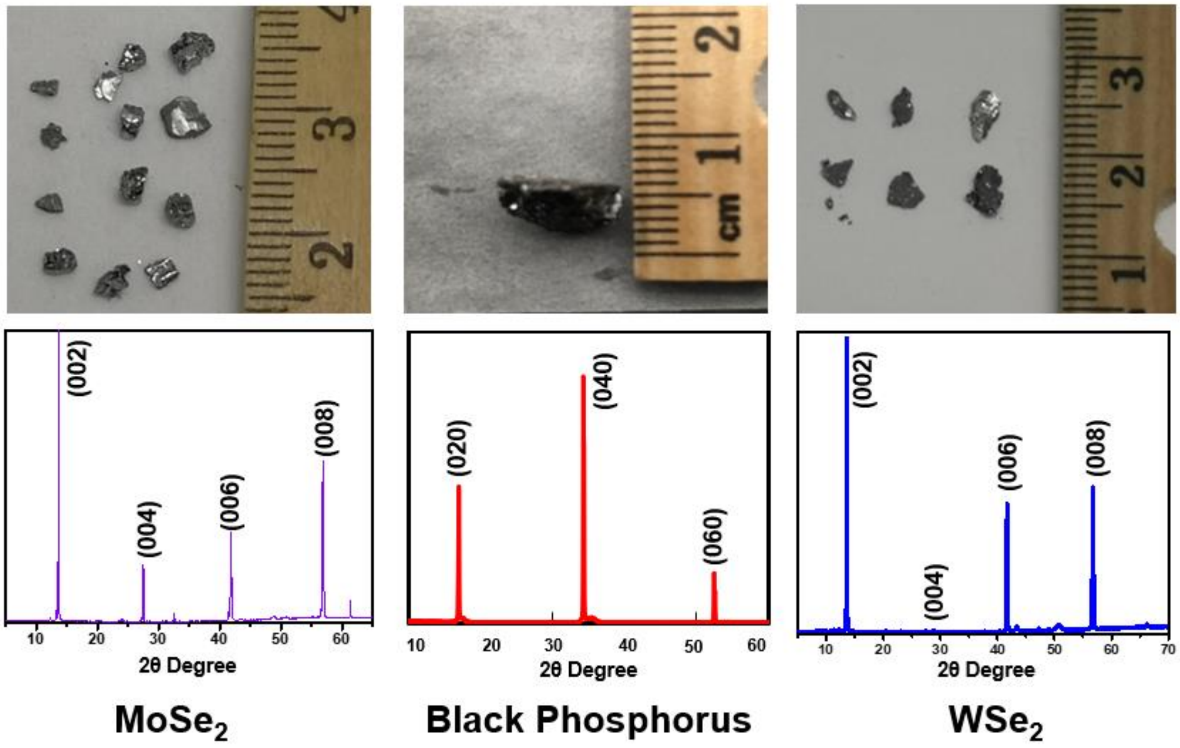

Figure 4.5 Crystals grown using vapor transport with corresponding x-ray diffraction patterns.

Using both vapor transport and melt solidification, a variety of different layered crystals could be grown. Similar to naturally occurring MoS_2 these crystals could also be electrochemically intercalated with large ammonium ions (Fig. 6a), here we show InSe being intercalated with THAB with large layered expansion. The expanded crystals could all be exfoliated in appropriate solvents such as dimethylformamide and N-Methyl-2-pyrrolidone. After exfoliation AFM data of black phosphorus exhibited that they could be exfoliated down into nanosheets (Fig. 6b), in this case black phosphorus was intercalated with THAB and exfoliated in dimethylformamide. This nanosheet formation was further confirmed using transmission electron microscopy with (Fig. 6c) showing a sample of exfoliated $MoSe_2$. Just like MoS_2, after solution depositing the nanosheets into a thin-film. The crystallinity remained from x-ray diffraction data (Fig. 6d). In this example, InSe was spin-coated onto SiO_2 substrate, there was no shifts in the diffraction pattern and all original peaks remained.

Being able to grow different van der Waals crystals expanded the possible functional nanosheet inks that could be produced through top-down intercalation and exfoliation. A large challenge was being able to grow the crystals in a large enough size to be used as individual electrodes in the electrochemical cell setup. Using both melt solidification and vapor transport a large variety of van der Waals layered crystals could be grown, all of which could be intercalated and exfoliated. This allowed for the creation of many different nanosheet inks (Fig. 7). Top-down intercalation and exfoliation has proven to create highly crystalline colloidal nanosheet solutions that can be printed into thin-films. Having access to a library of different colloidal nanosheets expands the possible applications of 2D nanostructures being used for printed electronic applications.

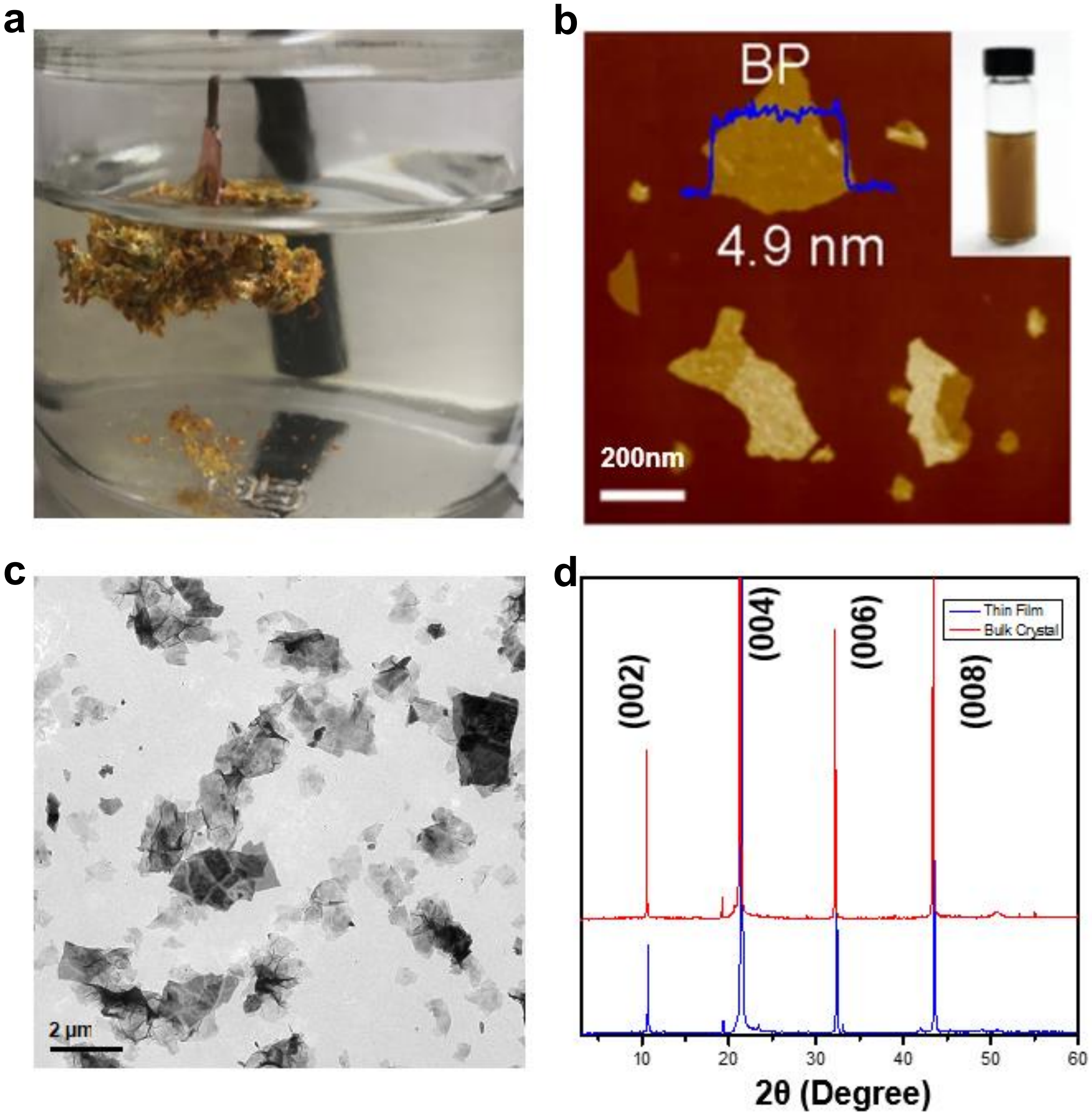

Figure 4.6 Images and data showing intercalation and exfoliated nanosheets from lab grown layered crystals. (a) Layered expansion of InSe. (b) Exfoliated nanosheets of black phosphorus. (c) Transmission electron microscope of $MoSe_2$ exfoliated nanosheet. (d) X-ray diffraction of solution deposited thin-film of InSe with matching peaks compared to bulk crystal.

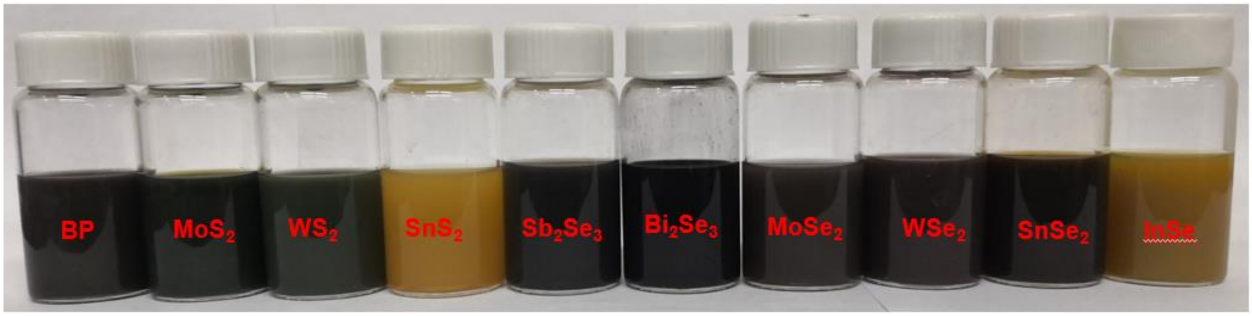

Figure 4.7 A total library of nanosheet inks produced from in lab grown crystals that were exfoliated through top-down electrochemical intercalation of large ammoniums and exfoliation.

From (Fig. 7) there is immediately obvious characteristic differences just based on their light absorption properties. A unique aspect is the difference in their physical properties ensuing different intercalation and exfoliation results. MoS_2 when intercalated expanded like a popcorn structure, however for crystals such as In_2Se_3 shown in (Fig. 8a) with its x-ray diffraction (Fig. 8b) did not show pure expansion. Instead as the intercalation process proceeded, the crystal would expand and shed individual flakes. This was also witnessed in InSe and Bi_2Se_3. What makes this different than MoS_2 was the individual flakes from In_2Se_3 were exfoliated down to monolayers capped with the tetraheptylammonium ion acting as a ligand. This is evident by the atomic force microscopy data (Fig. 9). Starting at a room temperature thickness of 1.9 nm, this size decreased as annealing steps were applied to the sample. As the temperature increased the organic ligand proceeded to burned off the nanosheet surface until 400 ^oC where all organics are burned off and pure monolayers were obtained. The ability to synthesize nanosheets down to pure monolayer has always been difficult for both top-down and bottom-up methods. Previous synthetic methods produced mixed phase thicknesses with no selectivity towards monolayers.

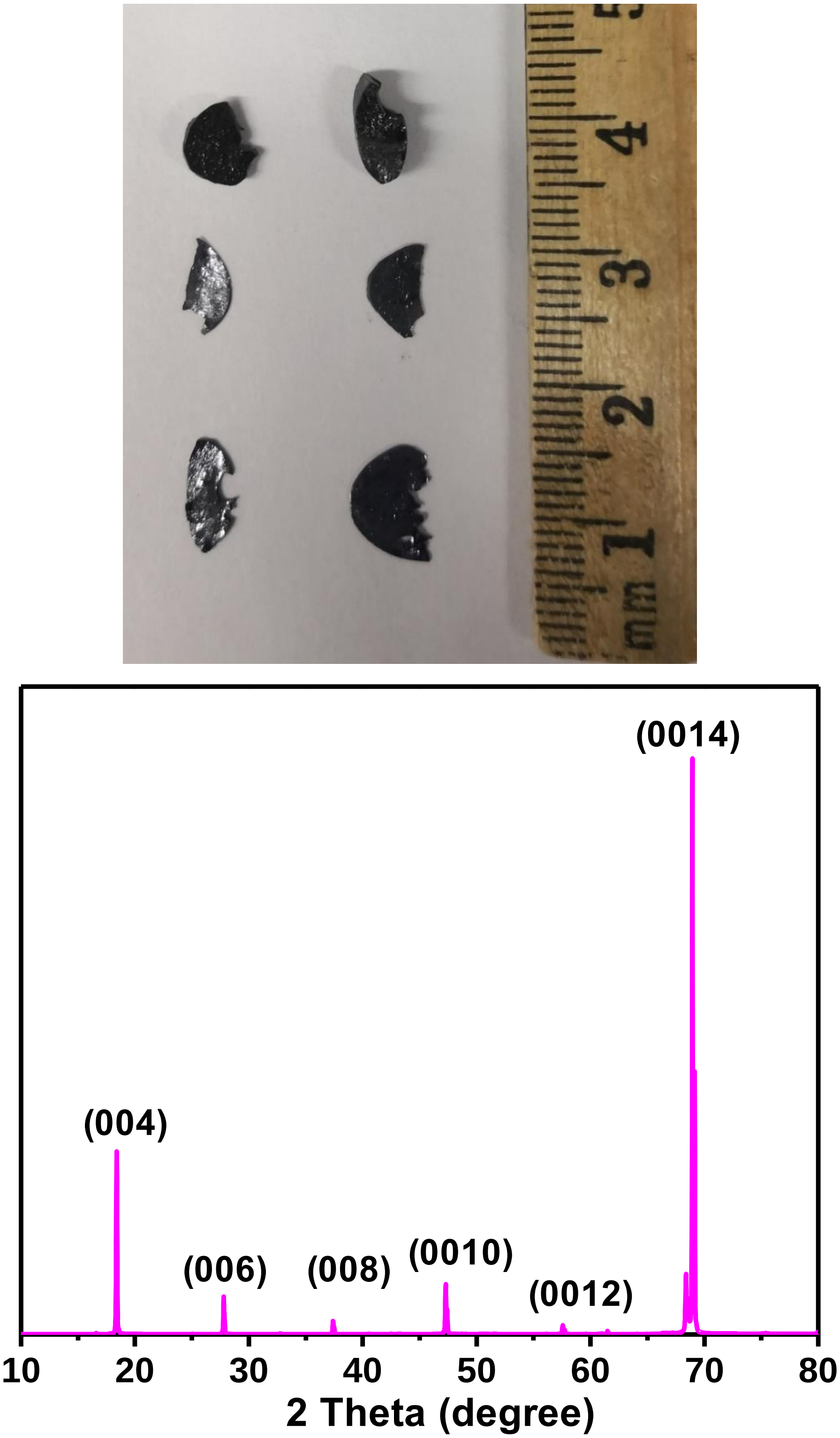

Figure 4.8 In_2Se_3 crystal. (a) Picture of In_2Se_3 crystals grown from melt solidification. (b) X-ray diffraction pattern of In_2Se_3 along the (00l) plane.

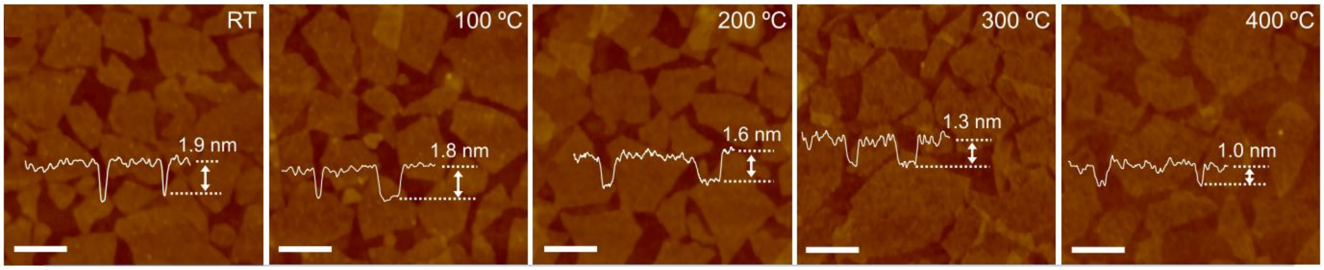

Figure 4.9 Atomic force microscopy of intercalated and exfoliated In_2Se_3 nanosheets. Starting at a thickness of 1.9nm is the nanosheet with a layer of organic ammonium ion surfactant. As temperature increases the organic surfactant vaporizes off the sheets reducing the thickness. Scale bar is 300 nm.

When compared to black phosphorus or MoS_2 which simply expanded into a popcorn structure. The breaking of the individual flakes during the intercalation process creates a self-refreshing effect to allow new layers of crystal to be intercalated (Fig. 10). The large expansion of organic molecules into the layers of the crystal creates a large strain within the crystal creating a self-retarding effect preventing any further intercalation. Whereas for In_2Se_3, InSe, and Bi_2Se_3 the breaking of the outer layer exposes new fresh layer to be intercalated with no strain effect. This in turn allows for the exfoliation of high percentage of monolayers, with In_2Se_3 and InSe being above 95% and Bi_2Se_3 being around 70% pure monolayer exfoliation.

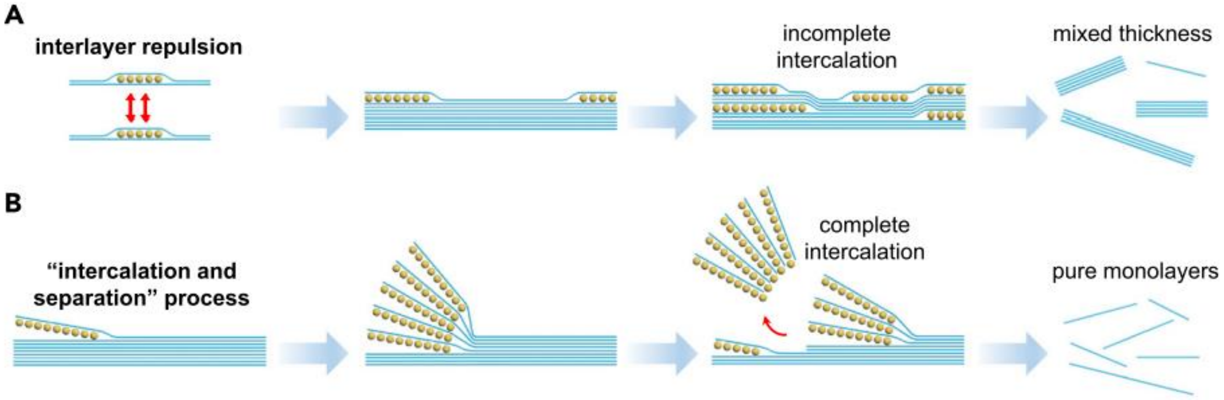

Figure 4.10. Illustrated diagram of intercalating large ammonium ions. (a) Electrostatic and strain repulsion causes incomplete intercalation leading to mix thickness nanosheets. (b) High induced strain layered crystals have a self-refreshing effect leading to pure monolayers.

An explanation for this is the small in-plane Youngs modulus of In_2Se_3, InSe, and Bi_2Se_3. Compared to MoS_2, their in-plane Youngs modulus were much lower at roughly 80 GPa versus 200 GPa for MoS_2. MoS_2 larger Youngs modulus means much less elasticity within the individual layers of the crystals. This lack of elasticity generated sufficient strain from ammonium intercalation to create interlayer repulsion during the insertion process. This can be further confirmed with scanning electron microscope data (Fig. 11). Pristine MoS_2 and In_2Se_3 both have tightly packed layered structure in its natural form. After intercalation we see a large amount of In_2Se_3 peeling off from the surface. For MoS_2 we instead observe simple expansion with large amounts of individual flakes being pushed out due to strain giving it the popcorn effect. Both were intercalated using THAB for 5 minutes under 5 Volts.

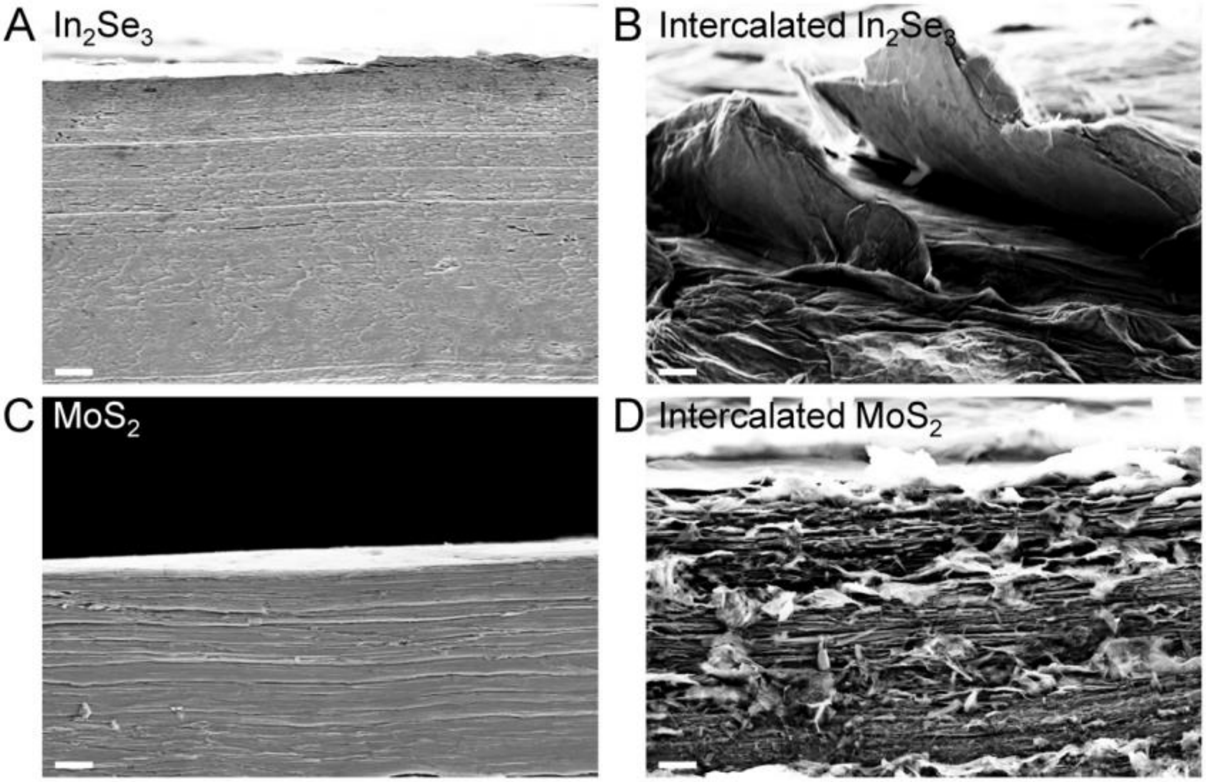

Figure 4.11. Scanning electron microscope images of layered crystals before and after intercalation. (a) In_2Se_3 before intercalation. (b) In_2Se_3 after intercalation. (c) MoS_2 before intercalation. (d) MoS_2 after intercalation. Scale bar is 20 μm.

The monolayer In_2Se_3 produced through intercalation and exfoliation remained the same valence state of In^{+3} and Se^{-2}, there was no lattice shift or stoichiometric phase shifts. This is evident by the X-ray photoelectron spectroscopy (XPS) data, that showed matching peaks even after several rounds of annealing (Fig. 12a). Uv-vis optical absorption data also showed no visible change in absorption property as organic molecules were removed from the surface (Fig. 12b). The absorption data alongside with X-ray photoelectron spectroscopy demonstrates the lack of material degradation undergoing annealing process. The elemental ratio remained 2:3 of indium to selenium from the energy dispersive spectroscopy data (Fig. 12c) which further confirms the X-ray photoelectron spectroscopy valence states. The maximum annealing temperature was within the glass transition temperature of amorphous resin polyimide (400 °C).

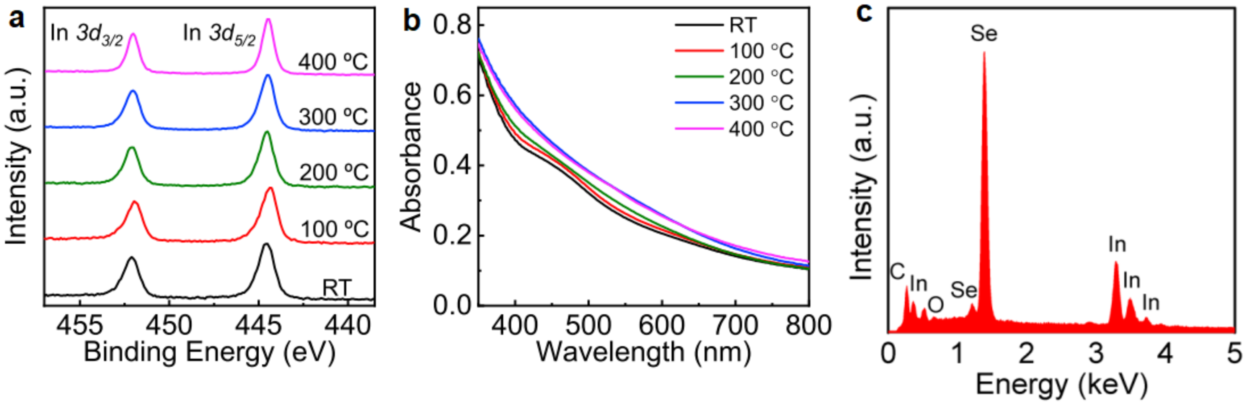

Figure 4.12. XPS, UV-vis absorption, and EDS data. (a) XPS data showing no change after annealing cycles at different temperatures. (b) Absorption spectroscopy showing no notable changes in absorption pattern after annealing cycles. (c) EDS showing a retained 2:3 ratio of indium to selenium.

In_2Se_3 monolayers were then processed into an ink solution and spin-coated onto 70 nm Si_3N_4 substrates. Using standard clean room techniques, back-gate thin-film transistors were fabricated. The transistors had an on/off current ratio of 10^5 with a mobility of 0.2 $cm^2 \cdot V^{-1} \cdot s^{-1}$ (Fig. 13), which were comparable to In_2Se_3 films synthesized through CVD.

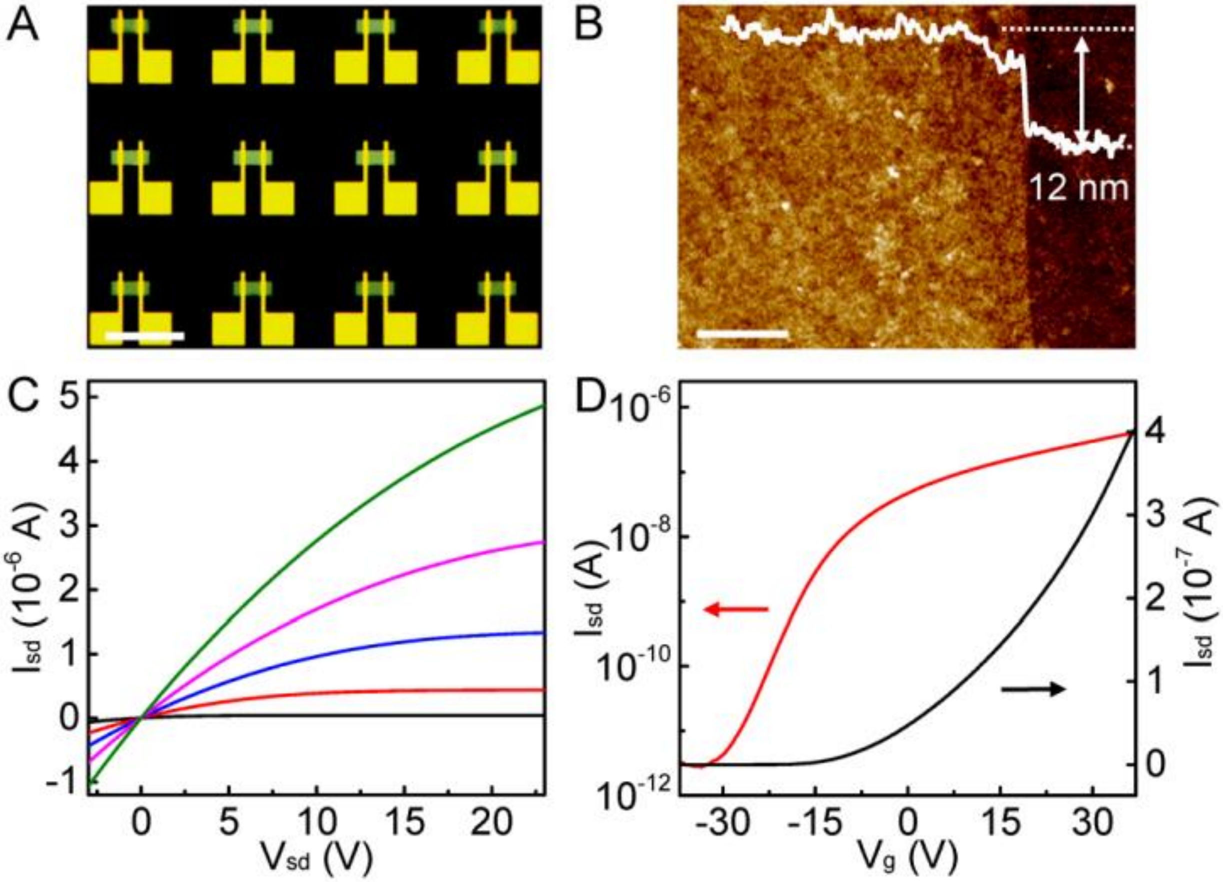

Figure 4.13. Back gate thin-film transistor data. (a) Optical microscope picture of thin-film transistors fabricated. Scale bar is 200 μm. (b) Atomic force microscopy image showing thickness of film was 12 nm. Scale bar is 2 μm. (c) Output characterization data with varying gate voltages from -10 to 30 V. (d) Transfer characterization data with source drain at 1 V.

What makes the ability to synthesize monolayers desired is the fact that they can be reassembled into superlattice materials. Here with the organic ligand capping the surface, we can assemble superlattices defined by alternating two distinct individual layers of materials in a periodic repeating pattern. By spin-coating the organic molecule capped In_2Se_3, a superlattice film is developed with controllable thickness based on how many layers are deposited (Fig. 14a). This is a rare example of a superlattice solution processed thin-film. By tuning the organic ligand used through ligand exchange, the properties of the superlattice can be tuned (Fig. 14b). From the X-ray diffraction pattern, the (001) peak can be shifted based on the organic molecule being used since the sizes of the organic molecules vary resulting in distinct d-spacing difference (Fig. 14c).

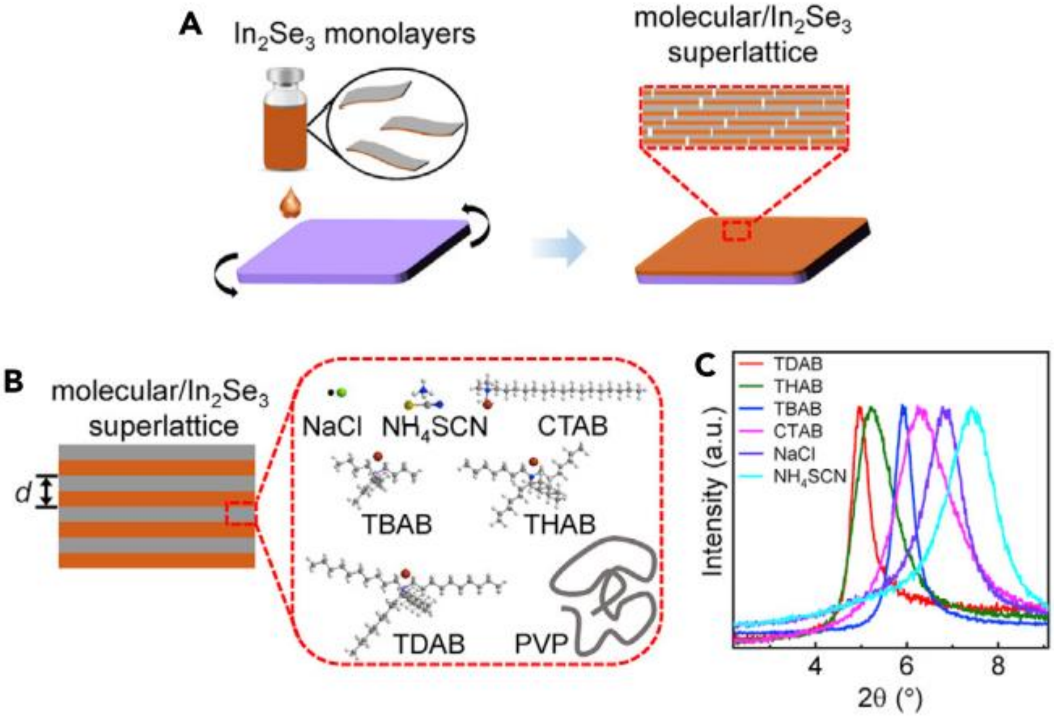

Figure 4.14. Schematic diagram and XRD data of superlattice formation. (a and b) Illustration of superlattice thin-film formation. (c) Different lattice spacing as a result of different organic molecule used for superlattice.

The assembly of the superlattice alongside with ability to change the ligand gives a more tunable material to suit a wider array of applications. One desired property that can be tuned is the electron transport within the superlattice material. To test electron transport differences between materials, gold electrodes were placed on top and bottom of the film to measure the tunneling threshold shown in (Fig. 15a) and (Fig. 15b). At a low applied voltage, the films are insulating due to the organic molecule but past a threshold we observe a sharp rise in current attributed to tunneling behavior. This threshold voltage can be tuned by changing the organic ligand. Large bulky organic ligands such as PVP resisted the tunneling effects to a much greater degree than shorter ones (Fig. 15c). This demonstrates the ability to make superlattice material with high degree of tunability all through pure solution-based approaches.

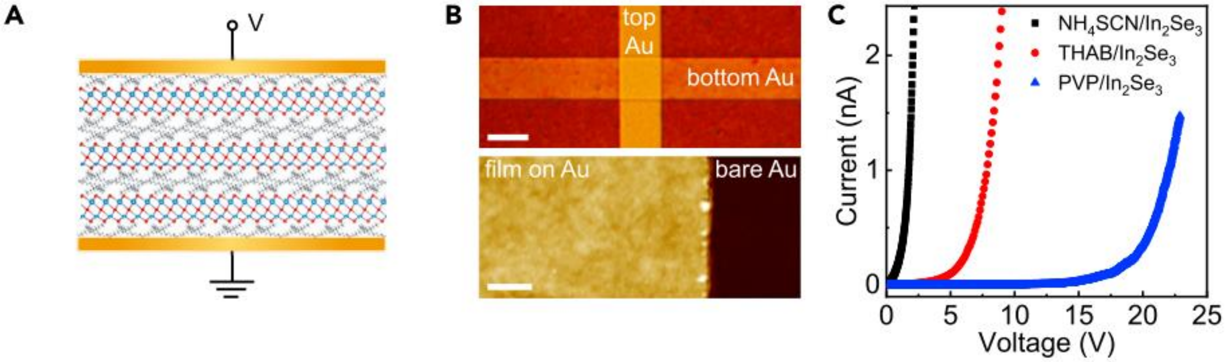

Figure 4.15. Electronic property characterization of superlattice. (a) Illustrated schematic of tunneling measurement device. (b) Top is optical microscope image showing how the gold electrodes were laid out. 20 µm scale bar. Bottom is atomic force microscope image showing uniform film on the gold. 2 µm scale bar. (c) Current versus voltage applied showing tunneling voltage changes with different organic molecule.

4.4 Conclusion

Here we show that not only can naturally occurring van der Waals layered crystals be used as electrodes for top-down ammonium molecule intercalation and exfoliation, but artificial layered crystals grown in lab could also be used. The lab grown crystals function similarly in the fact that intercalation can be achieved with bulky organic molecules and that this process makes large scale exfoliation down to nano size regime possible. This opens doors for this field as much more different materials can be explored to be used for nanosheet production through top-down methods. Many of the lab grown crystals have vastly different properties compared to naturally occurring ones such as MoS_2 and graphite. In_2Se_3 for example can be easily exfoliated down to monolayer in high concentration (95%). This is due to the lower inter-plane Youngs modulus which allows a self-refreshing intercalation to occur. The monolayer In_2Se_3 can be reassembled into superlattice heterostructure films with tunable properties through changing the organic ligands. Crystal growth alongside with electrochemical intercalation exfoliation allows new pristine quality nanosheets to be produced in solution-phase for a variety of applications.

4.5 Reference

1. Jung, Y.; Zhou, Y.; Cha, J. Intercalation in Two-Dimensional Transition Metal Chalcogenides. *Inorg. Chem. Front.* **2016**, 3, 452− 463.
2. Ambrosi, A.; Pumera, M. Exfoliation of layered materials using electrochemistry. *Chem. Soc. Rev*. **2018**, 47, 7213−7224
3. Luo, F.; Wang, D.; Zhang, J.; Li, X.; Liu, D.; Li, H.; Lu, M.; Xie, X.; Huang, L.; Huang, W. Ultrafast Cathodic Exfoliation of Few-Layer Black Phosphorus in Aqueous Solution. *ACS Applied Nano Materials.* **2019**, 2 (6), 3793−3801.
4. Zhong, Y. L.; Swager, T. M. Enhanced Electrochemical Expansion of Graphite for in Situ Electrochemical Functionalization. *J. Am. Chem. Soc.* **2012**, 134, 17896−17899.
5. Zhou, M.; Tang, J.; Cheng, Q.; Xu, G. J.; Cui, P.; Qin, L. C. Few-layer graphene obtained by electrochemical exfoliation of graphite cathode. *Chem. Phys. Lett.* **2013**, 572, 61−65.
6. Yu, P.; Lowe, S. E.; Simon, G. P.; Zhong, Y. L. Electrochemical Exfoliation of Graphite and Production of Functional Graphene. *Curr. Opin. Colloid Interface Sci.* **2015**, 20, 329−338.
7. Backes, C.; Abdelkader, A. M.; Alonso, C.; Andrieux-Ledier, A.; Arenal, R.; Azpeitia, J.; Balakrishnan, N.; Banszerus, L.; Barjon, J.; Bartali, R.; Bellani, S.; Berger, C.; Berger, R.; Ortega, M. M. B.; Bernard, C.; Beton, P. H.; Beyer, A.; Bianco, A.; Bøggild, P.; Bonaccorso, F.; Barin, G. B.; Botas, C.; Bueno, R. A.; Carriazo, D.; Castellanos-Gomez, A.; Christian, M.; Ciesielski, A.; Ciuk, T.; Cole, M. T.; Coleman, J.; Coletti, C.; Crema, L.; Cun, H.; Dasler, D.; De Fazio, D.; Díez, N.; Drieschner, S.; Duesberg, G. S.; Fasel, R.; Feng, X.; Fina, A.; Forti, S.; Galiotis, C.; Garberoglio, G.; García, J. M.; Garrido, J. A.; Gibertini, M.; Gölzhäuser, A.; Gómez, J.; Greber, T.; Hauke, F.; Hemmi, A.;

Hernandez-Rodriguez, I.; Hirsch, A.; Hodge, S. A.; Huttel, Y.; Jepsen, P. U.; Jimenez, I.; Kaiser, U.; Kaplas, T.; Kim, H.; Kis, A.; Papagelis, K.; Kostarelos, K.; Krajewska, A.; Lee, K.; Li, C.; Lipsanen, H.; Liscio, A.; Lohe, M. R.; Loiseau, A.; Lombardi, L.; Francisca López, M.; Martin, O.; Martín, C.; Martínez, L.; MartinGago, J. A.; Ignacio Martínez, J.; Marzari, N.; Mayoral, Á .; McManus, J.; Melucci, M.; Méndez, J.; Merino, C.; Merino, P.; Meyer, A. P.; Miniussi, E.; Miseikis, V.; Mishra, N.; Morandi, V.; Munuera, C.; Muñoz, R.; Nolan, H.; Ortolani, L.; Ott, A. K.; Palacio, I.; Palermo, V.; Parthenios, J.; Pasternak, I.; Patane, A.; Prato, M.; Prevost, H.; Prudkovskiy, V.; Pugno, N.; Rojo, T.; Rossi, A.; Ruffieux, P.; Samorì, P.; Schué, L.; Setijadi, E.; Seyller, T.; Speranza, G.; Stampfer, C.; Stenger, I.; Strupinski, W.; Svirko, Y.; Taioli, S.; Teo, K. B. K.; Testi, M.; Tomarchio, F.; Tortello, M.; Treossi, E.; Turchanin, A.; Vazquez, E.; Villaro, E.; Whelan, P. R.; Xia, Z.; Yakimova, R.; Yang, S.; Yazdi, G. R.; Yim, C.; Yoon, D.; Zhang, X.; Zhuang, X.; Colombo, L.; Ferrari, A. C.; Garcia-Hernandez, M. Production and Processing of Graphene and Related Materials. *2D Mater.* **2020**, 7, No. 022001.

8. Ayari, A.; Cobas, E.; Ogundadegbe, O.; Fuhrer, M. S. Realization and Electrical Characterization of Ultrathin Crystals of Layered Transition-Metal Dichalcogenides. *J. Appl. Phys.* **2007**, 101 (1), 014507.
9. Withers, F.; Bointon, T. H.; Hudson, D. C.; Craciun, M. F.; Russo, S. Electron Transport of WS2 Transistors in a Hexagonal Boron Nitride Dielectric *Environment. Sci. Rep.* **2014**, 4, 4967.

10. Castellanos-Gomez, A.; Wojtaszek, M.; Tombros, N.; Agraït, N.; van Wees, B. J.; Rubio-Bollinger, G. Atomically Thin Mica Flakes and Their Application as Ultrathin Insulating Substrates for Graphene. *Small.* **2011**, 7, 2491−2497.
11. Coleman, J. N.; Lotya, M.; O'Neill, A.; Bergin, S. D.; King, P. J.; Khan, U.; Young, K.; Gaucher, A.; De, S.; Smith, R. J.; Shvets, I. V.; Arora, S. K.; Stanton, G.; Kim, H.-Y.; Lee, K.; Kim, G. T.; Duesberg, G. S.; Hallam, T.; Boland, J. J.; Wang, J. J.; Donegan, J. F.; Grunlan, J. C.; Moriarty, G.; Shmeliov, A.; Nicholls, R. J.; Perkins, J. M.; Grieveson, E. M.; Theuwissen, K.; McComb, D. W.; Nellist, P. D.; Nicolosi, V. TwoDimensional Nanosheets Produced by Liquid Exfoliation of Layered Materials. *Science* **2011**, 331, 568−571.
12. Johnson-McDaniel, D.; Barrett, C. A.; Sharafi, A.; Salguero, T. T. Nanoscience of an ancient pigment. *J. Am. Chem. Soc.* **2013**, 135, 1677−1679.
13. Wu, Y. C.; Lan, A.; Yang, C. F.; Hsu, C. W.; Lu, C. M.; Yang, A.; Lan, C. W. Effect of Seed Arrangements on the Quality of n-Type Monolike Silicon Grown by Directional Solidification. *Cryst. Growth Des.* **2016**, 16, 6641−6647.
14. Venema, L. Silicon Electronics and Beyond. *Nature* **2011**, 479, 309.
15. Huang, Y.; Pan, Y. H.; Yang, R.; Bao, L. H.; Meng, L.; Luo, H. L.; Cai, Y. Q.; Liu, G. D.; Zhao, W. J.; Zhou, Z.; Wu, L. M.; Zhu, Z. L.; Huang, M.; Liu, L. W.; Liu, L.; Cheng, P.; Wu, K. H.; Tian, S. B.; Gu, C. Z.; Shi, Y. G.; Guo, Y. F.; Cheng, Z. G.; Hu, J. P.; Zhao, L.; Yang, G. H.; Sutter, E.; Sutter, P.; Wang, Y. L.; Ji, W.; Zhou, X. J.; Gao, H. J. Universal mechanical exfoliation of large-area 2D crystals. *Nat. Commun.* **2020**, 11 (1), 2453.

16. Xu, C.; Wang, L.; Liu, Z.; Chen, L.; Guo, J.; Kang, N.; Ma, X.- L.; Cheng, H.-M.; Ren, W. Large-Area High-Quality 2D Ultrathin Mo2C Superconducting Crystals. *Nat. Mater.* **2015**, 14, 1135−1141.
17. Jariwala, D.; Sangwan, V. K.; Lauhon, L. J.; Marks, T. J.; Hersam, M. C. Emerging Device Applications for Semiconducting Two-Dimensional Transition Metal Dichalcogenides. *ACS Nano* **2014**, 8, 1102−1120.
18. Wang, Y. X.; Zhao, M. T.; Ping, J. F.; Chen, B.; Cao, X. H.; Huang, Y.; Tan, C. L.; Ma, Q. L.; Wu, S. X.; Yu, Y. F.; et al. Bioinspired Design of Ultrathin 2D Bimetallic Metal-Organic-Framework Nanosheets Used as Biomimetic Enzymes. *Adv. Mater.* **2016**, 28, 4149− 4155.
19. Shi, Y.; Hamsen, C.; Jia, X.; Kim, K. K.; Reina, A.; Hofmann, M.; Hsu, A. L.; Zhang, K.; Li, H.; Juang, Z.-Y.; et al. Synthesis of FewLayer Hexagonal Boron Nitride Thin Film by Chemical Vapor Deposition. *Nano Lett.* **2010**, 10, 4134−4139.
20. Wang, Q. H.; Kalantar-Zadeh, K.; Kis, A.; Coleman, J. N.; Strano, M. S. Electronics and Optoelectronics of Two-Dimensional Transition Metal Dichalcogenides. *Nat. Nanotechnol.* **2012**, 11, 699− 712.
21. Fiori, G.; Bonaccorso, F.; Iannaccone, G.; Palacios, T.; Neumaier, D.; Seabaugh, A.; Banerjee, S. K.; Colombo, L. Electronics Based on Two-Dimensional Materials. *Nat. Nanotechnol.* **2014**, 7, 768−779.
22. Chhowalla, M.; Jena, D.; Zhang, H. 2D Semiconductors for Transistors. *Nat. Rev. Mater.* **2016**, 1, 16052.
23. Novoselov, K. S.; Falko, V. I.; Colombo, L.; Gellert, P. R.; Schwab, M. G.; Kim, K. A Roadmap for Graphene. *Nature* **2012**, 490, 192−200.

24. Song, F.; Hu, X. Ultrathin Cobalt-Manganese Layered Double Hydroxide Is an Efficient Oxygen Evolution Catalyst. *J. Am. Chem. Soc.* **2014**, 136, 16481−16484.

25. Deng, D.; Novoselov, K. S.; Fu, Q.; Zheng, N.; Tian, Z.; Bao, X. Catalysis with Two-Dimensional Materials and Their Heterostructures. *Nat. Nanotechnol.* **2016**, 11, 218−230.

26. Sun, Y.; Gao, S.; Lei, F.; Xie, Y. Atomically-Thin TwoDimensional Sheets for Understanding Active Sites in Catalysis. *Chem. Soc. Rev.* **2015**, 44, 623−636.

27. Qu, L.; Liu, Y.; Baek, J.-B.; Dai, L. Nitrogen-Doped Graphene as Efficient Metal-Free Electrocatalyst for Oxygen Reduction in Fuel Cells. *ACS Nano* **2010**, 4, 1321−1326.

28. Cao, X. H.; Tan, C. L.; Zhang, X.; Zhao, W.; Zhang, H. Solution-Processed Two-Dimensional Metal Dichalcogenide-Based Nanomaterials for Energy Storage and Conversion. *Adv. Mater.* **2016**, 28, 6167−6196.

29. Fowler, J. D.; Allen, M. J.; Tung, V. C.; Yang, Y.; Kaner, R. B.; Weiller, B. H. Practical Chemical Sensors from Chemically Derived Graphene. *ACS Nano* **2009**, 3, 301−306.

30. Yoo, E.; Kim, J.; Hosono, E.; Zhou, H.-s.; Kudo, T.; Honma, I. Large Reversible Li Storage of Graphene Nanosheet Families for Use in Rechargeable Lithium-Ion Batteries. *Nano Lett.* **2008**, 8, 2277− 2282.

31. Cao, X. H.; Tan, C. L.; Zhang, X.; Zhao, W.; Zhang, H. Solution-Processed Two-Dimensional Metal Dichalcogenide-Based Nanomaterials for Energy Storage and Conversion. *Adv. Mater.* **2016**, 28, 6167−6196.

32. Liu, Z.; Robinson, J. T.; Sun, X. M.; Dai, H. J. PEGylated Nanographene Oxide for Delivery of Water-Insoluble Cancer Drugs. *J. Am. Chem. Soc.* **2008**, 130, 10876−10877.

33. Bhatt, V. P.; Gireesan, K.; Pandya, G. R. Growth and Characterization of SnSe and SnSe2 Single-Crystals. *J. Cryst. Growth* **1989**, 96, 649−651.

34. Cevallos, F. A.; Guo, S.; Heo, H.; Scuri, G.; Zhou, Y.; Sung, J.; Taniguchi, T.; Watanabe, K.; Kim, P.; Park, H.; Cava, R. J. Liquid Salt Transport Growth of Single Crystals of the Layered Dichalcogenides MoS2 and WS2. *Cryst. Growth Des.* **2019**, 19, 5762−5767.

35. Yan, Z.; Jiang, C.; Pope, T. R.; Tsang, C. F.; Stickney, J. L.; Goli, P.; Renteria, J.; Salguero, T. T.; Balandin, A. A. *J. Appl. Phys.* **2013**, 114, 204301.

36. Ubaldini, A.; Jacimovic, J.; Ubrig, N.; Giannini, E. ChlorideDriven Chemical Vapor Transport Method for Crystal Growth of Transition Metal Dichalcogenides. *Cryst. Growth Des.* **2013**, 13, 4453−4459.

37. Shen, J.; He, Y.; Wu, J.; Gao, C.; Keyshar, K.; Zhang, X.; Yang, Y.; Ye, M.; Vajtai, R.; Lou, J.; et al. Liquid Phase Exfoliation of TwoDimensional Materials by Directly Probing and Matching Surface Tension Components. *Nano Lett.* **2015**, 15, 5449−54.

Chapter 5. Conclusion

Here we have explored the possibility of solution processability of two-dimensional inorganic nanostructures as active material in functional inks for printed electronics. This field was previously dominated by organic polymers which had poor performance and bad stability. Then further carried onto 0D and 1D nanostructured materials which suffered from poor film coverage or significant electron transport barriers. It has been shown here that 2D nanosheets offer great film coverage due to the large dimensional area, natural flexibility due to thin nature and their ability to lay flat on substrates creates interfacial contacts with no dangling bonds for superior charge transport. Overall, nanosheets is the better choice of material for large-area and flexible based solution-processed electronics. Once in colloidal form these 2D nanosheets can be easily printed over large-area substrates through already established printing methods.

These nanosheets have a variety of different approaches to be synthesized. Through bottom-up, the precursors along with heat and mixing can be used. Here InSe and SnSe were synthesized through air free methods. Bi_2Se_3 and Bi_2Te_3 2D structures were also created using a single pot polyglycol reduction method. It was also discussed the difficulty of bottom-up methods such as impurities from unreacted precursors and flower defects from aggregation. For superior pristine 2D nanocrystals able to function as active material for printed electronics, top-down methods were used.

Using MoS_2 as an example, it was shown an electrochemically driven cathodic intercalation was possible using aprotic polar solvents and ammonium organic molecules that are stable to applied voltages. The large size of the ammonium molecule means only simple bath sonication was needed to exfoliate the intercalated crystals down to nanosheets. The nanosheets made had little defects that are typically found in pure liquid phase exfoliation using an aggressive probe sonication or lithium intercalated MoS_2 which required a reaction with water to expand the lithium ions. Additionally, the low amount of electron injected into the MoS_2 crystal prevented any phase shift typically found in alkali metal intercalation. This retention of the crystalline quality led to the solution-based fabrication thin-film with high carrier mobilities of 10 $cm^2 \cdot V^{-1} \cdot s^{-1}$.

Using crystal growth techniques, a wide variety of different van der Waals layered crystals could be made. The lab grown crystals intercalated and exfoliated similarly to MoS_2 down to the dimension of 2D nanostructures. These could all be dispersed colloidally in various solutions to be used as functional inks. Many of these crystals had different electronic and physical properties to be exploited for various applications. Here we show that In_2Se_3, InSe, and Bi_2Se_3 could be exfoliated down to monolayers to be used to create superlattice thin-films with tunable electronic properties. This dissertation pushes the boundaries of colloidal 2D nanosheets used in printed electronics. Future research would involve the bottom-up synthesis or top-down exfoliation of p-type, conductive, and insulating material so high quality all printed electronics can be made. This is believed to be the future of large-area electronics.